SAPIENZA
UNIVERSITÀ DI ROMA

Terahertz and Optical Response of Novel Quantum Materials

Facoltà di Scienze Matematiche, Fisiche e Naturali
Corso di Dottorato in Scienze Fisiche "Vito Volterra" - XXXV Ciclo

Candidato

Tomarchio Luca
Matricola 1641766
Email: luca.tomarchio@uniroma1.it

Relatore

Prof. Stefano LUPI

Anno Accademico 2022/2023

Research is what I'm doing when I don't know what I'm doing

- Wernher von Braun

Abstract

Quantum materials are a class of systems that host low energy emergent properties due to the strong correlations between the lattice, charge, spin and orbital degrees of freedom. In recent years, this classification has encompassed the world of strongly correlated materials, like high-temperature superconductors and Mott-Hubbard insulators, and the topological states of matter, like Dirac/Weyl semimetals and topological insulators. This doctoral thesis discusses the study of the optical characterization of novel quantum materials, with a special focus on the terahertz (THz) spectral range, where low energy emergent features arise as a consequence of strong electronic correlations, symmetry breaking and/or topological transitions. The low energy photons associated to THz radiation grant an easy access to the quasiparticles occupying the low energy modes of quantum materials. The recent progress in the generation and detection of THz radiation have enabled the production of ultrashort pulses at the picosecond scale and their exploitation in time-domain spectroscopy measurements, like pump-probe and nonlinear spectroscopy, from which it is possible to study the out-of-equilibrium dynamics of electrons and dipole-coupled low energy states, along with the appearance of nonlinear responses at the presence of high external electric fields. This thesis shows that quantum materials can host a plethora of THz-related responses which can be tuned in terms of their thickness, temperature and external drivings, like the perturbation associated to an ultrashort optical pulse. It addresses the optical and THz study of novel magnetic quantum materials like Co_2MnGa, a magnetic nodel line semimetal, $MnBi_2Te_4$, the first intrinsic magnetic topological insulator discovered, and CrI_3, a layered ferromagnetic insulator with research interests ranging from spintronics to topological Majorana modes. In particular, the interplay between the magnetic, electronic and phononic states is addressed through linear and nonlinear spectroscopy, along with the direct sampling of the topological features by optical means. As a final purpose, this thesis also reports the novel findings for the direct optical sampling of the superconductive gap in the Sr-doped nickelate $NdNiO_2$, a strain-induced superconductor. The results show how the electrodynamic properties of this material are quantitatively different from the ones found in cuprate superconductors, sharing a similar infinite layer structural phase.

Contents

Acknowledgements

I would like to acknowledge all the people that supported me during my PhD program. In particular, a mention to my direct colleagues at the THz Sapienza lab Annalisa D'Arco, Salvatore Macis, Sen Mou and Lorenzo Mosesso, and to my supervisor Stefano Lupi. A further mention goes to the people that supported my studies with whom I closely collaborated in these last three years: Nicola Poccia, Mickey Martini, Mariangela Cestelli Guidi, Rebecca Cervasio, and Pascale Roy.

Publication List

This thesis is based in part on the following articles:

- Luca Tomarchio, Lorenzo Mosesso, Salvatore Macis, Antonio Grilli, Martina Romani, Mariangela Cestelli Guidi, Kejing Zhu, Xiao Feng, Michele Zacchigna, Massimo Petrarca, Ke He & Stefano Lupi, "Electrodynamics of $MnBi_2Te_4$ intrinsic magnetic topological insulators", *NPG Asia Materials* **14**, 82 (2022)

- Rebecca Cervasio, Luca Tomarchio, Marine Verseils, Jean-Blaise Brubach, Salvatore Macis, Shengwei Zeng, Ariando Ariando, Pascale Roy & Stefano Lupi, "Optical Properties of Superconducting $Nd_{0.8}Sr_{0.2}NiO_2$ Nickelate", arXiv:2203.16986 (2022)

- Luca Tomarchio, Salvatore Macis, Lorenzo Mosesso, Loi T. Nguyen, Antonio Grilli, Mariangela Cestelli Guidi, Robert J. Cava & Stefano Lupi, "Low energy electrodynamics of CrI_3 layered ferromagnet", *Scientific Reports* **11**, 23405 (2021)

- Luca Tomarchio, Salvatore Macis, Lorenzo Mosesso, Loi T. Nguyen, Antonio Grilli, Mariangela Cestelli Guidi, Robert J. Cava & Stefano Lupi, "Optical Phonon Anharmonicity and Spin-phonon Coupling in Bulk CrI_3", (to be published) (2022)

- Annalisa D'Arco, Luca Tomarchio, Valerio Dolci, Paola Di Pietro, Andrea Perucchi, Sen Mou, Massimo Petrarca & Stefano Lupi, "Broadband Anisotropic Optical Properties of the Terahertz Generator HMQ-TMS Organic Crystal", *Condensed Matter* **5** (3), 47 (2020)

- Luca Tomarchio, Sen Mou, Lorenzo Mosesso, Anastasios Markou, Edouard Lesne, Claudia Felser & Stefano Lupi, "Frequency- and Time-dependent Optical Conductivity of Co_2MnGa Nodal Semimetal", (to be published) (2022)

- Luca Tomarchio, Sen Mou, Lorenzo Mosesso, Anastasios Markou, Edouard Lesne, Claudia Felser & Stefano Lupi, "THz Generation from the Topological Nodal Line Semimetal Co_2MnGa", *ACS Applied Electronic Materials* (Under peer review) (2022)

List of additional papers published during the doctoral program:

- Akinori Irizawa, Masaki Fujimoto, Keigo Kawase, Ryukou Kato, Hidenori Fujiwara, Atsushi Higashiya, Salvatore Macis, Luca Tomarchio, Stefano Lupi, Augusto

Marcelli & Shigemasa Suga, "Spatially Resolved Spectral Imaging by A THz-FEL", *Condens. Matter* **5**(2), 38 (2020)

- Salvatore Macis, Luca Tomarchio, Silvia Tofani, S Javad Rezvani, Luigi Faillace, Stefano Lupi, Akinori Irizawa & Augusto Marcelli, "Angular Dependence of Copper Surface Damage Induced by an Intense Coherent THz Radiation Beam", *Condens. Matter* **5**(1), 16 (2020)

- Sen Mou, Annalisa D'Arco, Luca Tomarchio, Marta Di Fabrizio, Alessandro Curcio, Stefano Lupi & Massimo Petrarca, "Simultaneous elliptically and radially polarized THz from one-color laser-induced plasma filament", *New Journal of Physics* **23** (6), 063048 (2021)

- Luca Tomarchio, Salvatore Macis, Annalisa D'Arco, Sen Mou, Antonio Grilli, Martina Romani, Mariangela Cestelli Guidi, Kailong Hu, Suresh Kukunuri, Samuel Jeong, Augusto Marcelli, Yoshikazu Ito & Stefano Lupi, "Disordered photonics behavior from terahertz to ultraviolet of a three-dimensional graphene network", *NPG Asia Materials* **13**, 73 (2021)

- Salvatore Macis, Luca Tomarchio, Silvia Tofani, Federica Piccirilli, Michele Zacchigna, Vincenzo Aglieri, Andrea Toma, Gaurab Rimal, Seongshik Oh & Stefano Lupi, "Infrared plasmons in ultrahigh conductive $PdCoO_2$ metallic oxide", *Commun Phys* **5**, 145 (2022)

- Salvatore Macis, Maria Chiara Paolozzi, Annalisa D'Arco, Luca Tomarchio, Alessandra Di Gaspare & Stefano Lupi, "Terahertz Resonators based on $YBa_2Cu_3O_7$ High-Tc Superconductor", *Applied Sciences* **12**, 20 (2022)

Contribution to Conferences and Workshops

- THz Sapienza Workshop 2019: "Spectroscopy and Imaging with THz Radiation using Ultimate Radiation Sources" (10-11/12/2019), University of Rome La Sapienza, Rome, Italy.
  Invited speaker and session moderator. Oral contribution with title: *THz Nonlinear Responses of Weyl Semimetals.*

- SuperFOx2020 Conference on Superconductivity and Functional Oxides (10-12/02/2020), Santa Margherita Ligure, Italy.
  Oral contribution with title: *THz Nonlinear Response of the Weyl Semimetal* WTe_2.

- 11th NGSCES 2021 conference (07-10/06/2021), virtual meeting.
  Poster contribution with title: *THz and Optical Spectroscopy Study of Magnetic Topological Materials.*

- LEES 2021 conference (28/06-01/07/2021), virtual meeting.
  Poster contribution with title: *Optical Identification of the Superconductive Gap in* $Nd_{0.8}Sr_{0.2}NiO_2$ (Best poster prize winner).

- Bilateral 3D Graphene workshop (25/11/2021), University of Rome La Sapienza, Rome, Italy.
  Invited speaker. Oral contribution with title: *Direct Optical Sampling of the Dirac Surface States in* $MnBi_2Te_4$ *Thin Films.*

- Quantum Materials for Quantum Technologies workshop (14-15/02/2022), Laboratori Nazionali di Frascati (LNF), Frascati, Rome, Italy.
  Invited speaker. Oral contribution with title: *Electromagnetic Properties of Magnetic 3D Topological Insulators.*

- GEMCMP22 Conference (16-18/06/2022), Rome, Italy.
  Invited speaker. Oral contribution with title: *Low Energy Electrodynamics of* CrI_3 *Layered Ferromagnet.*

- Superstripes 2022 Conference (20-24/06/2022), Laboratori Nazionali di Frascati (LNF), Frascati, Italy.
  Invited speaker. Oral contribution with title: *Optical Identification of the Superconductive Gap in* $Nd_{0.8}Sr_{0.2}NiO_2$.

Introduction

In the condensed matter physics playground, the term *quantum materials* (QM) has found its place as a way to classify states of matter that cannot be described in terms of the low-lying level quantum mechanical theories, like the Fermi gas or the Landau liquid. On a microscopic level, these materials are intrinsically complex due to the strong correlations between the lattice, charge, spin and orbital degrees of freedom. The resulting phases of matter can thus be linked to the concept of emergence, describing the appearance of low energy features as a consequence of the strong correlations, instead of a direct reductionist interpretation in terms of the single parts composing the material. From a historical point of view, the quantum materials label has encompassed the formerly known strongly correlated materials, like the high-temperature superconductors or the more general Slater and Mott-Hubbard insulators. However, since the discovery of the quantum Hall effect (QHE) in the 1980s[1], the new class of topological materials, whose electronic properties are related to the topological features of the band structure, has also found its place in the QM classification. Topological insulators, Dirac/Weyl semimetals and low-dimensional materials like graphene all find their place in the QM class.

As highlighted by the Nobel laureate Philip W. Anderson in its seminal paper "More is Different"[2], the concept of symmetry breaking is the core behind the variety of phenomena that appear in the condensed matter physics research branch. Different degrees of complexity can thus be created, ranging from perfectly ordered systems to chaotic ones, where no discernible order parameter can be identified as a consequence of the high complexity degree. The taste for these latter emergent properties coincided with the discovery of the topological states of matter, starting from the most trivial quantum Hall effect based on the quantization of Landau levels. Around the same time, a more clear picture was developed by Thouless, Kohmoto, Nightingale and den Nijs (TKNN)[3], highlighting the relation of the electronic features to the nontrivial topological properties (Chern numbers or TKNN integers) of the Bloch states of an electron in a crystal. A few years later, Haldane gave an example of how the integer quantum Hall effect could arise in a simple model of a crystal with zero magnetic fields[4]. The work of Haldane and Thouless was recognized by the 2016 Nobel prize in physics since it turned out to be crucial for many of the more recent developments of this area. The newfound quantum Hall state is fundamentally different from Landau's spontaneous symmetry breaking phases, like crystallization, magnetism, or superconductivity. In

the case of topological phases, the transition does not break any symmetry and the phases are not associated with any local order parameter. In the past years, the most active research in the topological properties of condensed systems has revolved around topological insulators. However, intermediate phases between them and the normal insulators also show new topological features, characterized by the appearance of a semimetallic state, known as a Weyl/Dirac state[5,6]. The quasiparticles describing this emergent phase are known as Dirac or Weyl electrons since they can be described by the homonym relativistic quantum equations[7,8].

The whole topological nature of matter can be described in terms of the geometric properties of the single electron's wavefunction, from which concepts like the Berry phase or the Berry connection arise[9]. In other words, these properties arise from the way the wavefunctions get entangled inside the material. The simple thought about entanglement in a solid is mind-boggling since in a single chunk of metal we have $\sim 10^{23}$ electrons. Even by taking in mind only the electrons at the Fermi surface, the ones that support the transport properties, the number is still enormous. These processes transcribe into remarkably robust properties of the topological phases, like the protection against back-scattering of the topological insulator surface states, supported by the time-reversal symmetry conservation, or the protection of the Weyl band structures against the formation of an energy gap. The combination of these topological states with further electronic correlations permits the production of the most intriguing phases of matter yet to be fully characterized, like topological superconductors or spin liquid phases, predicted to host fractionalized excitations in terms of spinons and Majorana quasiparticles[10,11].

To achieve quantum control of this new physics by electrical and optical means, more studies are necessary, especially in the low frequency and nonlinear regime. Due to the low energy nature of emergent phenomena, the terahertz, or far-infrared, region of the electromagnetic spectrum (typically referred to as the frequencies between 100 GHz and 30 THz) is of critical importance in the spectroscopy of condensed matter systems. Many of the electronic properties of semiconductors and metals are greatly influenced by bound states whose energies are resonant with terahertz photons. For the case of quantum materials, this is true especially for the linear and nonlinear conductivity behavior of the emergent phases, which contains the information on the fundamental processes behind the quasiparticles transport. Despite its importance, terahertz spectroscopy developments have been hindered by the lack of suitable tools. However, recent technological innovations in photonics and nanotechnology are now enabling THz research to be applied in many more sectors, like communications and medical sciences[12]. Indeed, terahertz radiation can well penetrate many materials such as paper, plastics, textiles and foams. This has lead to imaging applications in areas like non-destructive industrial quality checks. However, in the context of condensed matter physics, the most useful application of THz is for spectroscopic applications. A milestone in this path has been the development of THz time-domain spectroscopy (THz-TDS)[13], supported by the fundamental research in the generation and detection of THz waves by nonlinear optical effects, such as the creation of ultrafast photocurrents in semiconductors

or the optical rectification in organic and inorganic nonlinear crystals[14]. Gas is also one of the most promising and convenient nonlinear mediums for the generation of broadband pulsed terahertz radiation, with the highest generation efficiency in the case of high intensity, dual-frequency femtosecond laser pulses, focused to create an air plasma filament from which a broadband THz signal is emitted[15].

Outline of Thesis

The goal of this thesis is to address the low energy electrodynamics of novel quantum materials through spectroscopic means. In particular, it revolves around the study of four compounds of major interest in the modern solid state research.

In Chapter §1 of this work, the physics behind the classification of quantum materials is highlighted, with a focus on topological materials and the theoretical concepts used to model them.

Chapter §2 is dedicated to the production of THz radiation short pulses and its time-domain detection, highlighting the most modern experimental techniques and their application for the characterization of quantum materials. The chapter also contains the description of the experimental optical setups used in this thesis.

Part I focuses on the optical characterization of three magnetic quantum materials: Co_2MnGa (§3), a nodal/Weyl topological semimetal, $MnBi_2Te_4$ (§4), a magnetic topological/axion insulator, and CrI_3 (§5) a Van der Waals layered ferromagnet which has been predicted to host spin liquid phase features due to its high correlations between the lattice, electronic and magnetic degrees of freedom. It highlights the linear light-matter interaction for the three materials by studying their transmittance and reflectance of light across a broadband spectrum, from THz to Visible. The former two topological systems are studied in a thin film geometry, while the latter in a single-crystal one. For Co_2MnGa, THz emission spectroscopy is used to characterize the hidden topological features, directly contributing to nonlinear processes like the production of photogalvanic effects. Optical pump-THz probe measurements for the same samples are also reported, highlighting the strong coupling of the charge carriers with the lattice through the formation of polaronic states.

Chapter §6 reports the novel findings for the direct optical sampling of the superconductive gap in the nickelate $Nd_{0.8}Sr_{0.2}NiO_2$ thin film, a strain-induced superconductor. Reflectance spectroscopy results are reported, highlighting the electrodynamic properties of this material and their comparison with cuprate superconductors, sharing a similar infinite layer structural phase.

Chapter 1

Quantum and Topological Materials: an overview

In condensed matter, the main goal is to understand all the possible beautiful emergent phenomena and states that can appear by putting electrons and atoms together. These building blocks in the quantum world can form different states of matter, and one of the greatest triumph of condensed matter physics in the last century is the classification of these states by the principle of spontaneous symmetry breaking, meaning that the ground state of the system doesn't respect its intrinsic symmetry. The pattern of symmetry breaking leads to an unique order parameter, which assumes a non-vanishing expectation value only in the ordered state, and a general effective field theory can be formulated based on it. This theory, known as Landau-Ginzburg theory, is determined by general properties such as dimensionality and symmetry of the order parameter, and gives an universal description of quantum states of matter. This chapter will present the novel phases of matter characterizing the materials whose experimental study is the main goal of this thesis. Topological semimetals and insulators will be introduced, along with the quantum spin liquid phase and the phenomenology of high temperature superconductors.

The concept of symmetry breaking is the tool nature needs to increase the complexity of a system. The lack of symmetries can be related to the appearance of new degrees of freedom, the order parameters, thus rendering the material a bit more difficult to describe in his new symmetry-broken phase. Moreover, Goldstone's theorem dictates the appearance of new collective excitations inside the material in the form of Nambu-Goldstone bosons. For instance, phonons appear due to the breaking of Galilean and continuous translational and rotational symmetry, while magnons due to the breaking of the original rotational symmetry in magnets. A solid will thus have a multitude of degrees of freedom, starting from the electronic charge and orbital ones, to which we add the spin and the lattice collective excitations. These attributes, when coupled together, determine the overall responses of the system to external stimuli, appearing in terms of materials' electrical, magnetic, optical, thermal, and mechanical properties. A response that arise from such a complex network of interactions and diversity of the degrees of freedom in fundamentally emergent, meaning that it cannot be described through a

reductionist approach but, instead, needs to take in mind the material as a whole. This new way to classify states of matter in terms of their emergent phases has been remarked multiple times in seminal papers from eminent physicists like P. W. Anderson [2] and R. B. Laughlin and D. Pines [16], with the latter suggesting a completely new point of view of the phenomena appearing in condensed matter physics, introducing the concept of *quantum protectorate*, meaning the idea that phases of matter can be described only by an organization that arises on a different scale with respect to the one of the single atomic components. Examples of quantum protectorate behavior can be steadily find in the superconducting phase, where electrons behave collectively sharing an equal macroscopic phase. The well known robustness to scattering of superconducting electrons emerges as a result of this collective behavior. Indeed, effective field theories like the BCS theory become the main theoretical tool to describe similar emergent phenomena, since they can be applied to the specific energetic scale at which the phenomena of interest take form. Emergent effects like superconductivity induce changes in the low energy structure of matter, close to the Fermi level, while becoming invisible at higher energies (an example is the breaking of superconducting pairs), the one needed to investigate the single components of the supporting system.

The active research behind the quantum materials category is supported by the need of controlling the emergent phenomena they host. These complex phases of matter are usually found in transition metals (TM) compounds. This is due to the complexity of the structures that can be composed using the d-orbitals filled with valence electrons. The theory that describes their hybridization is the *crystal field theory*, with whom it is possible to understand the splitting of the d-orbitals degeneracies into other electronic configurations, depending on the coordination complex geometry. The generalization of these orbitals to periodic lattices is obtained through the tight-binding theory. However, when dealing with complex phases, an orbital description is not enough. For instance, some materials that are predicted to be d-wave metallic by the tight-binding theory are instead insulators. These stunning events are known as metal-insulator transitions (MITs) and their origin is versatile, like simple band-gap closing, Anderson localization, electron-lattice interactions or electron-electron interactions [17]. The latter process is better known as the *Mott transition* [18]. At a finite temperature, preferably around and beyond room temperature for practical applications, the MIT can provide useful functions like gigantic, ultrafast switching of versatile physical properties. Electrical conductivity and other transport, magnetic and optical properties can all be affected by the MIT. Due to the importance of these applications, the terminology "Mottronics" was coined to represent the concept of electron technology exploiting the Mott transition. The most striking modern innovations regarding this field revolve around the use of vanadium dioxide as a medium for modern transistors, thermal protection or optical detectors. The study of the out-of-equilibrium properties of the MIT can also give striking results for a better understanding of the strong correlations characterizing these materials. For instance, high-temperature superconductors are Mott insulators in their room temperature phase, meaning that studying their "*Mottness*" [19] would permit to obtain insights about the mechanism behind the superconducting phase.

Originally introduced to emphasize the exotic properties of unconventional superconductors, heavy-fermion systems, and multifunctional oxides, the definition of quantum materials has morphed into a much broader container that also encompasses research on topological properties, two-dimensional (2D) materials and driven quantum systems, as shown in Fig. 1.1. These applications of these novel phases of matter range from spintronics, due to the non-trivial magneto-electron responses, to thermal and electro-optical devices[20,21]. These phenomena are easily highlighted in the topological materials family, where the presence of a strong spin-orbit coupling leads to a complex interplay between the orbital and spin degrees of freedom, coupling electric polarization and magnetism.

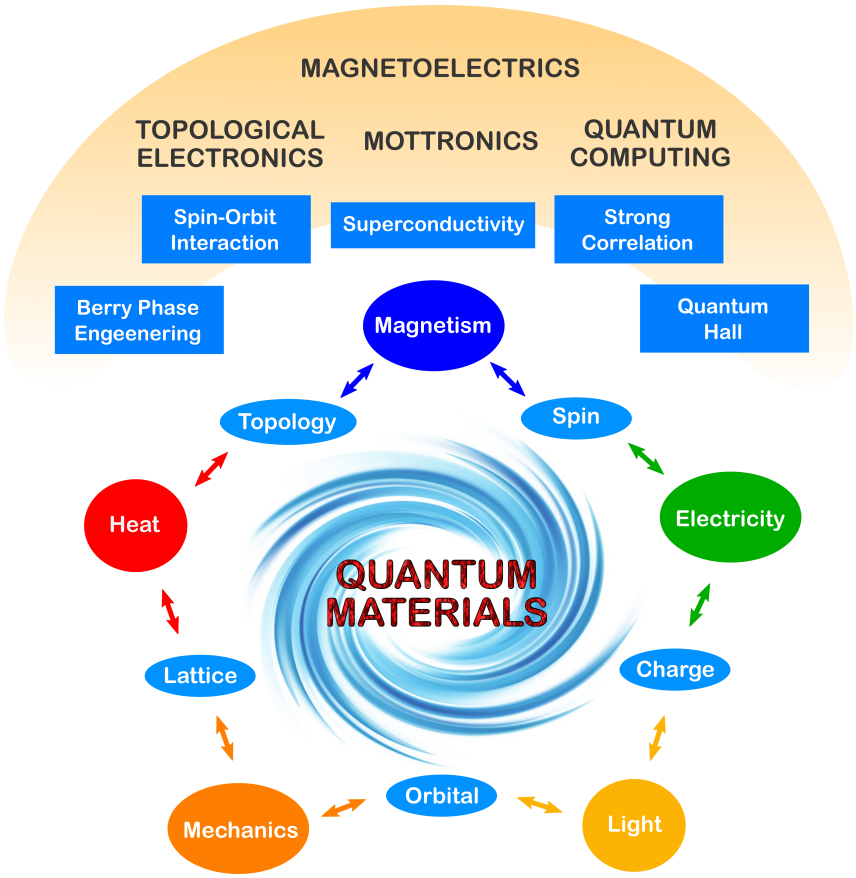

Figure 1.1: The picture shows various degrees of freedom of correlated electrons in solids that can respond to external stimuli. These effects lead to emergent functions depicted on top and to the development of related applications such as Mottronics, magnetoelectrics, topological electronics, and quantum computing.

1.1 Topological Materials

In 1980, a new quantum state was discovered, the quantum Hall (QH) state[1], which does not fit into the symmetry-breaking paradigm. In the QH state, a two-dimensional sample is subjected to an external magnetic field and low temperatures, hosting Landau levels as electronic quantum states and becoming insulating. However, an electric current can be carried along the 1D edges of the sample. The flow of this unidirectional current avoids dissipation and gives rise to a quantized Hall effect. Over the past 30 years, the study of the quantum Hall effect has led to a different classification paradigm, based on the notion of topological order. In mathematics, topological classification discards small details and focuses on the fundamental distinction of shapes, like the impossibility to smoothly transform a cup to a pretzel without applying a cut somewhere on the shape. In physics, precisely quantized physical quantities such as the Hall conductance also have a topological origin, meaning that they remain unchanged by smooth changes in the sample, making them robust against perturbations and disorder.

A topological phase is a phase of matter whose low-energy field theory is a topological field theory[22]. The term topological implies the existence of a bulk invariant that differentiates between phases of matter having the same symmetry. The energy spectrum alone, with or without boundaries (edge states), is insufficient to determine the full topological character of a state of matter. In the bulk of an insulator, it is a known fact that the topological structure is encoded in the eigenstates, rather than the energy spectrum. As such, we can expect that entanglement, which depends only on the eigenstates, can provide additional information about the topological nature of the system.

The Berry phase (or geometrical phase) concept is the principal missing tool in the original band theory description of solids, that permits to enhance it to a topological version. The Berry phase has its origins in the phase arbitrariness that we get while thinking about an orthonormal set of eigenstates for a Hamiltonian dependent upon a number of parameters variable with time, like fields or strains (see appendix A). As highlighted by the parallel-transport gauge (appendix A.1.2), one of the most important applications of the Berry phase is the characterization of degenerate energy states. If the denominator in Eq. A.3 is close to zero, this degeneracy will correspond to a monopole in the parameter space of the Berry curvature. To further analyze this point, we consider a general Hamiltonian H for a two-level system, parametrized by a parameter $\mathbf{R}$, and its two energy eigenvalues $E_\pm$

$$H = \epsilon(\mathbf{R})T_{2\times 2} + \mathbf{d}(\mathbf{R})\cdot\sigma \qquad E_\pm(\mathbf{R}) = \epsilon(\mathbf{R}) \pm \sqrt{\mathbf{d}\cdot\mathbf{d}} \tag{1.1}$$

where σ are the Pauli matrices and the offset term ϵ is negligible for the Berry phase computation. Substituting $\mathbf{d}$ as $|d|(\sin\theta\cos\phi, \sin\theta\sin\phi, \cos\theta)$ and taking $\mathbf{d}(\mathbf{R}) = \mathbf{R}$, we see that the Berry curvature takes the form of a monopole $\frac{1}{2}\mathbf{d}/d^3$ of strength $1/2$ for the - band, and $+1/2$ for the + band. If we integrate the Berry curvature over a sphere containing the monopole, we get 2π, and hence the Berry curvature integrated over a closed manifold is equal to 2π times the net number of monopoles (degeneracies)

contained inside. This integer is known as the Chern number. When different from zero, it is the source of the intrinsic anomalous Hall effect in solids. The Chern number concept made its first appearance in the electronic structure in 1982, in the famous TKNN paper about quantum Hall effect[3].

One of the most important consequences of these topological properties is the formation of edge modes strictly related to the bulk behavior of the band structure, namely the *bulk-edge correspondence*[23], which is the reason why there can be moving electrons contributing to the anomalous Hall effect in insulating systems. Qualitatively, since we know that the Chern number is an integer that characterizes the phase of the system, and since we know that it cannot be changed under smooth deformations of the band structure, the conclusion is that the boundary region that separates two different Hall conductive materials must host electronics features that imply a rough change in the electronic properties, like a electronic gap-closing-and-reopening point. This phenomenon can be seen in topological insulators with the production of conductive helical edge states, in Weyl fermions with the formation of Fermi arcs, or in superconducting wires with the emergent Majorana fermions. These topological systems are described in the next sections.

1.2 Topological Semimetals

In condensed matter physics, where one deals with energy scales much smaller than the rest mass of the electron, it would appear from a trivial observation that a non-relativistic description, with minor corrections, would be enough to fully describe the system, suggesting that Dirac physics would not play an important role. However, the propagation of even slow electrons through the periodic potential of a crystal leads to a dressing of the electronic states, from which a quasiparticle description emerges. In certain instances, this results in an effective low energy description in terms of the relativistic Dirac or Weyl equations.

The best known example of these phenomena is in graphene, where the energy dispersion of electrons near the edges of the Brillouin zone can be approximated for low energy excitations by the massless two dimensional Dirac equation. However, major interest has come nowadays from the three dimensional crystals which show linearly dispersing fermionic excitations. The line of reasoning behind this emergent phenomena resides in the study of the conditions under which degeneracies occur in electronic band structures, first investigated by Herring in 1937[24]. It was noted that, even in the absence of particular symmetries, one could obtain accidental two-fold degeneracies of bands in a three dimensional solid. These bands touching of Herring were named *Weyl nodes*, and the dispersion in the vicinity of these crossings is in general linear. These solid state realizations offer a platform where predictions made by relativistic theories can be tested, but at the same time entirely new properties that only exist in a condensed matter context emerge. This feature is highlighted by the fact that the strict symmetries of free space do not necessarily hold in a lattice, meaning that new fermion types with no counterpart in high-energy physics can emerge. Remarkably, several of the defining

physical properties of the high-energy fermions, such as the so called *chiral anomaly*, continue to hold in this nonrelativistic condensed matter context.

In 1928, Paul A. M. Dirac derived an equation for a relativistic quantum mechanical wave function, that describes an elementary spin-$\frac{1}{2}$ particle[25]:

$$H = c\mathbf{p} \cdot \alpha + mc^2\beta \tag{1.2}$$

where m is the mass of the fermion and c is the speed of light. The matrices α_i and β are known as the Dirac matrices, and satisfy the relations

$$\alpha_i^2 = \beta^2 = 1, \qquad \alpha_i\alpha_j = -\alpha_j\alpha_i, \qquad \alpha_i\beta = -\beta\alpha_i$$

The matrix form of the parameters has to be taken in mind due to the anticommutation relation. In one- and two-dimensional spatial space, they are at least 2×2 matrices. Thus, it appears that the Pauli matrices σ_i can be used to satisfy all these relations. In fact these can be written in the known forms

$$\sigma_x = \begin{pmatrix} 0 & 1 \\ 1 & 0 \end{pmatrix}, \qquad \sigma_y = \begin{pmatrix} 0 & -i \\ i & 0 \end{pmatrix}, \qquad \sigma_z = \begin{pmatrix} 1 & 0 \\ 0 & -1 \end{pmatrix} \tag{1.3}$$

satisfying the anticommutation relation $\{\sigma_i, \sigma_j\} = 2\delta_{ij}$. Thus, in one dimension, the two Dirac matrices α_x and β are any two of the three Pauli matrices, for instance $\alpha_x = \sigma_x$ and $\beta = \sigma_z$. In two dimensions all three of them are used. However, in three dimensions we can't find more than three 2×2 matrices satisfying the anti-commutation rules, therefore the four Dirac matrices are at least four-dimensional and can be expressed in terms of the Pauli matrices as

$$\alpha_i = \begin{pmatrix} 0 & \sigma_i \\ \sigma_i & 0 \end{pmatrix} \equiv \sigma_x \otimes \sigma_i, \qquad \beta = \begin{pmatrix} I & 0 \\ 0 & -I \end{pmatrix} \equiv \sigma_z \otimes I$$

where I is a 2×2 identity matrix. In three dimensions one has two solutions for positive energy and two further solutions for the negative one. The results obtained from the Dirac equation can be used to describe the motion of an electron with spin: the two solutions of the positive energy correspond to two states of the electron with spin-up and spin-down, while the remaining negative energy solutions correspond to a positron with spin-up and spin-down. Therefore, this equation demands the existence of antiparticles.

A number of variations of the Dirac equation quickly followed. In 1929, the mathematician Hermann Weyl proposed a simplified version that described massless fermions with a definite chirality (or handedness)[26]. To describe a massless particle in three dimensions we use for simplicity the γ-matrices formalism for the Dirac equation. For

this system it will take the form

$$\sum_{\mu=0}^{3} \gamma^\mu \partial_\mu \psi = 0, \qquad \text{or} \qquad i\hbar \frac{\partial \psi}{\partial t} = -ic \sum_{k=1}^{3} \gamma_0 \gamma_k \frac{\partial \psi}{\partial x^k}$$

where ψ is the wavefunction describing the massless particle, and the matrices follow the relations $\{\gamma^\mu, \gamma^\nu\} = 2\eta^{\mu\nu}$ with $\eta^{\mu\nu} = \text{diag}(-1, 1, 1, 1)$.

To represent the four γ matrices, we need 4×4 matrices. However, the matrix $\gamma_5 = i\gamma_0\gamma_1\gamma_2\gamma_3$ is Lorentz-invariant and obeys $\gamma_5^2 = 1$, thus its eigenvalues are ± 1. To simplify the problem, we can place on ψ a *chirality condition* $\gamma_5 \psi = \pm\psi$, reducing the problem to a 2×2 Dirac Hamiltonian. Once we reduce to a 2×2 matrix dimensionality, we can take the γ matrices to be the Pauli ones, i.e., $\sigma_i = \pm\gamma_0\gamma_i$, where the sign is dictated by the chirality condition. Given this result we can write[27]

$$\sigma_i \sigma_j = \delta_{ij} + i\epsilon_{ijk}\sigma_k$$

where ϵ_{ijk} is the Levi-Civita symbol, and the Dirac Hamiltonian now takes the form

$$H = \mp ic \sum_k \sigma^k \frac{\partial}{\partial x^k} = \pm c\vec{\sigma} \cdot \vec{p}$$

When we are in even dimensions, all this treatment fails since all the gamma matrices are utilized and their product is just the identity.

A charged relativistic fermion of defined chirality (eigenstate of γ_5) is called a *Weyl fermion*. The physical meaning of the eigenvalue of γ_5 is that it determines the fermion *chirality*, which is conserved during the motion. A chiral phenomenon is one that is not identical to its mirror image, and chirality coincides with the helicity concept in the limit of massless particles. However, for massive objects, the chirality concept becomes more abstract: it refers to how the particle's quantum mechanical wave function behaves when the particle is rotated (or looked at from a different angle). In our condensed matter context, it is simply used as a quantum number that permits an explicit differentiation of the two opposite chirality electron states. In particular, these newfound Weyl fields can be used as building blocks for the formation of the Dirac ones, meaning completely unconstrained solutions of the Dirac equation, given by the combination of right- and left-chiral Weyl fields. In fact, the main difference between the constrained and unconstrained solutions resides in the commutation with the parity operator, which involves the matrix γ_0 that anti-commutes with γ_5.

1.2.1 Weyl Fermions in Bulk Crystals

The discussion of Weyl materials starts by asking under what conditions would we expect to find a relativistic dispersion relation for electrons in a crystal. In general, quantum mechanical energy levels repel, which means that, if $H(\lambda)$ is a generic 1-parameter family

of Hamiltonians with no particular symmetry, generically its energy levels do not cross as a function of λ[27]. Thus, we might want to know how many parameters do we have to adjust to make two energy levels coincide in an "accidental" way (degeneracy not associated to any symmetry). The answer is at least 3.

We see this because a 2×2 Hermitian matrix depends on 4 real parameters, while a 2×2 Hermitian matrix whose energy levels are equal depends only on 1 real parameter

$$H = \begin{pmatrix} a & b \\ \bar{b} & c \end{pmatrix} \qquad \text{and} \qquad H = \begin{pmatrix} a & 0 \\ 0 & a \end{pmatrix}$$

To put this differently, any 2×2 Hermitian matrix can be written as $H = a + \mathbf{b} \cdot \sigma$, with σ the vector of Pauli matrices. The condition of equal eigenvalues is $\mathbf{b} = 0$, which are three real conditions. In three dimensions, a band Hamiltonian depends at least on three real parameters, so it is natural for two bands to cross at some isolated value $\mathbf{p} = \mathbf{p}_0$. Near this point, and looking only at the two bands in question, the Hamiltonian looks something like

$$H = a(\mathbf{p}) + \vec{b}(\mathbf{p}) \cdot \vec{\sigma} \tag{1.4}$$

where $\vec{b}(\mathbf{p}) = 0$ at $\mathbf{p} = \mathbf{p}_0$. Expanding near this point

$$b_i(\mathbf{p}) = \sum_j b_{ij}(\mathbf{p} - \mathbf{p}_0)_j + \mathcal{O}((\mathbf{p} - \mathbf{p}_0)^2), \qquad b_{ij} = \left.\frac{\partial b_i}{\partial p_j}\right|_{\mathbf{p}=\mathbf{p}_0}$$

Where we have neglected the constant zero order contribution. Thus, ignoring higher order terms, the band splitting is described near $\mathbf{p} = \mathbf{p}_0$ by

$$H' = \sum_{i,j} \sigma_i b_{ij}(\mathbf{p} - \mathbf{p}_0)_j$$

Apart from a shift $\mathbf{p} \to \mathbf{p} - \mathbf{p}_0$, this is essentially a Weyl Hamiltonian in 3+1 dimensions. The newfound Weyl fermion propagates with a speed way lower than c, and, in general, this propagation doesn't follow the standard Euclidean metric on $\mathbb{R}^3$. Instead, the natural metric governing these modes is[27]

$$||\mathbf{p}||^2 = \sum_i \left(\sum_j b_{ij} p_j \right)^2 \tag{1.5}$$

and the chirality of the gapless electron mode is given by $\chi = \text{sign}\, \det(b_{ij})$.

The appearance of Weyl nodes in the Brillouin zone must have a dual nature. This can be easily proved by the Berry phase formalism. When the Chern number is measured around Weyl nodes, taking the Berry curvature flux across the sphere S_α that contains

the bad point p_α, its sign quantifies the associated chirality. By using Stokes theorem on the entire reduced BZ and equation (A.2), one sees that

$$\sum_\alpha \frac{1}{2\pi} \int_{S_\alpha} \mathcal{F}_{ij} dS^{ij} = \sum_\alpha w(S_\alpha) = 0 \tag{1.6}$$

This result, valid for time-reversal symmetric systems, is generalized by the *Nielsen-Ninomiya theorem*. The theorem states that positive and negative chirality Weyl gapless modes must balance equally across the BZ, thus imposing the appearance of these nodes as doublets with opposite chiralities and same energies.

1.2.2 Robustness of the Weyl Phase

Due to the anti-symmetric statistical nature of fermions, the only electrons that support the transport properties in metals are the ones living at the Fermi surface. Therefore, to have a real Dirac/Weyl semimetal, we need the accidental band crossings to appear near the Fermi level. Similar degeneracies can be induced by the presence of strong spin-orbit coupling, similarly to topological insulators, arising in solids from the strong crystal electric fields produced by heavy ions. To achieve the condition of net-zero chirality across the BZ, as predicted by the Nielsen-Ninomiya theorem, a single four-degenerate node should appear (Dirac node). However, whenever parity and/or time-reversal symmetry are broken, this degeneracy splits into two two-degenerate nodes at the same energy level (Weyl nodes)[6].

From a simple analysis of the Weyl phase, one could speculate that this is a very unstable situation, and that any small perturbation, like disorder, would open a gap through band inversion, removing the Weyl node. However, in three spacial dimensions there exists a topological protection of the phase against small perturbations[28]. This protection is simple to understand. The condition for the points to annihilate in couples requires them to have well defined coordinates, hence the momentum has to be a good quantum number and traslational invariance has to be unbroken (weak disorder). Under this symmetry, two bands create a two-level system described by the 2×2 Pauli matrices. Because there are only three of them, they can acquire the three components of the lattice momentum as coefficients, such that any perturbation, that doesn't break any symmetry, has to couple with the Pauli matrices, and can only be reinterpreted as a shift in lattice momenta.

The topological way of understanding this robustness is through the Berry phase concept. Given the fermion doubling theorem (Nielsen-Ninomiya), this states that the Weyl nodes are opposite monopoles of the Berry connection with a same energy behavior. Therefore, it requires the Chern number of the band system to vanish, and the topological stability is related exactly to its conservation under smooth modifications of the Hamiltonian. In order to open a gap, the two Weyl nodes have to converge and form a Dirac one. The momentum separation of the two nodes is thus a measure of the Weyl phase stability.

1.3 Topological Insulators

Nontrivial electronic topology for the production of quantum Hall states can be generated by spin-orbit coupling (SOC) instead of a magnetic field. Because spin-orbit coupling respects time-reversal symmetry, unlike a magnetic field, there are some key differences. Indeed, SOC is the main ingredient in the research of topological materials, as shown in Fig. 1.2. In addition to the topological semimetals, topological insulators form a new class of topological states called the quantum spin Hall (QSH) states. Here SOC plays an essential role.

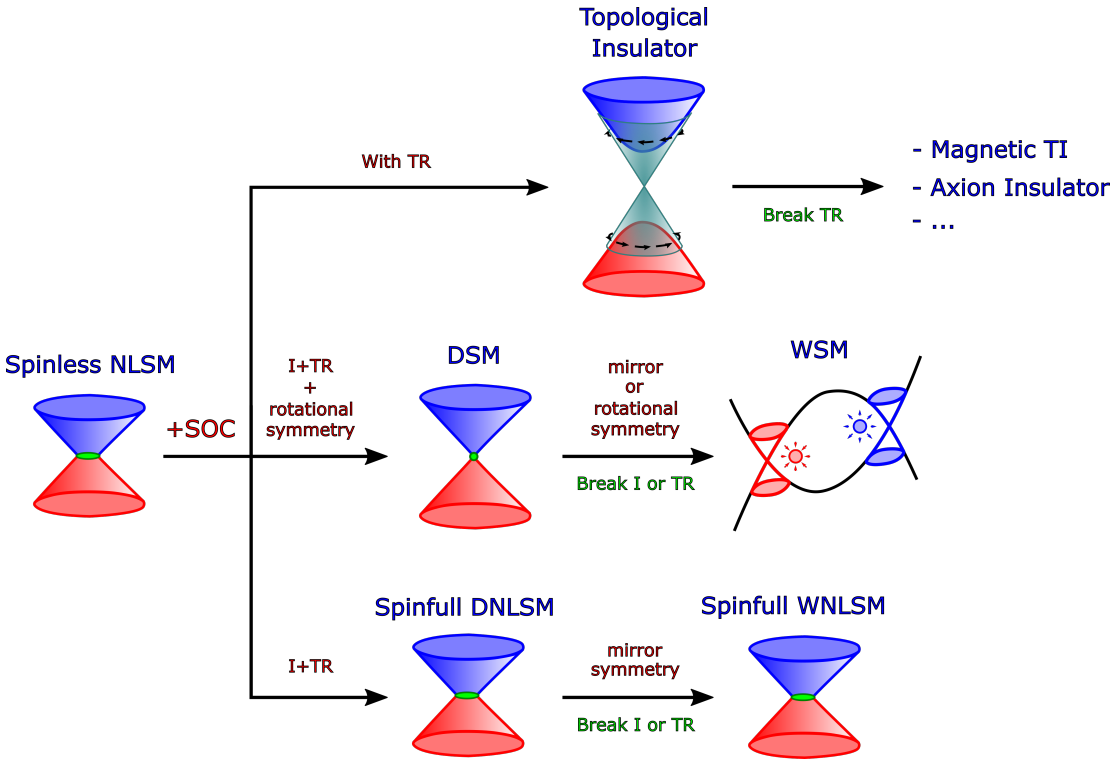

Figure 1.2: Schematic of different topological states and their relationship with each other (NDSM: nodal line semimetal, DSM: Dirac semimetal, WSM: Weyl semimetal, DNLSM: Dirac nodal line semimetal, WNLSM: Weyl nodal line semimetal, TI: topological insulator). SOC is the main element in the Hamiltonian for the production of the topological states. The symmetries indicate the global symmetry or spatial/lattice symmetry elements required to realize the new topological phase. I is the inversion symmetry, while TR the time reversal one.

The spin-orbit coupling is the origin of the fine structure of atoms. It comes from a relativistic quantum mechanical picture and can be simply expressed for a spin-full particle as $\sim \sigma \cdot (\mathbf{E} \times \mathbf{p})$, where σ is the spin, $\mathbf{E}$ the electrical field, and $\mathbf{p}$ the momentum.

The above expression can be written for a conservative potential in terms of the angular momentum $\mathbf{l}$ of the electron $\sim \sigma \cdot \mathbf{l}$. Such a coupling between the spin and orbital motion is a relativistic effect most pronounced in heavy elements. The manipulation of spin via SOC has not attracted much attention until J. E. Hirsh rediscovered the spin Hall effect in 1999[29].

In an ordinary Hall effect, like the quantum Hall (QHE) or anomalous Hall (AQHE) effect, the time-reversal symmetry is broken due to either an applied external magnetic field or a spontaneous magnetization. In contrast, the spin Hall effect does not require broken $\mathcal{T}$-symmetry (SOC doesn't affect it). Here, SOC will cause a drift of the electron motion like in the normal Hall state. However, it will depend on the spin state, increasing the spin-up and down densities at the edge of the material in order to balance the initial drift. The differences with respect to the QHE and AQHE are shown in Fig. 1.3.

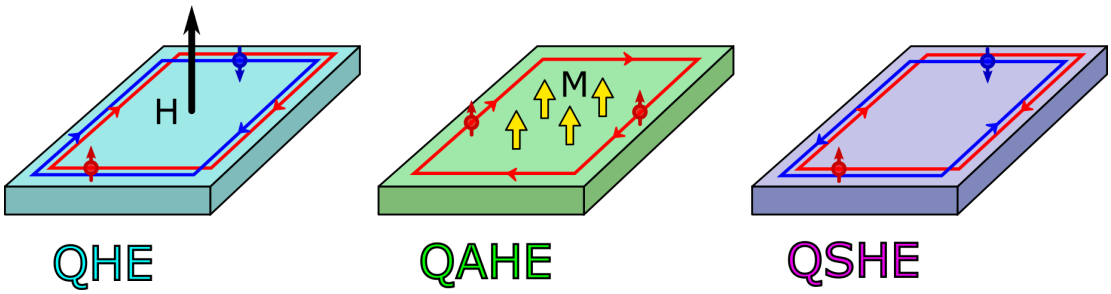

Figure 1.3: Comparison between the quantum Hall effect (QHE), the quantum anomalous Hall effect (QAHE), and the quantum spin Hall effect (QSHE). The QAHE can be induced by three processes: side-jump, skew-scattering, and/or an intrinsic Berry curvature.

To understand how the QSH effect might appear, we take graphene as a starting point and we introduce the spin variable in its low-energy Hamiltonian, that takes in mind both the Dirac points through a Pauli matrix τ_z [30]

$$H_0 = -i\hbar v_F \psi^\dagger (\sigma_x \tau_z + \sigma_y \partial_y)\psi = -i\hbar v_F \psi^\dagger \begin{bmatrix} \sigma_x \partial_x & 0 \\ 0 & -\sigma_x \partial_x + \sigma_y \partial_y \end{bmatrix} \psi \tag{1.7}$$

with ψ spinless field operators. Introducing spin, the Hamiltonian becomes an 8×8 matrix. We can now open a gap in different ways, for instance by introducing the effects given by SOC through the Hamiltonian

$$H_{SO} = \lambda_{SO} \psi^\dagger \sigma_z \tau_z s_z \psi + \lambda_R \psi^\dagger (\sigma_x \tau_z s_y - \sigma_y s_x)\psi \tag{1.8}$$

Here σ_i Pauli matrices act on the A(B) sublattice space of graphene, s_i on the spin space, and τ_i on the low energy $\mathbf{K}, \mathbf{K}'$ space. λ_{SO} is the so-called *Kane-Mele* (or intrinsic) SOC term[31] which originates from the next-nearest neighbor hopping, while λ_R is the *Rashba* SOC that originates from the mirror symmetry breaking in the z direction, perpendicular

to the graphene plane (for example by the presence of a substrate). This Hamiltonian does not violate $\mathcal{T}-$symmetry because time-reversal flips both the spin and σ_i. The Kane and Mele (KM) term opens a gap

$$E_k = \pm\sqrt{(\hbar v_F k)^2 + \lambda_{SO}^2}$$

The Rashba term itself, instead, is not able to open a full gap in the spectrum, due to the fact that this term does not anti-commute with the Hamiltonian. However, it is used to influence (reduce or enhance) the Kane and Mele gap, since the KM term anti-commutes with the Rashba term. The opening of a gap can be associated to the presence of two opposite Hall conductances in the non-trivial state[30,31]: +1 and -1, summing to zero as expected for a TR symmetric material, but forming gapless 1D edge states that conduct just like a QH state, connecting the bulk gapped ones (former Dirac cones). This results in a *quantized spin conductivity*, that is, the quantum spin Hall effect[31]. The 2D material is thus a topological insulator (TI), meaning that it is insulating in the bulk, but conductive at its edges. The edge states are "spin filtered", meaning that the electrons with opposite spin propagate in opposite directions (chiral and anti-chiral). Such states were later dubbed as *helical*. In principle, backscattering would open a gap in the edge states, meaning that transport would be blocked by Anderson localization. However, scattering is prohibited on the edge by TRS for an odd number of fermion pairs, due to Kramer's degeneracy theorem[32] that preserves the edge states from gapping. As long as time reversal is preserved, every k-point in the system must have a T-orthogonal counterpart at $-k$. Therefore, the T-invariant points must each host two states by Kramer's theorem. That means the gap can never open for a single pair of counter propagating modes (odd number of doublets). However, this protection fails at the presence of even doublets. This difference implies the existence of two separate classes, highlighting a Z_2 (cyclic group of order 2[1]) classification for the non-interacting topological insulators.

1.3.1 Inverted Quantum Wells

The Kane and Mele 2D proposal was hard to achieve experimentally. The gap opened by spin-orbit in graphene is extremely small. Instead, the topological insulating state has been achieved through a band inversion procedure in HgTe/CdTe quantum wells[33], hence, in the 2D interface between the HgTe and CdTe materials. In most common semiconductors, the conduction band is formed from electrons in s orbitals and the valence band is formed from electrons in p orbitals. In HgTe, however, the relativistic effect including spin-orbit coupling is so large that the bands are *inverted* (see Fig. 1.4), that is, the p-orbital dominated valence band is pushed above the s-orbital dominated conduction band. HgTe quantum wells are grown by sandwiching the material between CdTe, which has a similar lattice constant but much weaker spin-orbit coupling with normal band ordering. Therefore, increasing the thickness d of the HgTe layer increases

[1] It is the group isomorphic to the $\mathbb{Z}/2\mathbb{Z}$ group, the group of integers modulo 2.

the strength of the spin-orbit coupling for the entire quantum well, permitting its general tuning.

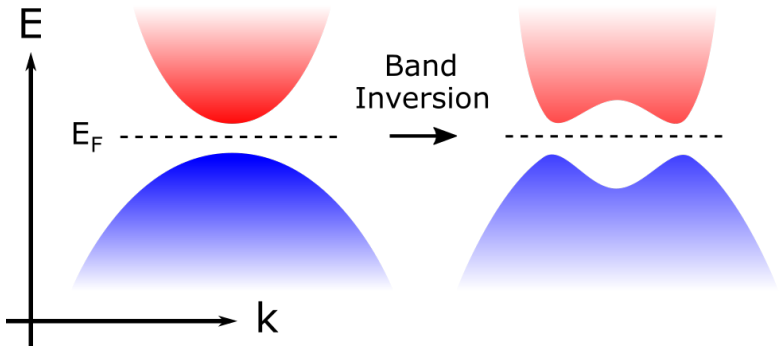

Figure 1.4: Schematic of a band inversion process, as caused by a strong spin-orbit coupling. The conduction band is pushed below the valence one through the Fermi level, creating a new insulating state (topological transition).

1.3.2 3D Topological Insulators

In 2007, 3D bulk solids of binary compounds involving bismuth were predicted to belong to the TIs family[34,35], generalizing the concept of 2D topological insulators as presented by the Kane and Mele SOC model. The first experimentally realized 3D TI state was discovered in bismuth antimode through ARPES[36]. Symmetry-protected surface states were also observed in other compounds, like bismuth selenide, bismuth telluride and antimony telluride[23]. Three dimensional TI have many things in common with graphene, such as their low-energy electronic response dominated by massless Dirac fermions excitations. Differences lie in the parity of the number of Dirac cones emerging at surfaces and the spin-orbit interaction, which results in the spin-momentum locking property already found in the Kane and Mele model. The Dirac cone Hamiltonian, $v_F \mathbf{p} \cdot \sigma$, is described in terms of pseudospin Pauli matrices for graphene, while spin matrices for TIs, with spin vector pointing always in the $\pi/2$ shifted direction, and the associated wavefunction carrying a π Berry phase (vorticity). The Hamiltonian of the edge states for 3D TIs that describes the pair of counter-propagating modes takes the form

$$H = \hbar v_F (\sigma \times \mathbf{k})_n \tag{1.9}$$

where the normal component to the surface is selected. This leads to a linear dispersion $E = \pm \hbar v_F k$. However, in real TIs the Fermi surface is not a perfect circle but has a warping[23]. In 3D topological insulators, the odd number of Dirac nodes on an edge appears to violate the Nielsen-Ninomyia theorem. The surface states are not spin degenerate and, since TRS requires the states at momenta $\mathbf{k}$ and $-\mathbf{k}$ to have opposite spin, the spin must rotate with $\mathbf{k}$ around the Fermi surface. The solution to this

controversy is given by the partner Dirac points residing on opposite surfaces. The main differences between the spin Hall edge states in 2D and the 3D TIs is that, in the latter, electrons don't propagate in a ballistic way, but diffuse on the surface.

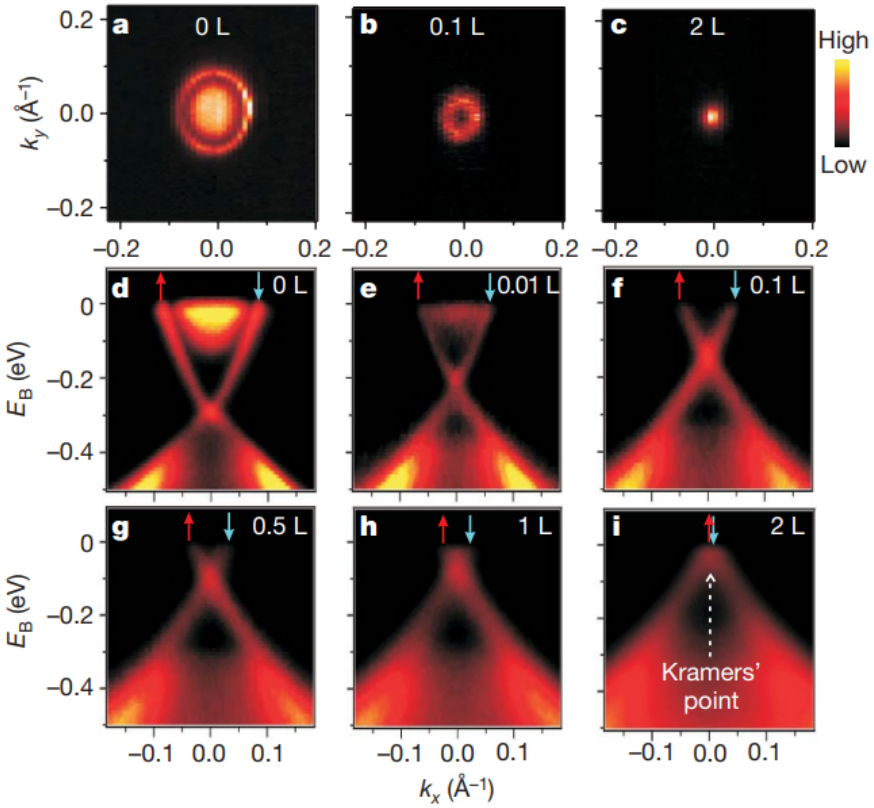

Figure 1.5: Example of Dirac-like dispersions measured through ARPES in Bi_2Se_3 by D. Hsieh et al[37]. Figures a) to c) show the topological Fermi surface at different values of surface disorder (L). Figures d) to i) show the evolution of the band dispersions. The figure is adapted from ref.[37].

1.3.3 Magnetic Topological Insulators

The previous section has introduced the helical surface states as the direct consequence of the bulk topological properties of 3D topological insulators. However, other emergent fingerprints can be found in the quantization of their electromagnetic response. Indeed, the electromagnetic fingerprint for 3DTIs turns out to be a topological magnetoelectric effect (TME)[38], that appears when TRS is broken at the surface but not in the bulk. These properties make 3DTIs an important building block for heterostructures, where proximity effects can be engineered.

The breaking of time-reversal symmetry is an important process in 3DTIs. The helical surface states are protected from gapping by the Kramer's degeneracy, which is removed when TRS is broken. Without this constraint, additional terms can be added to the surface states Hamiltonian that induce the creation of a gap at the Dirac node. The relativistic electrons thus acquire an effective mass due to the loss of their protection against backscattering. The new perturbed Hamiltonian can be written as[39]

$$H = v_F \left(-k_y \sigma_x + k_x \sigma_y\right) + m\sigma_z \tag{1.10}$$

where $2|m|$ is the energy gap at the Dirac node. The sign of m is also representative of the Chern number acquired by the 2D surface states, implying that a quantized anomalous Hall effect can now appear at the edge of each surface, giving rise to chiral edge modes. The Hall conductivity is quantized to $\sigma_H = sgn(m)e^2/2h$[38] whenever the Fermi level lies in the energy gap, according to the TKNN formula (integration of the Berry curvature over the occupied states in the Brillouin zone). The magnitude of the Hall conductivity is thus halved with respect to the normal QAHE. This difference is actually a fingerprint that we are observing a different topological state than the normal QAHE, which is linked to the topological magnetoelectric response of the bulk, i.e., the ability to induce a magnetization through an electric field or, alternatively, an electrical polarization through a magnetic field. This magnetoelectric effect can be taken in mind by adding to the Lagrangian of the system the so-called *axion term*[40]

$$L_{TI} = \frac{\theta e^2}{2\pi h} \mathbf{E} \cdot \mathbf{B} \tag{1.11}$$

where θ is a function of the Berry connection. For time-reversal symmetric TIs, it takes the fixed value $\theta = \pi$. However, when TRS is broken, it is allowed to change and produce exotic magnetoelectric effects[41]. These effects are known as axion electrodynamics. However, in the case of a QAH insulator, θ has opposite signs on the top and bottom surfaces. Hence, macroscopically, the topological magnetoelectric effect is cancelled out. To produce a TME or an axion insulator, it is necessary to realize an antiparallel magnetization or an opposite sign of the exchange gaps (m) on the top and bottom surface[41].

Experimentally, the realization of magnetic 3D topological insulators has been initially tackled through the introduction of magnetic impurities[42]. However, doping inhomogeneity leads to complex magnetic ordering and small exchange gaps[43]. As a consequence, the various topological quantum effects appear at very low temperatures. Therefore, intrinsic magnetic topological insulators are highly desired for increasing those temperatures and for investigating topological quantum phenomena.

1.4 Quantum Spin Liquids

In the search for novel quantum phases of solid matter, Quantum Spin Liquids (QSL) are one of the most complex and evasive. QSL can be considered "quantum disordered"

ground states of spin systems, in which zero-point fluctuations are so strong that a conventional magnetic long-range order cannot be reached. In this context, the simple semiclassical spin approach must be replaced by a quantum one, with the main consequences in the need to consider quantum fluctuations and the Berry's phase theory[44], which dictates the quantization of the spins. However, the essential ingredient of a QSL is not the lack of order, but the presence of an anomalously high degree of entanglement in a magnetic context, or *massive quantum superposition*[45]. We thus look for ground states that cannot be continuously deformed into a product state while staying within the phase, meaning that there is no way to disentangle the states without a sharp change of the microscopic properties of the material. As highlighted in the previous sections, topological phases are an example for these ground states.

The ingredient for such a recipe is strong SOC and/or hopping integrals. However, a metallic nature due to strong hopping integrals would rapidly hide the low energy quantum disordered state, as it usually happens in topological materials like Weyl semimetals and topological insulators. This, together with the lack of local order makes QSL states difficult to detect experimentally. Other experimental difficulties in finding and characterizing QSL states are given by the scarcity of massive entangled states in materials and the subtleties of their theoretical description, which leave only few smoking gun experimental signatures. It is currently very difficult to probe nonlocal features or measure the degree of entanglement, since traditional experiments usually detect order and local excitations. Therefore, we can only address the QSL states in an indirect way, thus relying on the theoretical models that predict how local excitations should behave in these materials.

From the materials prediction point of view, it is straightforward to seek QSL states in systems which host processes that destabilize the magnetic ordered states. Clearly, frustration must thus be an essential feature. The simplest platform for the appearance of frustration is given by a classical Ising model on a triangular lattice with antiferromagnetically (AFM) coupled nearest neighbor spins, as depicted in Fig. 1.6a. Because of the AFM coupling, two nearest neighboring spins A and B tend to be antiparallel. Then, a third spin C that is a neighbor of both A and B is frustrated because its two possible orientations, up and down, both have the same energy. The classical ground state of a multitude of such spins will thus have a high level of degeneracy. Therefore, materials that host honeycomb or Kagomé crystal structures (Fig. 1.6b-c) are valuable spin liquid candidates. In particular, magnetic insulators with layered honeycomb lattices can be described by the *Kitaev honeycomb model*[46], for which exact solutions for the ground state can be found (in the basis of Majorana quasiparticles). For frustrated QSLs with short-range spin correlation, it was proposed[47,48] that two unpaired spins may interact only weakly with each other and can be regarded as independent spin-1/2 elementary excitations called *spinons*. The process through which a spin-1 magnon turns into two independent spin-1/2 spinons is an example of *fractionalization*. Whether fractionalization of spin excitations actually occur in a particular spin system is a highly nontrivial question. Different experimental techniques can highlight similar features indirectly. Indeed, this thesis focuses on light spectroscopy and a few insights

are needed when dealing with QSLs using this technique. For instance, the polarization operator sensible to the incident light does not involve the magnetic degrees of freedom. However, spin-lattice interactions and spin–orbit coupling may lead to a coupling with the spins. This means that magnetic excitations quite generically lead to non-zero absorption within the electronic gap of QSL candidates. As we will highlight in section 5, the main difficulties in detecting these features lie in the separation of the spin contributions to the stronger low energy collective excitations like phonons. Due to these complexities, applications to QSLs are limited and open to multiple interpretations.

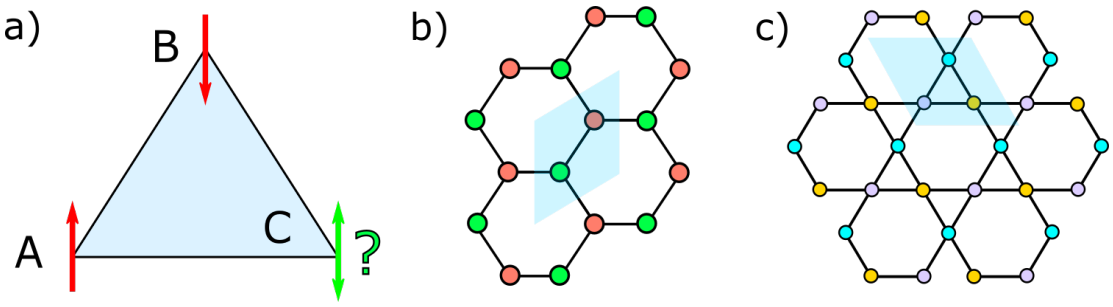

Figure 1.6: **a)** Antiferromagnetic coupling between spins in a triangular lattice. The spin C can either point upward or downward since the two configurations are degenerate. **b)** Honeycomb 2D lattice with unit cell. **c)** Kagomé 2D lattice with unit cell.

Chapter 2

Terahertz Spectroscopy Methods

Terahertz radiation, also known as terahertz waves or THz, consists of electromagnetic waves within the frequencies of 0.1 to 30 terahertz (1 THz = 10^{12} Hz = 1000 GHz), or within [0.41; 124] meV, [3.34; 1000] cm^{-1}, and [2997; 9.99] μm. Terahertz radiation occupies a middle gap between microwaves and infrared light waves known as the terahertz gap[49–51]. In this region the frequency becomes too high to be measured digitally via electronic counters, thus it must be measured by probes using properties of wavelength and energy. Similarly, the generation and modulation of coherent electromagnetic signals in this frequency range ceases to be possible by the conventional electronic devices. Just like infrared radiation, the frequency of THz is low enough to propagate in a line of sight (no diffusion) and is non-ionizing. Like microwave radiation, instead, it can penetrate a wide variety of non-conducting materials. Due to these properties, THz has been proposed as a probe in different applications, ranging from medical imaging devices to military implementations.

In the context of quantum materials, THz radiation can directly probe the low energy excitations that arise from the complex phases of matter near the Fermi level. Spectroscopic probes like THz provide an experimental foundation for tests of theoretical models. Quantum materials are the platform where correlated effects among electrons and other quasiparticles take place. The complexity of the problem of correlated electrons poses difficulties for the theoretical analysis of many of their properties. Experimental probes can thus be used as icebreakers to prove the validity of theoretical models and simulations. When dealing with the spectroscopy of quantum materials, it is always useful to start the discussion with a reference to the Fermi liquid (FL), where interactions are reduced to small corrections of the free electron gas susceptibilities. For this system, the complex optical conductivity of electrons, $\sigma(\omega) = \sigma_1(\omega) + i\sigma_2(\omega)$, can be adequately described by the Drude model[52]

$$\sigma_D(\omega) = \frac{ne^2\tau}{m_b}\frac{1}{1 - i\omega\tau} = \frac{\sigma_{DC}}{1 - i\omega\tau} \tag{2.1}$$

where e is the electronic charge, n is the relevant density, m_b is the band mass of the carriers which is generally different from the free electron mass m_e, τ is the scattering

rate, and σ_{DC} is the dc conductivity. In dirty metals, impurities dominate and the scattering rate is nearly independent of frequency (with the exception of the e-ph scattering process), thus obscuring the quadratic form of $1/\tau(\omega)$ that is expected for electron-electron scattering of a Fermi liquid. This form of the conductivity accounts for the presence of *intraband* transitions, meaning the diagonal electronic transitions appearing in the conductive bands crossing the Fermi level. To describe the finite energy excitations coming from interband transitions, Eq. 2.1 is modified to provide the Drude-Lorentz expression of the optical conductivity[53]

$$\sigma(\omega) = \sigma_D(\omega) + \frac{\omega}{4\pi} \sum_j \frac{\omega_{pj}^2}{\omega\gamma_j - i(\omega^2 - \omega_{0j}^2)} \tag{2.2}$$

where the sum index j follows the number of optical transitions at specific frequencies ω_{0j} and intensities ω_{pj}, with a decaying factor γ_i. Eq. 2.2 can be used to describe the optical response of most materials. However, many quantum materials host responses that cannot be accounted by the Drude-Lorentz model, requiring instead specific corrections, mainly at low frequencies where emergent phenomena take place[54].

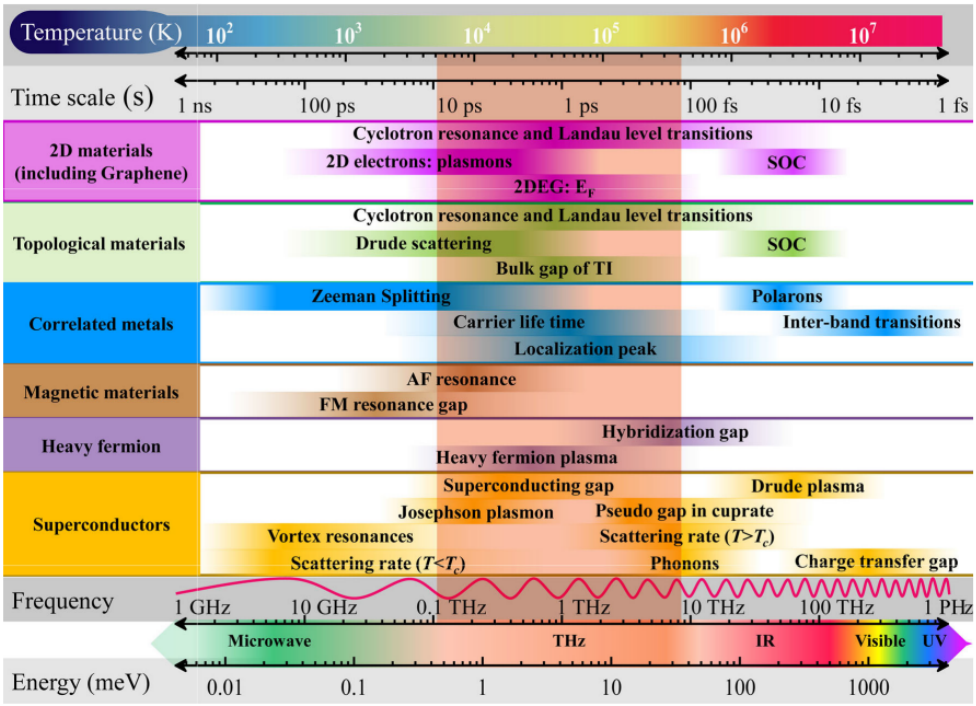

Figure 2.1: Schematic representation of the typical energy scales of various quantum materials. The orange band highlights the THz spectral range. The figure is adapted from ref.[54].

2.1 Experimental Probes and Techniques

Terahertz spectroscopy can be developed both in the time and frequency domain. However, the former is sensitive to the amplitude and the phase of the radiation (electric field), while the latter only on the amplitude (intensity). Indeed, a time domain probing system is linked to major difficulties in the production of short pulses and detection, but it may grant useful insights in the light-matter interaction and its evolution over time, like the out-of-equilibrium quasiparticle transport and their correlations.

Spectroscopic measurements in the frequency domain can be used to evaluate the optical constants of materials that are found in the context of Maxwell's equations for the description of light-matter interaction. The optical conductivity is the linear response function relating the current density j to the applied electric field E: $j(\omega) = \sigma(\omega)E(\omega)$. Another commonly employed notation is that of the complex dielectric function $\tilde{\epsilon}(\omega) = \epsilon_1(\omega) + i\epsilon_2(\omega)$. The real and imaginary parts of these two sets of optical constants are related by $\sigma_1(\omega) = (\omega/4\pi)\epsilon_2(\omega)$ and $\sigma_2(\omega) = -(\omega/4\pi)[\epsilon_1(\omega)-1]$. In anisotropic materials the complex optical constants acquire a tensor form. For instance, time reversal symmetry breaking by an applied magnetic field introduces nondiagonal components to these tensors known as Hall conductivity. In the Maxwell´s equations study of the optical constants we also need to consider the magnetic permeability μ of a material. This value is usually set to 1, with the exception of magnetic resonances usually occurring in microwave and very far-infrared frequencies (sub-THz). The complex optical constants as a function of frequency can be inferred from several complementary procedures, like the combination of reflectance $R(\omega)$ and transmission $T(\omega)$ spectra, meaning the light intensity percentage reflected and transmitted by a sample. The analytic expressions for the extrapolation of the optical indices are based on approximations, like the absence of Fabry-Perot terms interference or the condition of low absorption, from which it is possible to analytically couple the reflectance and transmittance measurements to the microscopic optical parameters[55]. Other methods use the Kramers-Kronig constrained analysis, especially when only one of the two macroscopic responses can be obtained. The Kramers-Kronig equations link the real and imaginary part of the conductivity[56]

$$\sigma_1(\omega) = \frac{2}{\pi}\int_0^\infty d\omega' \frac{\omega'\sigma_2(\omega')}{\omega'^2 - \omega^2} \tag{2.3}$$

$$\sigma_2(\omega) = -\frac{2\omega}{\pi}\int_0^\infty d\omega' \frac{\sigma_1(\omega')}{\omega'^2 - \omega^2} \tag{2.4}$$

such that it is possible to evaluate the complete response in terms of a single variable, the real or the imaginary part. The approximations used for this technique are based on the limitations of the measured spectrum, introducing a frequency cutoff in the integrals of Eq. 2.3 and 2.4. The Kramers-Kronig constraint can also be used in numerical evaluations of the optical parameters, for instance in the direct fitting process

of reflectance and/or transmittance through a specific microscopic model, like the Drude-Lorentz one. However, it is important to take in mind that the microscopic models for the conductivity do not always satisfy Eq. 2.3 and 2.4.

The reflected and transmitted light from a sample can be measured as a function of frequency through frequency-selective instruments like Michelson interferometers or monochromators. Other approaches, like ellipsometry, will not be accounted in this thesis. A Michelson interferometer uses the selective property of the light constructive and destructive interference to create an intensity signal (interferogram) containing the whole information on the frequencies under study, i.e., the spectral amplitude of the light source. This information is obtained by Fourier transforming the interferogram, which is expressed as a function of the time delay between the two optical paths of the interferometer arms. This signal is reflected or transmitted by the sample, and the respective spectral amplitude after the process is compared to the incident one coming from the light source. The ratio gives exactly the reflectance and transmittance values as a function of the frequencies contained in the spectral amplitude. This process is known as Fourier-Transform Infrared Spectroscopy (FTIR). The light source in FTIR experiments is usually a grey body like a lamp, emitting a wide range of frequencies.

Other instruments can also be used to generate electromagnetic radiation at specific frequencies. For instance, at higher wavelengths it is useful to use diffraction as the main principle for wavelength separation. This is done in monochromator devices by using an optical grating and a series of mirrors to transport the light to the sample position. At lower frequencies, in the THz range, novel setups like the quantum cascade lasers[57] offer great opportunities for the production of almost monochromatic light.

2.1.1 Thin films over Substrates

The metallic compounds studied in this thesis are measured in a thin film geometry. The materials thickness is controlled to values below 100 nm during the growth procedure, granting a high degree of the material quality (low impurities and defects). The thin film is not free-standing, but rather deposited on a specific substrate (hundreds of microns thick). The use of thin films is crucial for optical measurements due to a series of reasons:

- High crystal quality, reducing the impurity-related effects that might damage the emergent properties of quantum phases;
- Large flat material surface, useful to increase the number of photons sent on the sample and improve the signal to noise ratio of the optical measurements;
- Systematic study as a function of thickness, from which it is possible to tune the intrinsic properties of some materials;
- Higher transparency at low frequencies, given that the thickness is usually lower or comparable to the optical penetration depth.

Drawbacks of the thin film configuration are instead associated to the substrate contributions to the optical transmittance and reflectance. For instance, materials like silicon

are transparent up to 9000 cm^{-1}, or insulators like MgO have a strong MIR absorption given by the optical phonons. Due to this limitations, both transmittance and reflectance measurements are needed at frequencies where the film-over-substrate stack is opaque. Moreover, specific algorithms that take in mind the substrate contribution must be used when fitting the film response to a specific model. These models are described in appendix B.

2.1.2 THz Time-Domain Spectroscopy

Terahertz time-domain spectroscopy (THz-TDS or TDTS) is a spectroscopic technique in which the properties of matter are probed with short pulses of terahertz radiation, allowing phase-sensitive generation and detection of THz signals[58,59]. The working principle of TDTS is shown in Fig. 2.2. It starts with a femtosecond laser producing an optical-pulse train. Each pulse separates into two paths. One reaches the THz emitter, such as a photoconductive antenna, semiconductor wafer or nonlinear crystal, where the optical pulses are transformed into ultrashort THz ones (picosecond scale). Then, these propagate in free space or across a sample (transmitted or reflected) and are focused onto an ultrafast detector, such as a low-temperature-grown GaAs photoconductive switch or an electro–optic crystal. The other part of the pulse is also delivered onto the detector after passing through a time-delay stage. The rapid, optically induced changes in the detecting material properties on a femtosecond time scale is the origin of generation and detection of the ultrafast THz pulses. The probe pulse (femtosecond duration) is used to scan the longer THz one (picosecond) by sampling its electric field step-by-step of the delay line, thus changing the temporal overlap between the two signals in order to sample the entire THz waveform. The detailed way on how the two pulses can interact in a detection material will be explained later.

As already pointed out, time domain measurements give the possibility to measure directly the complete intensity and phase information of the electric field. Its shape in time is very sensible to phase shifts; small-frequency, independent-phase changes result in significant reshaping. In a general spectroscopy experiment, the beam passes through a specimen or is reflected by it such that the change in waveform of the THz signal is measured. The power of TDS resides in the possibility to measure the whole complex refractive index and, hence, all the microscopic responses without the use of Kramers-Kronig relations, generally exploited as a bridge between the real and the complex part of the optical indices. The whole dataset for the THz-TDS spectroscopic measurements will include an electric field of reference, $E_{ref}(t)$, measured without sample (signal propagating in air or reflected from a golden mirror), and a second measurement with the sample $E_{sample}(t)$. The Fourier transform of the temporal waveform gives the spectral distribution of the THz pulse in the frequency domain

$$\tilde{E}(\omega) = A(\omega)e^{-i\phi(\omega)} = \int dt E(t)e^{-i\omega t} \tag{2.5}$$

By recording the waveform of a THz pulse after its interaction with a target, and then

extracting its spectrum, it is possible to obtain the response of the target within the pulse-covered bandwidth. The spectral resolution of THz-TDS, $\delta\omega$, is determined as $\delta\omega = 2\pi/T$ by the temporal scanning range T, i.e., the range of temporal delays between the probe and pump pulses. The frequency range of the spectrometer is limited by the response of the THz source and detector, while mathematically it is significant within a bandwidth $\Delta\Omega = 2\pi/\delta t$. In order to have a smooth calculated spectrum, a zero padding technique should be applied. This adds several zero values on one or both sides of the THz waveform. This increases, mathematically, the temporal range T, thus giving more dense data points in the THz spectrum, but not providing any additional information or resolution.

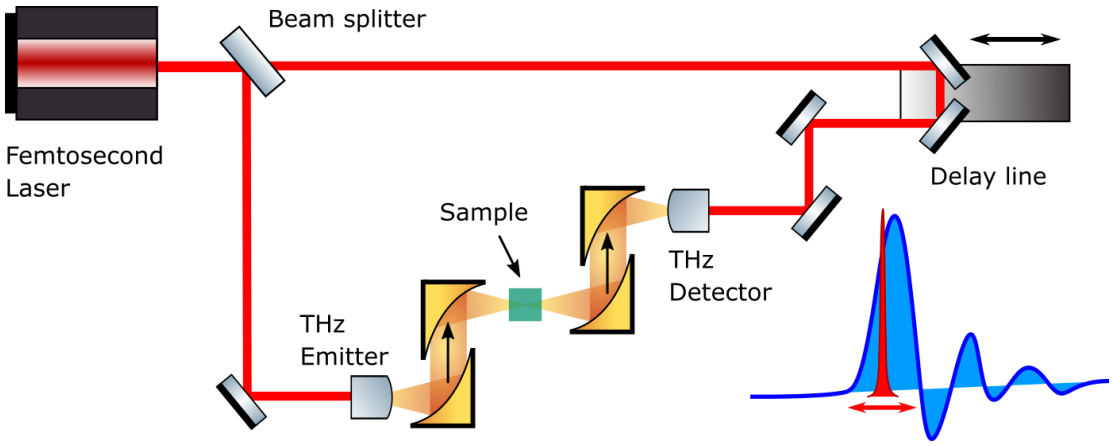

Figure 2.2: Optical alignment of a THz-TDS setup in a transmission geometry. The femtosecond pulse (red) is separated into two branches, respectively used for THz generation and detection. The generated THz pulse (orange) is focalized on a sample. The transmitted light is then sent to a THz detection system. The THz signal in time (blue shape sketch in the corner) is detected by sampling its entire waveform by changing its temporal overlap with the shorter probe pulse (red shape) on the detector. This is done by changing the delay line position along the detection optical branch.

2.1.3 Pump-Probe Spectroscopy

Since the THz generated for TDS is perfectly time-synchronized with the optical pulse that generates it, THz-TDS is also ideally suited for nonlinear pump-probe experiments. Ultrafast spectroscopy provides the possibility to temporally resolve phenomena in quantum matter at the fundamental time scales of atomic and electronic motion. Subpicosecond temporal resolution combined with spectral selectivity enables detailed studies of electronic, spin, and lattice dynamics, and, most importantly, the correlations between these degrees of freedom. This includes phenomena such as electron-phonon coupling,

charge density-wave dynamics, condensate recovery, and quasiparticle formation. In optical pump-THz probe experiments, an ultrashort pump pulse photo-excites a sample inducing a dynamical response. This behavior is expected to change as a function of the pump fluence and wavelength. Its effect to the low energy THz response is monitored with a time delayed THz probe pulse.

Formally, in the low-fluence regime ($\leq 100\ \mu J/cm^2$), pump-probe experiments can be described in terms of the third-order nonlinear susceptibility. However, better insights on the physical problem under study are often obtained by considering pump-probe as a modulation spectroscopy, where the self-referencing probe beam measures the induced change in reflectivity $\Delta R/R$ or transmission $\Delta T/T$[60]. This provides an important connection with linear frequency resolved optical spectroscopy, from which the reflectivity is measured and the dielectric responses are extracted. The comparison gives insights on the possible modifications of the microscopic properties induced by the optical pump. In femtosecond pump-probe experiments, the dynamics can be interpreted following the equation for the relative variation of R (a similar equation can be written for T)[61]

$$\frac{\Delta R}{R}(t) = \frac{\partial \ln(R)}{\partial \epsilon_1}\Delta\epsilon_1(t) + \frac{\partial \ln(R)}{\partial \epsilon_2}\Delta\epsilon_2(t) \tag{2.6}$$

where $\Delta\epsilon_1$, $\Delta\epsilon_2$ are the induced changes in the real (ϵ_1) and imaginary (ϵ_2) part of the dielectric function, respectively. In some materials the pump pulse creates a non-thermal electron distribution at times so fast that there is no coupling to other degrees of freedom. During the first 100 fs, the non-thermal distribution relaxes primarily by electron-electron scattering (see Fig. 2.3). This process cannot be probed by THz pulses, due to their intrinsic temporal length of the order of picoseconds. Subsequently, the excited Fermi-Dirac distribution thermalizes through coupling to the other degrees of freedom. However, other non-electronic responses can also appear, like the direct excitation of collective modes. All these results can be interpreted as a dynamic modulation of the optical conductivity tensor, although sometimes also the connection with Raman scattering is important for certain experiments.

For pump energies higher than the material band gap, it is possible to consider the dynamics largely in terms of the band structure, where photo-excitation leads to changes in band occupation followed by subsequent relaxation processes. The situation can be considerably more complicated in correlated materials starting with the fact that the electronic structure varies with occupancy. Thus, an excitation pulse can initiate a sequence of dynamical events quite different in comparison to the relaxation of a non-thermal electron distribution in a rigid band[61]. Generally, a delicate balance between various degrees of freedom occurs. Consequently, many correlated materials teeter on the edge of stability and exhibit gigantic susceptibilities to small external perturbations[62].

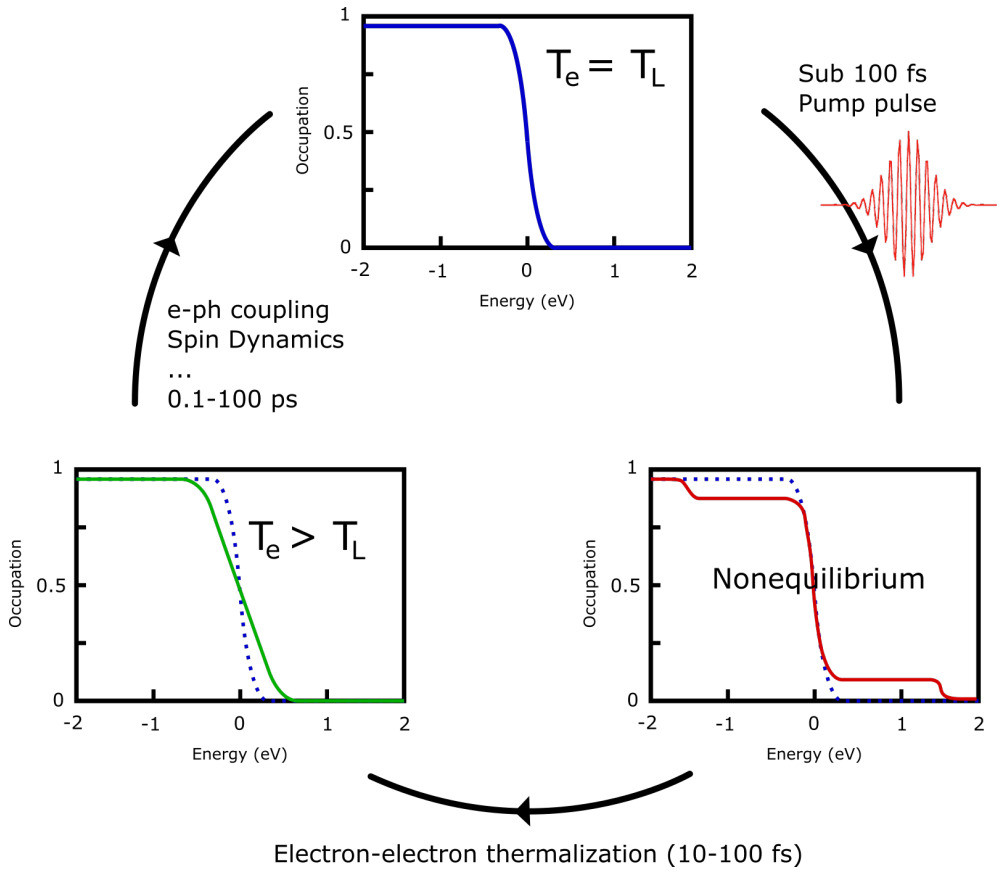

Figure 2.3: Schematic description of electrons dynamics pumped by a femtosecond pulse. Before photoexcitation, the system is at equilibrium as the electron temperature (T_e) is the same as the lattice one (T_L). Photoexcitation creates a nonthermal electron distribution that relaxes initially through electron-electron thermalization. The electrons excess energy is then transferred to other degrees of freedom on characteristic time scales ranging from 1 ps for electron-phonon relaxation to tens of picoseconds for processes such as pair recovery across a gap. The figure is adapted from ref.[61].

2.2 Terahertz Sources

Incoherent THz light is naturally emitted by thermal gray bodies and can be analyzed using a standard Michelson interferometry optical setup. However, due to the low brilliance of these light sources, expensive detection mechanisms are required to resolve the THz spectrum with a high signal-to-noise ratio. Better alternatives can be found in the generation of THz impulses, whose technology has spearheaded THz research for the past few decades. Optical generation of THz radiation using lasers, either pulsed or c.w., falls into two general categories. The first involves generating an ultrafast photocurrent in a photoconductive switch or semiconductor using electric-field carrier

acceleration or the photo-Dember effect[63,64]. In the second category, THz waves are generated by nonlinear optical effects such as optical rectification (limited to femtosecond laser excitation), difference-frequency generation (DFG) or optical parametric oscillation. Current nonlinear media receiving attention are crystals like DAST, HMQ-TMS and $LiNbO_3$[65,14,66]. Another intriguing optical THz generation method is ambient air-plasma generation[67,68]. Here, an intense pulsed laser induces an air plasma, which emits THz radiation. Recent advances in nanotechnology have also led to the development of semiconductor based THz sources: the THz-QCL (quantum cascade laser)[57], where continuous THz waves are emitted by means of electron relaxation between subbands of quantum wells.

Any process that creates a time-dependent change in the material properties like conductivity (σ) can act as a source term that results in emission of THz radiation. For THz generation using photoconductive switches, an ultrashort pulse incident on a semiconductor causes rapid transient changes to the macroscopic material properties represented by the microscopic responses. In particular, the rapid, optically induced change in σ on a femtosecond time scale is the origin of ultrafast THz pulses generated through photoconduction as well as the physical mechanism by which the THz pulses are detected. However, different processes for the production of THz, like the changes in σ and optical difference frequency generation, are not easily separable and can both contribute. A point to highlight while generating THz radiation is the time-evolution difference between the optical pulse and the generated THz one. The shape of the latter, in fact, is nearly a single cycle oscillation, thus many simplifying assumptions in nonlinear theory, like SVEA (Slowly Varying Envelope Approximation), are not satisfied[69].

2.2.1 THz Generation from Nonlinear Crystals

Rectification sources for THz generation rely on the $\chi^{(2)}$ of some materials, like ZnTe, DAST or HMQ-TMS[14,70]. For the measurements developed in this work, both ZnTe and DSTMS crystals have been used to develop transmission THz-TDS measurements to probe the nonlinear response of quantum materials. In the plane wave approximation, the THz field generated through optical rectification in these materials can be written as a function of the pump wavelength λ and spectral amplitude $I(\omega)$[71]

$$E_{THz}(\omega,\lambda,L) = \frac{2d_{THz}\omega^2 I(\omega)}{\left(\frac{\omega}{c}(n_{THz}+n_g)+i(\alpha_{THz}/2+\alpha)\right) n\epsilon_0 c^3}\cdot L_{gen}(\omega,\lambda,L) \tag{2.7}$$

where L is the crystal thickness, n_{THz} and α_{THz} the index of refraction and absorption coefficient at THz frequencies $\omega_{THz}=\omega$ for the nonlinear crystal, while n and α are the index of refraction and absorption coefficient at the λ wavelength. Finally, d_{THz} is the nonlinear coefficient associated to the THz generation. The second term in Equation 2.7 has a unit of length and its maximum, in case of negligible absorption, is reached at phase matching, i.e. $n_{THz}=n_g$, where n_g is the group velocity at λ. Its absolute value

is referred to as the effective generation length

$$L_{gen}(\omega, \lambda, L) = \frac{e^{i(\frac{\omega}{c}n_{THz}+i\alpha_{THz}/2)L} - e^{i(\frac{\omega}{c}n_g+i\alpha)L}}{\frac{\omega}{c}(n_{THz} - n_g) + i(\alpha_{THz}/2 - \alpha)} \tag{2.8}$$

The generated THz pulses are so short that it is impossible to detect them with a simple photoelectric scheme. Thus, the method used is based on an electro-optic effect, that is the Pockel's effect produced in nonlinear crystals like Zincum Telluride (ZnTe) or Gallium Phosphate (GaP). The initial E_ω laser pulse is splitted into a pump and a probe signal. The former produces the THz beam that acts on the crystal as a static field, inducing a birefringence effect that produces a polarization rotation of the probe beam that passes through. Its modified linear polarization into an elliptic one is initially sent to a quarter wave-plate, used to balance out the unperturbed linear polarization, and then is decomposed by a Wollaston prism to reach a balanced detector which measures the difference of the linear components, I_x and I_y. Without the static field, $I_x = I_y = I_0/2$. Instead, when the THz impinges on the crystal the detector reads $I_y = (1 + \Delta\phi)I_0/2$ and $I_x = (1 - \Delta\phi)I_0/2$, with $\Delta\phi$ directly related to the static electric field through the electro-optic coefficient r_{41} and crystal thickness L[72]:

$$\Delta\phi(t) = \frac{\omega_0 L}{c} n_O^3 r_{41} E_{THz}(t) \tag{2.9}$$

where n_O is the ordinary index of refraction of the EO crystal at the optical frequency ω_0. This result is a linear approximation for the phase difference.

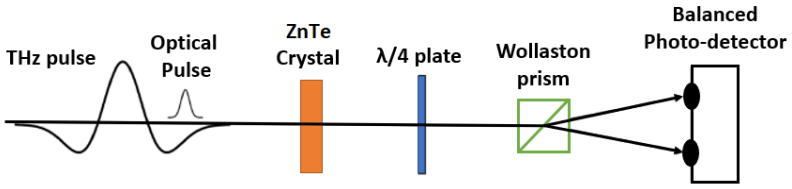

Figure 2.4: Scheme of an electro-optic detection based on ZnTe. The thicker the ZnTe crystal, the higher the polarization rotation effect. However, shorter crystal thicknesses grant a lower deformation of the spectral band as caused by dispersion.

2.3 Experimental Setups Characterization

Different experimental techniques and setups have been used for the optical characterization of the quantum materials studied in this thesis. Frequency resolved spectroscopic measurements have been performed through the use of two instruments: a Michelson interferometer (Bruker Vertex 70v), for infrared and far-infrared spectral range, and an

optical spectrometer (JASCO v-770) for the VIS-UV wavelengths. Both the setups can be used for reflection and transmission measurements. The interferometer can be coupled to a He-cooled ARS cryostat and a liquid He-cooled bolometer. The former permits precise temperature-dependent measurements, while the latter extends the spectral range to the THz region (20 cm^{-1} up to 600 cm^{-1}). A room-temperature pyroelectric detector is instead used for higher frequencies. The Michelson interferometer experimental scheme is shown in Fig. 2.5 in a transmission geometry.

Room temperature transmission measurements have been extended to sub-THz frequencies through a PCA-based time-domain THz system. A 800 nm wavelength optical pulse (780 nm Toptica FemtoFiber Pro, 80 fs, 80 MHz repetition rate) is used to pump two photoconductive antennas (Hamamatsu-G10620 series) in order to generate and detect THz radiation. The light is collimated and then focused through TPX plano-convex lenses on the sample. The transmitted signal is then again collected and focused on the second PCA. The current generated is filtered electronically through a lock-in amplifier. The entire system is enclosed in a container for nitrogen purging to remove the strong water absorptions coming from bare air.

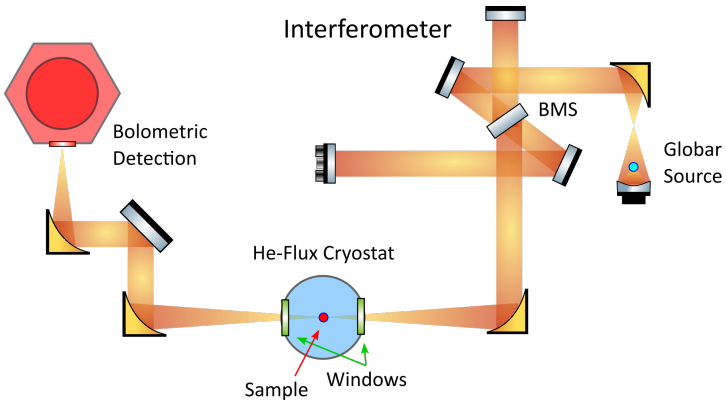

Figure 2.5: FTIR transmission geometry. A globar radiation source is sent to a Michelson interferometer and then focused on a sample between the cryostat transparent windows. The collected signal is then sent to a bolometric detection apparatus.

2.3.1 Nonlinear THz Spectroscopy

A second THz time-domain setup concerns the production of high intensity THz pulses through the optical rectification in a DSTMS organic crystal, as discussed in the previous section. A 15 femtoseconds high-intensity pulse at 800 nm, as generated by a vitara-UBB modelocked Ti:Sapphire Laser from Coherent©, is first amplified by a chirped pulse amplificator (Coherent© Verdi G-series), reaching a final power of nearly 7 W with a repetition rate of 1 kHz, while broadening the pulse in time up to 35 fs. This same pulse is used as an input in a collinear optical parametric amplifier (OPA) (TOPASprime from

Light Conversion©), permitting the production of femtosecond pulses at tunable IR wavelengths, going from 1100 nm up to 2300 nm. By fixing the wavelength emission at 1500 nm, in accordance with the phase matching condition for the THz generation in DSTMS crystals, the emitted pulse from the OPA, with a power of nearly 800 mW (with a fluence nearly 4 mJ/cm^2), is used to pump the organic crystal. The THz electric field is detected in a time-domain experimental configuration through an electro-optical sampling in a GaP crystal, by chopping the THz signal at a frequency of 500 Hz and integrating the detected signal electronically through a Boxcar averager. The intensity of the generated field can reach 2 MV/cm when focused to dimensions lower than 1 mm in diameter. Fig. 2.6 depicts the generation setup. Fig. 2.7 shows the THz signal and the measured spectral amplitude, along with a picture of the THz focus at the sample position, as obtained from a THz pyroelectric camera (Ophir Pyrocam IIIHR). The pulse energy has been monitored using a calibrated pyroelectric detector (Gentec-eo), chopped at 50 Hz, and its control has been achieved through a two polarizer series, where the second is maintained fixed to avoid polarization variations on the samples and EO detection crystal. The setup in enclosed in a rigid container for nitrogen purging.

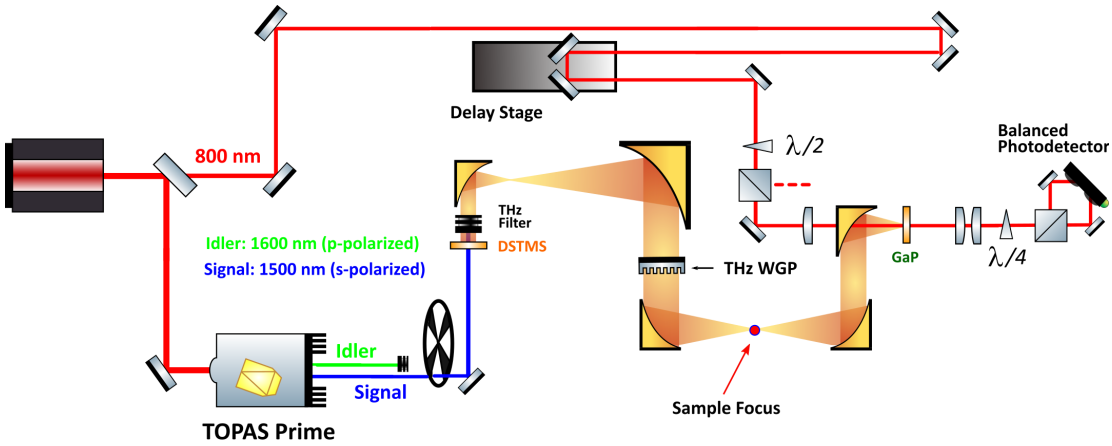

Figure 2.6: Optical setup for the generation of high-fluence THz pulses from the optical rectification in a DSTMS organic crystal. A 30 fs high-fluence pulse at 800 nm is separated into two branches, respectively for generation and detection. The generation branch is used as a seed in an optical parametric amplifier (OPA) (TOPASprime from Light Conversion©) for the generation of ultrashort pulses (∼80 fs) centered at 1500 nm. The residual idler pulse at 1600 nm is blocked. The 1500 nm signal is used to pump a DSTMS crystal (0.5 mm thick) with optical axis parallel to the pump polarization for the maximum generation efficiency. The THz signal propagates in dry air through a telescope and two wire-grid polarizers for fluence tuning. It is then focalized on a sample and transmitted in a normal incidence geometry. The transmitted signal is measured through an electro-optical detection based on a GaP crystal.

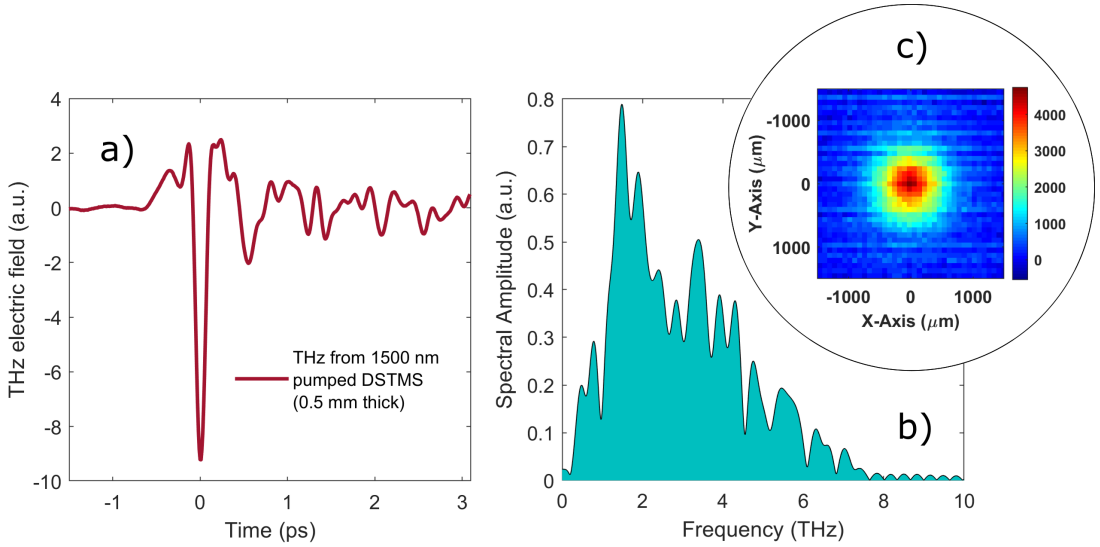

Figure 2.7: THz generation from a 0.5 mm thick DSTMS crystal pumped at 1500 nm. **a)** Waveform of the THz electric field measured through an electro-optical detection based on a GaP crystal. The voltage peak reaches magnitudes of 2 MV/cm. **b)** Spectral amplitude of the signal in a). The band extends up to 7 THz. **c)** THz focus at the sample position, as obtained from a THz pyroelectric camera (Ophir Pyrocam IIIHR).

2.3.2 Optical pump-THz probe Setup

A further THz-TDS setup based on the optical rectification in a ZnTe (110) nonlinear crystal is used to perform optical pump-THz probe spectroscopic measurements. Fig. 2.8 shows the experimental setup. The THz signal covers a range of frequencies going from 0.6 THz to ∼2.5 THz and is generated by the ultrashort 800 nm pulse as obtained by the Ti:Sapphire generation, with a repetition rate of 1 kHz. The optical signals used to pump the samples along with the THz probing are obtained from the 800 nm itself which can be used directly or sent to the OPA for the generation of 1300 nm and 2000 nm wavelengths. A 400 nm pump has also been obtained from the second harmonic generation of the 800 nm signal into a BBO nonlinear crystal. The sample is illuminated by the pump in a non-collinear geometry to avoid propagation to the detection scheme. The pump is also kept collimated in order to fit the entire THz focus in the photo-excited area. The pump fluence is controlled through the introduction of variable attenuators. The time delay between the pump and probe in achieved through a delay stage. Variations in the THz signal as a function of the pump-probe delay are monitored by fixing the THz detection delay to the highest peak of the THz electric field. Therefore, the pump-probe delay is scanned continuously by varying the pump delay stage up to 600 ps (∼200 mm). The pump signal is chopped at a frequency of 500 Hz, and the THz signal is integrated through a Boxcar averager. Complete THz scans can be also performed at fixed pump-probe time delays by chopping the THz signal and

fixing the pump delay stage at a specific pump-probe time delay.

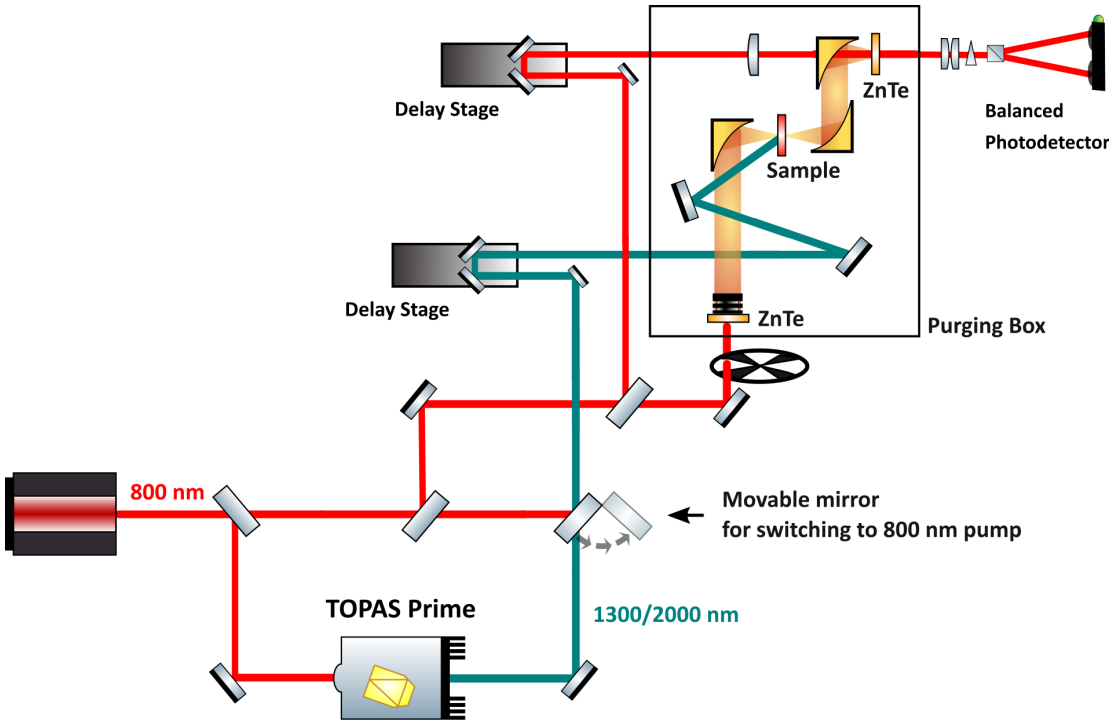

Figure 2.8: Pump-probe optical setup for the generation and detection of THz radiation synchronized in time to optical pumps at different wavelengths. A 30 fs high-fluence pulse at 800 nm is splitted and used as a seed for both the generation of THz from a ZnTe crystal (500 μm thick) and NIR ultrashort pulses from an optical parametric amplifier (OPA) (TOPASprime from Light Conversion©). The optical pulses can be used once at a time to perform optical pump-THz probe measurements in a transmission geometry. Four wavelengths can be used for pumping: 400 (second harmonic of the seed in a BBO crystal), 800 (seed), 1300 (OPA signal), and 2000 (OPA idler) nm. The THz generation and propagation is enclosed in a purging box for a low humidity environment. The transmitted THz signal is measured through as electro-optic detection based on a second ZnTe crystal.

Part I

Spectroscopy of Magnetic Quantum Materials

The dynamics of conduction electrons and collective excitations in magnetic solids is an attractive research topic due to its dual interest in the discovery of new fundamental phases of matter and technological applications. Among the quantum materials classification, intrinsic magnetic features are of great importance due to the breaking of time-reversal symmetry, which is related to a series of interesting effects like the protection of the helical states in 3D topological insulators, or the presence of giant magnetoresistance in topological semimetals and some oxides. These latter systems have already found industrial applications. The magnetic order in complex quantum systems might also couple with the other electronic or lattice degrees of freedom, inducing changes in the material's susceptibility to external stimuli. For instance, 2D magnetic materials are of interest for their possibility to be used in complex heterostructures to induce proximity effects, with applications in novel spintronic designs. This second part of the thesis will focus on the optical characterization of three magnetic quantum materials: Co_2MnGa, a nodal/Weyl topological semimetal, $MnBi_2Te_4$, a magnetic topological/axion insulator, and CrI_3, a Van der Waals layered ferromagnet. Transmission and reflectance optical spectroscopy cannot directly probe the magnetic order of these systems. However, the direct coupling of the magnetic features with the electronic and lattice degrees of freedom leaves striking fingerprints in the optical conductivity or Raman tensor. These can be highlighted by optical spectroscopy, giving important insights on the coupling mechanisms in act.

Chapter 3

THz Response of Optically Driven Co_2MnGa Thin Films

Since the breakthrough discovery of topological materials, several intriguing effects related to the topological nature of their electronic band structure have been highlighted theoretically and experimentally. Magneto-electric and thermo-electric effects, like the anomalous Hall and Nernst effects[73–76], or the enhanced nonlinear optical responses, like multiple harmonic generation (MHG)[77–79] and linear/circular photogalvanic effects (L/CPGE)[80,81], are just a few of the novel properties found in these materials that can be exploited in future electro-optical applications. More recently, topological materials presenting a time-reversal symmetry breaking provide novel topological phases of matter, like the magnetic topological insulators[41,23,82] and semimetals[83–85] and the axion insulators[76].

The full-Heusler alloy Co_2MnGa (CMG) is a ferromagnet with a Curie temperature higher than 600 K, that crystallizes in the cubic Cu_2MnAl-type structure with space group $Fm\bar{3}m$[86,87]. CMG has been theoretically predicted[88,89] and experimentally proved[90] to be a magnetic topological nodal line semimetal, showing a complex structure where the valence and conduction bands cross along arbitrarily intertwined nodes[5,91]. Moreover, the intricate nodal structure of CMG was revealed to contain Hopf links and show unconventional density of states and band structure[90,89], which have led to enhanced perspectives for non-linear optical responses and higher harmonic generation (HHG)[92–94].

Despite the promising properties of CMG, not much is known about its electronic properties and the corresponding optical properties[95–99]. Moreover, it is so far unclear what distinct experimental signature corresponds to nontrivial band topology[100]. Anomalous Hall[101] and Nernst[102,103] effects have been reported as a measure of the topological features, along with THz Faraday rotation[104]. Recent theoretical results have suggested that the HHG effect, related to the exotic nodal geometry, might be enhanced drastically by the topological curvature[100]. In this framework, optical linear and nonlinear spectroscopy are key tools for the characterization of the electronic features of these semimetals. Photoconductive responses have been used to study the photocarrier scattering mechanism governed by the unique band structure in Dirac semimetals[105–109] and

graphene[110,111], highlighting the dynamical interaction between the various degrees of freedom. Moreover, a further mechanism coupling to the topology of the band structure is the production of photocurrents (shift currents) through the linear/circular photogalvanic mechanism[77,80,81]. In Weyl semimetals[112–115] and topological insulators[116,117], it has been demonstrated how this effect generates polarization-sensitive THz radiation from both the bulk and surface states. In centro-symmetric materials like CMG, where parity conservation forbids bulk second-order non linear phenomena, THz emission is an optimal probe of the surface states, thus giving a direct probe of the topological features of the material.

In this chapter, the optical properties of CMG thin films with different thicknesses, ranging from 10 nm up to 80 nm, and grown on MgO (100) substrates are studied. Five high-quality epitaxial thin films with different thickness (10, 20, 40, 60 and 80 nm) of Co_2MnGa were grown in a BESTEC UHV magnetron sputtering system on single crystal MgO(001) substrates and capped in-situ with 3 nm Al, whose surface naturally oxidizes at ambient conditions. The cubic crystal structure of CMG is shown in Fig. 3.1a. The structure is understood as being the result of four interpenetrating face-centered-cubic (fcc) lattices (Heusler alloy structure).

3.1 Frequency-dependent Optical Conductivity

Reflectance (R) and Transmittance (T) of all the films have been measured at room temperature in a broad spectral range from THz (20 cm^{-1}) to UV (50000 cm^{-1}) ($\sim$ 2.5 meV – 6.2 eV). The measurements at room temperature were taken through a Vertex 70v FTIR broadband interferometer, covering the spectral range from THz (40 cm^{-1}) to MIR (7000 cm^{-1}), and through a Jasco V-770 spectrometer, extending the spectral data from 5000 cm^{-1} up to the UV region (50000 cm^{-1}). In Fig. 3.1b,c the real and imaginary part of the films conductivity are reported across the broadband spectrum, as extracted through a Kramers-Kronig consistent fitting process of the film response in a trilayer air/film/substrate system[118].

The optical conductivity is dominated by a Drude term up to the infrared range, whose spectral weight (SW) is shown in Fig. 3.1d as a function of thickness. The sharp peak at $\simeq$ 260 cm^{-1} can be attributed to a CMG phonon[119]. At higher frequencies, from 3000 to 20000 cm^{-1}, the interband contributions to the conductivity highlight the presence of some differences in the band structure, in particular for the thinner (10 nm) film. These differences are also reproduced in the SW (see Fig. 3.1d) and can been associated to the strains induced onto the film by the MgO substrate[101]. DFT results have also suggested the absence of the Co-Mn termination surface state in 10 nm films[97]. Increasing the thickness up to 20 and 40 nm, the conductivity acquires a strong metallic Drude term whose SW saturates for the 60 and 80 nm (see Fig.3.1d). Fig. 3.1e shows the comparison of the 80 nm conductivity to DFT calculations for the bulk CMG[97]. The experimental interband and Drude contributions closely resemble theoretical values, suggesting a bulk-like response of the thicker films (60 and 80 nm). However, a major energy shift is clearly visible. Such a shift was proved to converge

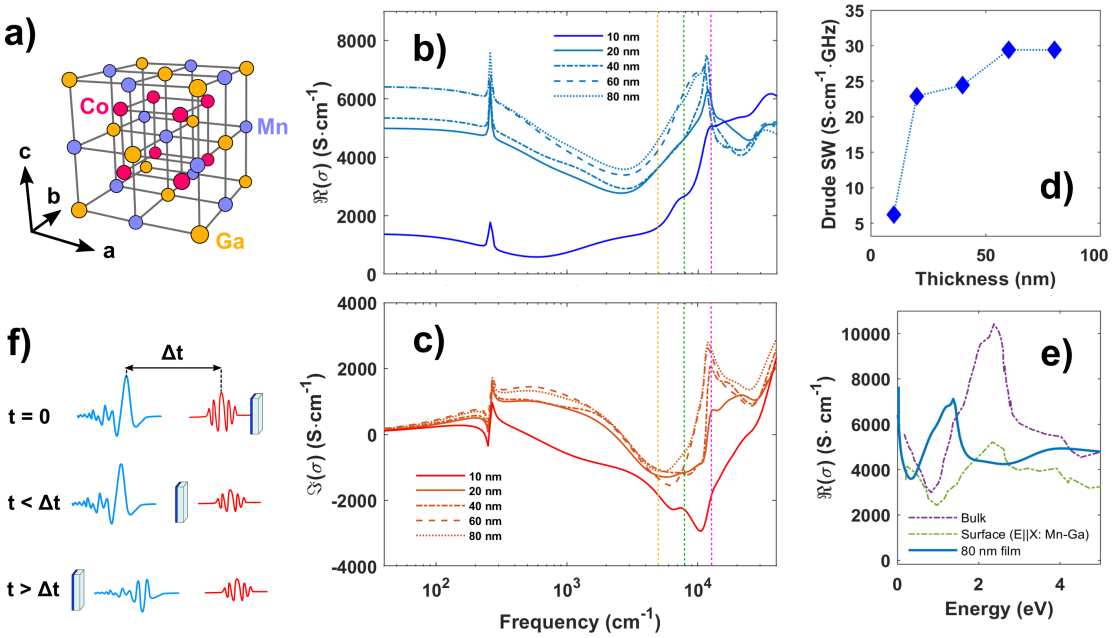

Figure 3.1: Linear optical response of Co_2MnGa thin films. **a)** Cubic unit cell of a Co_2MnGa crystal. The arrows indicate the crystal axes. **b-c)** Real and imaginary part of the optical conductivity of CMG films with different thickness, from THz to UV. The vertical dotted lines highlight three different wavelengths: 2000 nm (yellow), 1300 nm (green), 800 nm (pink). **d)** Drude spectral weight as a function of thickness, showing the convergence to a bulk behavior. **e)** Comparison between the experimental real conductivity (80 nm film) and DFT calculations[97]. The energy shift can be associated to the strong electron correlations[98]. **f)** Optical pump-THz probe spectroscopy measurements. The THz signal (light blue) is transmitted across the sample at a time Δt after the arrival of the optical pump (red). Varying Δt permits to sample the out-of-equilibrium dynamics of the low energy electrons.

down to the experimental values once a U term of nearly 5.4 eV is taken in mind the DFT+U calculations[98]. At 20 and 40 nm, the conductivity spectral weight shrinks by nearly 20%, while the interband features suggest a shift of the spectral contributions toward higher frequencies. Both these differences can be associated to the increase in strain effects on the film with decreasing thickness, inducing modifications in the electronic band structure. Indeed, similar differences among the film thicknesses are also confirmed by the study of the topological features, as suggested by magneto-optical measurements[101,104] and THz emission spectroscopy (see section §3.3). In the next sections, the time-domain sub-ps response of the CMG films is studied through pump-probe and THz emission spectroscopy. Optical pump-terahertz probe measurements are developed in a transmission geometry as explained in section §2.3.2.

3.2 Optical Pump-THz Probe Spectroscopy

To study the temporal dynamics of the charge-carriers in a sub-ps time scale, three different optical pumps at 800, 1300 and 2000 nm (see Fig. 3.1f) were applied. The photoinduced current is then probed by a THz pulse in a transmission configuration. More specifically, the transmitted THz electric field change $\Delta E_t = E_t - E_0$ is measured as a function of the pump-probe delay time Δt between the optical and THz signal, where E_t and E_0 denote the peak value of the THz electric field at a delay time t and without the pump, respectively. Due to the low transmission percentage of the 60 and 80 nm films, only the 20 and 40 nm samples have been studied. In the thin film approximation, the photoinduced relative transmission change $\Delta E_t/E_0$ is proportional to the THz negative photoconductivity (PC) $-\Delta\sigma_1/\sigma_1$, where σ_1 is the real part of the optical conductivity.

Fig. 3.2a shows $\Delta E_t/E_0$ for the two films (red curve 20 nm, blue curve 40 nm) at a fixed pumping wavelength of 1300 nm and 710 $\mu J/cm^2$. The time axis is separated to highlight the temporal behavior in a short and long time window. Four stages for

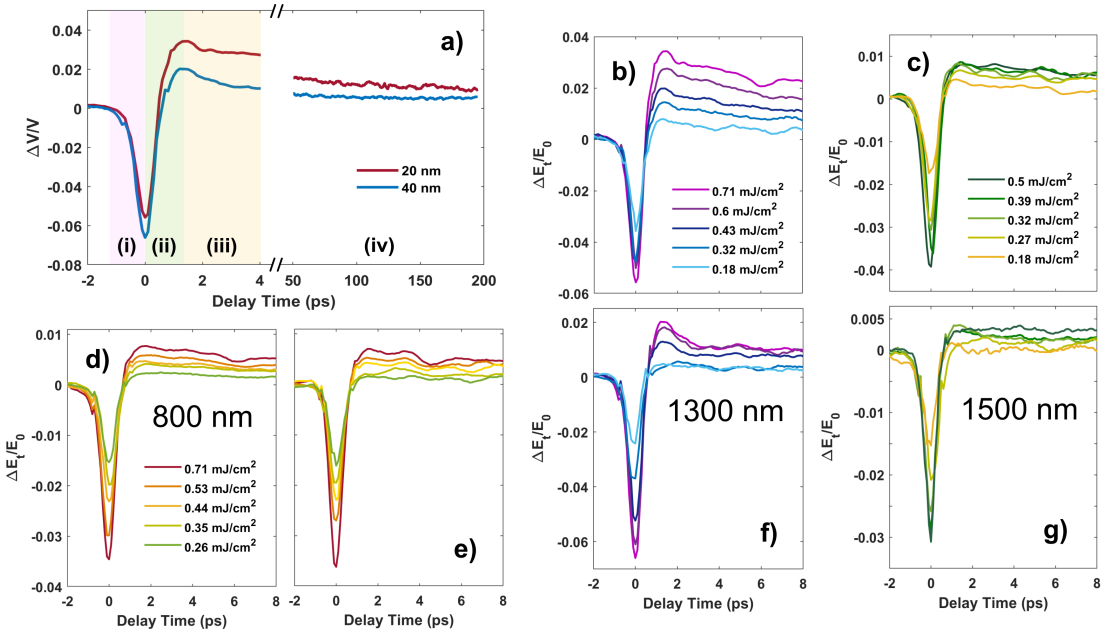

Figure 3.2: OPTP spectroscopy of Co_2MnGa thin films. **a)** Short and long time trend of the photoinduced THz peak transmission change. The colored boxed highlight the four steps process of transient excitation (i, ii) and relaxation to equilibrium (iii, iv). **b)-d)** OPTP measurements at three different pump wavelengths for the 20 nm thick sample. Five different fluences have been measured at each pumping wavelength. **e)-f)** OPTP easurements for the 40 nm sample. The fluences measured at each wavelength are equal to the 20 nm sample results (same curve colors).

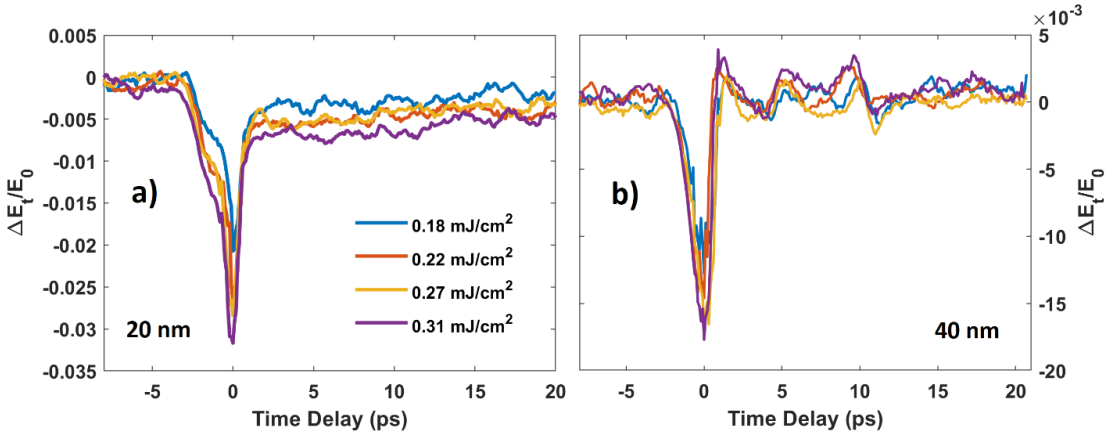

Figure 3.3: OPTP results for a pumping wavelength of 400 nm. a)-b) Photoinduced variation in the THz field transmitted after the pump at 400 nm for the 20 nm and 40 nm films, respectively.

the photoinduced response can be highlighted: (i) a first increase in photoconductivity (decrease in THz amplitude transmission); (ii) a second rapid (subpicosecond) transition to a positive PC; (iii) a fast (few picoseconds) decay process from the maximum PC value to a positive plateau; (iv) a slow (hundreds of picoseconds) recovery process to equilibrium. Figure 3.2b-d show the photoinduced THz transmission up to 8 ps for the 20 nm at the three pumping wavelengths (b: 1300nm, c: 2000 nm, d: 800 nm) and different pumping fluences. The same results are shown in Fig. 3.2e,f,g for the 40 nm sample. These results suggest a four-steps excitation and relaxation process for all the pumping wavelengths. The small coherent oscillations in the relaxation trend can be associated to the production of acoustic phonons, propagating back and forth through the sample thickness[120]. Pump-probe results are also obtained at 400 nm as shown in Fig. 3.3. However, due to the strong two-photon absorption processes of the MgO substrate, the results are plagued by the strong absorption of the MgO optical gap. Regardless of the problem, a similar response of the CMG films to the lower pumping wavelengths can be observed.

The origin of the four steps photoinduced change in THz conductivity can be associated to the changes in both the number of carriers (Δn) or a change in mobility ($\Delta\mu$). Due to the high carrier density of the metallic films, the former contribution is negligible even at the highest fluences measured (the number of photons, $< 10^{15}$, is negligible with respect to the number of carriers). In particular, form the absorption coefficient of the 40 nm film, it is possible to estimate $\Delta n(\lambda, d = 40\text{ nm})$ for the highest fluences of each wavelength λ as: $\Delta n(800\text{ nm}) \simeq 9.4 \times 10^{14}$, $\Delta n(1300\text{ nm}) \simeq 7.7 \times 10^{14}$, and $\Delta n(2000\text{ nm}) \simeq 4.5 \times 10^{14}$. Indeed, the sharp increase in absorption, appearing before the sub-picosecond transition to a NPC regime, is associated to a broadening of the Fermi distribution due to the interband transitions of electrons to higher energy levels, plus the increase in electron temperature induced by the e-e scattering processes.

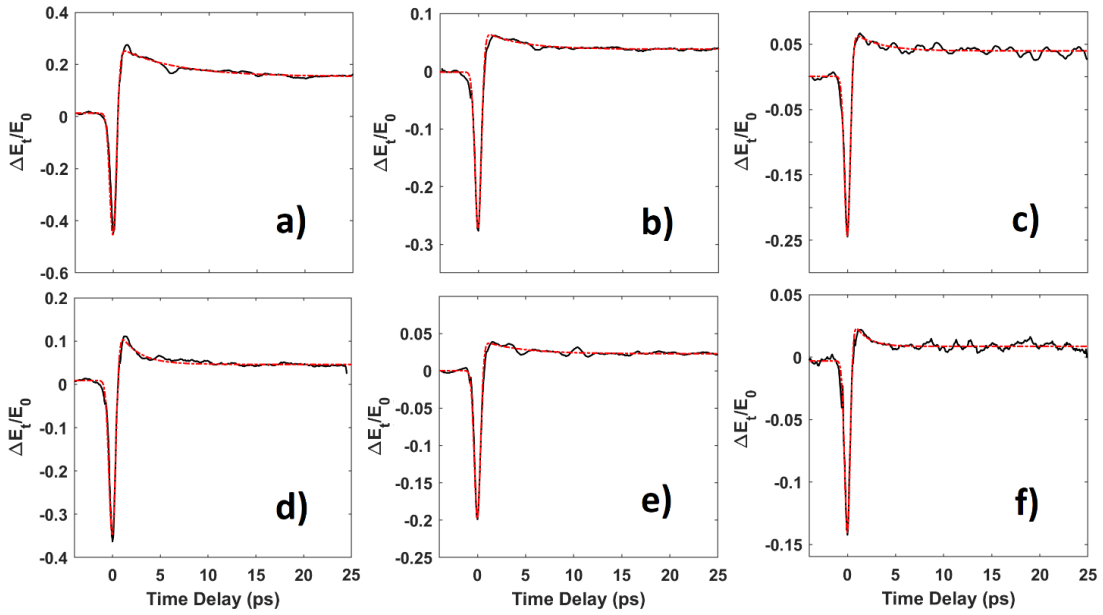

Figure 3.4: Fitting process of the OPTP results. a)-c) Fit of the 20 nm film response for the 1300, 800 and 2000 nm pumping wavelengths, respectively with fluences 0.71, 0.71, 0.39 mJ/cm^2. **d)-f)** Fit of the 40 nm film response for the 1300, 800 and 2000 nm pumping wavelengths, respectively with fluences 0.71, 0.71, 0.39 mJ/cm^2.

For the THz transmitted field, the NPC transition to positive values (ii step) can only be associated to a change in mobility for the carriers. Similar effects have been observed in materials such as graphene[121,122], Dirac semimetals[123], transition metal dichalcogenides[124] (TMDs) and perovskytes[125,126].

To analyze the data, the transient THz field transmission are fitted through a sum of two mono-exponential functions[123,127]

$$\frac{\Delta E_t}{E_0} = Ae^{-\frac{t}{\tau_{fast}}}\left[1-\text{erf}\left(\frac{w}{\tau_{fast}}-\frac{t}{2w}\right)\right]+ \tag{3.1}$$

$$+Be^{-\frac{t}{\tau_{slow}}}\left[1-\text{erf}\left(\frac{w}{\tau_{slow}}-\frac{t}{2w}\right)\right]+Ce^{-x^2/4w^2}$$

where τ_{fast} and τ_{slow} are the fitted relaxation times for process (iii) and (iv), respectively. The rise time from positive to negative PC is instead parametrized by w. The fitting process is highlighted in Fig. 3.4, from which the time constants for the four steps process are extracted. To describe the rapid change in mobility (ii), the production of polaronic quasiparticles in the CMG films is supposed. This assumption can be proved by looking at the time constants w and τ_{slow} for the steps (ii) and (iv). The change in mobility (ii) takes place on a sub-picosecond scale, with a time constant of the order of

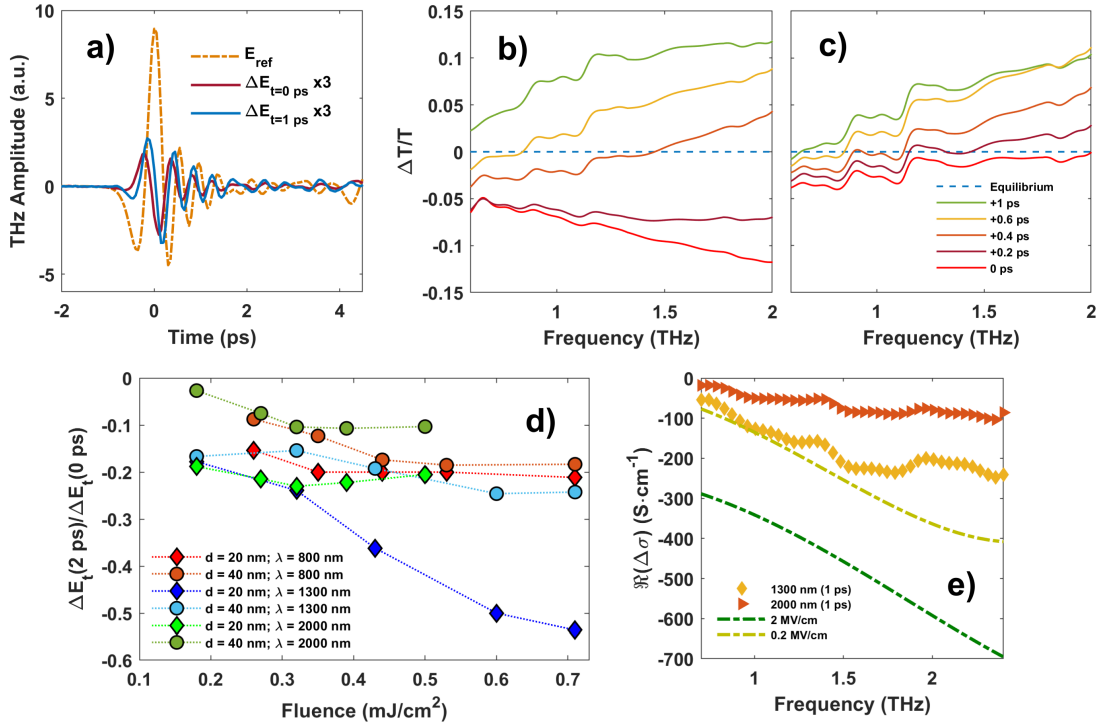

Figure 3.5: Polaron excitation in Co_2MnGa thin films. **a)** Photoconductive changes in the THz electric field transmitted by the 20 nm film after an optical pump at 1300 nm (0.71 mJ/cm^2 fluence). E_{ref} identifies the original signal transmitted without the pump application. **b)-c)** THz transmission change in the 20 nm film for different time delays between the optical pump at 1300 (b) and 2000 (c) nm and the THz probe. **d)** Ratio between the transmitted electric field change ΔE_t after (2 ps) and before the polaron formation (0 ps), as a function of fluence. **e)** NPC induced at 1 ps for the 1300 and 2000 nm pumping wavelength, compared to the NPC induced by strong THz pulses up to 2 MV/cm.

250 fs for all wavelengths and fluences. Similar time constants have been found for the polaronic formation in lead-iodide perovskites[125,126] and type-II Dirac semimetals[123]. Moreover, the slow relaxation process (iv), of the order of hundreds of picoseconds, suggests a very stable localization of the carriers, which can be related to the formation of polarons.

To better address the polaronic behavior, further measurements have been carried out by sampling the whole THz spectrum of the 20 nm sample at different pump delay times for the 1300 and 2000 nm wavelengths. Fig. 3.5a shows the photoinduced change (at 0 and 1 ps) in the whole THz electric field $\Delta E(t_s, t) = E(t_s, t) - E_{ref}(t_s)$ transmitted by the 20 nm film, where t_s is the electro-optical probing time of the THz scan, for the 1300 nm pump and 0.71 mJ/cm^2 pump fluence. A clearer picture of what is happening to the transmittance is shown in Fig. 3.5b,c for the 1300 and 2000 nm pumping wavelengths.

Here, the relative transmitted intensity across the 20 nm sample over substrate is plotted as a function of frequency for a sequence of pump delay times. This behavior suggests a frequency dependent NPC similar to the polaronic response found in Dirac semimetals[123], thus supporting the polaronic formation intuition in CMG.

3.2.1 Thickness and Pump Wavelength Dependence

Having explained step II and IV in terms of a polaronic formation, two additional questions remain: the physics behind the fast relaxation process of step III, and the subtle dependence with thickness and pumping wavelength of the photoconductivity. The former can be answered by looking at the relaxation times as extracted from the fitting process. All values fall on a temporal scale of a few picoseconds. Similar time constants have been found in other magnetic thin films[120,127,99], and can be associated to a fast electron-lattice or electron-spin-lattice thermalization. Indeed, a mixed phonon and magnon scattering state has been suggested by resistivity measurements[101].

To deal with thickness and pump wavelength dependence, instead, Fig. 3.5d shows a comparison between the polaronic formation in the 20 and 40 nm films at different wavelengths, comparing the ratio between the transmitted electric field change ΔE_t after (2 ps) and before the polaron formation (0 ps). The result suggests a stronger e-ph coupling in the thinner film. The data highlights also a stronger polaronic formation at the 1300 nm pumping wavelength with respect to the 800 and 2000 nm, for both thicknesses. To address the wavelength dependence of the ultrafast response, a simple model for the electron-phonon coupling based on the Fröhlich Hamiltonian can be proposed[128,129]. For a single polaron mode, the coupling constant γ of the model scales as $\gamma \propto 1/q$[130], where q is the wavevector of the coupling electron. Indeed, the polaron formation is stronger for carriers at the Γ point in the BZ. For CMG, the density of states at this point is zero at the Fermi level[103]. However, free carriers can be created by direct interband transition from the valence bands. At the Γ point these transitions are resonant for wavelengths close to 1300 nm, which is the pumping wavelength from which the highest polaronic response is obtained. The resonant behavior dampens at the 2000 nm pumping wavelength, corresponding to direct transitions away from the Γ point. The electrons pumped by this wavelength will thus see a weaker e-ph coupling, reducing the polaronic formation. At lower wavelengths like 800 nm, instead, the transitions can take place between multiple bands, smoothing out the resonance at the Γ point and resulting in a lower polaronic formation.

Finally, to address the higher e-ph coupling in the thinner film, two main contributions can be suggested: the stronger electron screening in the 40 nm film (see Fig. 3.1b), hindering the coupling with the lattice, and the enhanced strain effects in the 20 nm sample[120,131,132]. To highlight the latter effect, nonlinear THz transmission experiments were performed, where a strong THz pulse up to 2 MV/cm (see Fig. 2.7) is sent across the 20 and 40 nm films, studying the transmission as a function of fluence and THz frequency. As shown in Fig. 3.6, the 20 nm film hosts a nonlinear activation. This nonlinear effect coincides with a decrease in the optical conductivity at frequencies

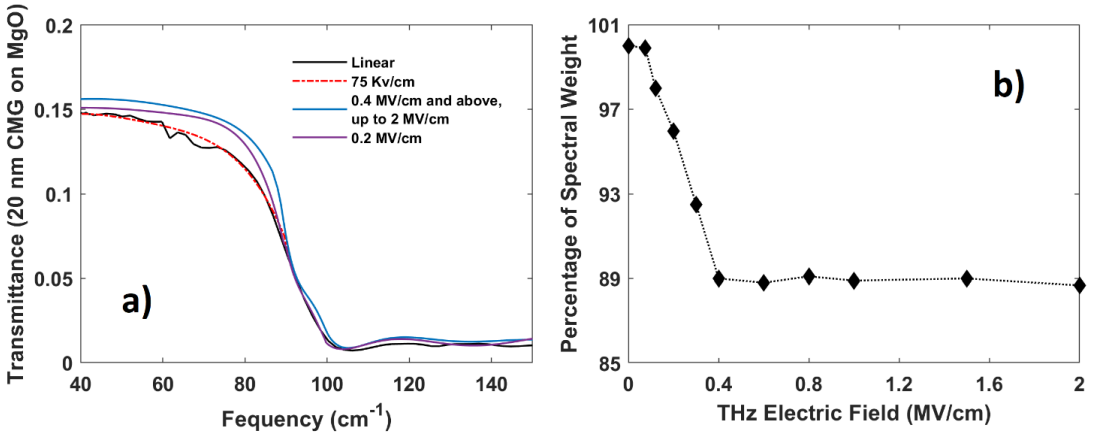

Figure 3.6: Nonlinear transparency of the 20 nm CMG film. a) Transmittance variations at different THz field magnitudes. **b)** Relative variation of the Drude spectral weight for the 20 nm CMG film, as a function of the THz field intensity.

comparable with the photoconductivity induced by the formation of polarons, as shown in Fig. 3.5f. This similarity suggests that the strong THz pulses, that produce strains on the CMG lattice, can induce a decrease in mobility similar to the one caused by the optical excitation. Differently from the 20 nm sample, thicker films do not show any change from the linear response. These results support the stronger polaron formation in the thinner film as a consequence of the lattice strain effects, which are known to be important in thinner films[101,99].

3.3 THz Emission Spectroscopy

A Strong support about the topological nature of the charge carriers in Weyl semimetals can be obtained through THz emission spectroscopy. Indeed, the production of photocurrents, as induced by topological effects like the L/CPGE, causes the emission of THz radiation in the direction orthogonal to the current propagation. Moreover, the THz radiation emitted from the optically generated ultrafast photocurrents shows a polarization parallel to the current propagation. Therefore, the direct measurement of the THz field amplitude and polarization allows to obtain useful information on the ultrafast current generation mechanisms. THz emission from CMG thin films was measured through the optical setup shown in Fig. 3.7a. The samples are pumped with a 800 nm ultrashort pulse (35 fs), as obtained by a Ti:sapphire amplifier (Coherent© Verdi G-series), with a repetition rate of 1 kHz. The pulse is sent on the films at a 45° angle geometry, and the THz signal is collected in reflection by a series of parabolic mirrors. The signal is then sent to a 250 μm ZnTe crystal for the electro-optical detection by a balanced photodetector. The crystal orientation was kept fixed for all measurements. Half and quarter wave-plates for the 800 nm signal were used to tune the incident

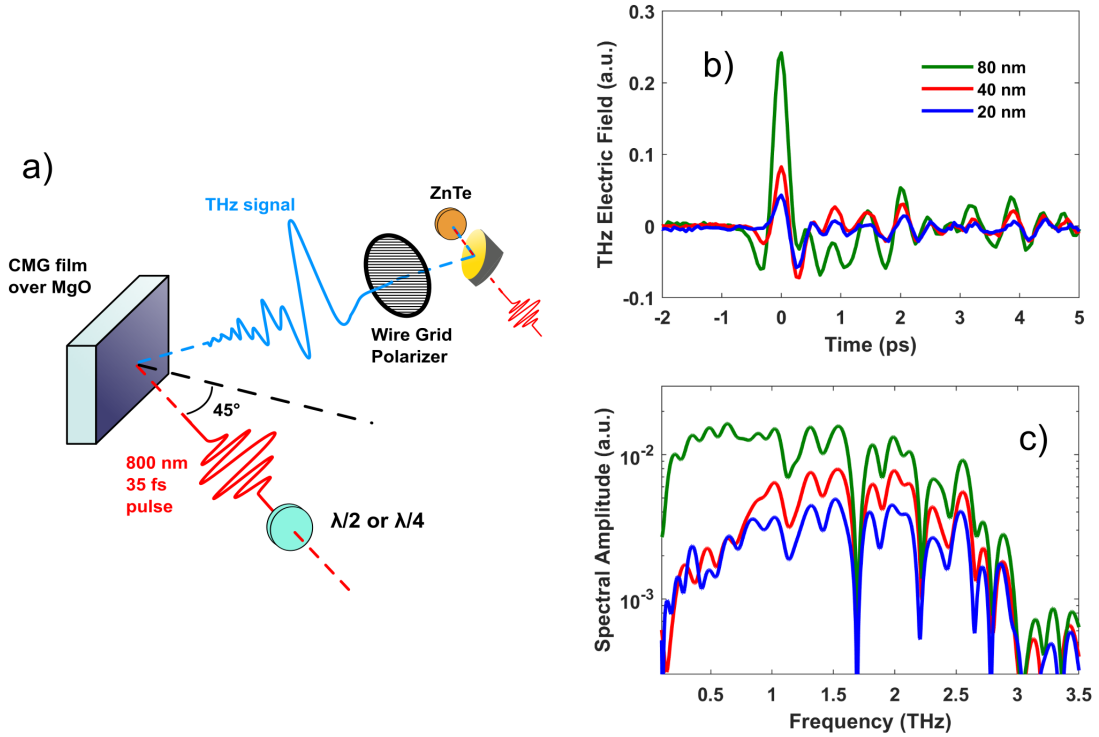

Figure 3.7: THz emission by optical excitation in Co_2MnGa thin films. a) Experimental setup for the generation and detection of THz waves from CMG thin films. Films are illuminated in a 45° reflection geometry by a 800 nm ultrashort pulse with tunable fluence and polarization. The THz detection is achieved through an electro-optical coupling by a ZnTe nonlinear crystal. **b)** THz electric field in time as emitted by three CMG films of different thicknesses. **c)** Spectral amplitudes of the THz signals, revealing the frequency emission band. Sharp dips are associated to the water vapour absorptions during propagation in air.

polarization, while a wire-grid polarizer was used to filter the THz signal polarization.

Fig. 3.7b shows the THz field emitted by the three films with different thicknesses, illuminated by a linearly S-polarized optical pulse with a fluence of 1.77 mJ/cm^2. The terahertz intensity (from the 80 nm film) is approximately 3% of that measured using a 500 μm thick ZnTe crystal under identical conditions (same exciting laser, illuminated area and fluence). Per unit thickness, the generation efficiency of the CMG film can be roughly estimated as hundreds of times higher than the ZnTe nonlinear crystal. Fig. 3.7c shows the spectral amplitude (SA) of the THz signals obtained through a fast Fourier transform (FFT) algorithm. The sharp dips between 1 and 3 THz are associated to water absorption from the atmospheric air. Due to the limitation of the ZnTe detection band, the THz signal emitted from the 80 nm film was also measured through a GaP crystal, able to detect the higher THz frequencies but less sensitive to the field intensity

due to the lower electro-optic coefficient[133]. Even in this case, the emitted spectrum shows a cut-off at nearly 3 THz, suggesting that the whole CMG THz emitted spectrum is confined below this frequency.

The THz emission described above provides fundamental information about topological effects in Co_2MnGa. Indeed, for nonlinear second-order responses (like the optical-rectification process), a non-centrosymmetric unit cell is required. This attribute does not apply to bulk CMG since, having a cubic structure, it keeps the parity symmetry intact while breaking the time-reversal one due to a Curie temperature higher than 600 K. Therefore, one expects a major contribution in the THz emission from topological surface states, where the parity symmetry is broken. However, as can be shown in the following analysis, a complex thickness dependence of the THz emission is found experimentally, revealing a further THz production mechanism originating from the bulk. Fig. 3.8a shows the ratio between the THz spectral amplitudes of the three films (SA(80 nm)/SA(40 nm) blue curve, SA(40 nm)/SA(20 nm) red curve). The dependency of the THz field with thickness appears indeed non-trivial across the full THz spectrum. SA(40 nm)/SA(20 nm) is nearly flat above 1 THz with a value $\simeq 2$ (doubled field), in agreement with the thickness ratio. A similar result is found for the ratio between 80 and 40 nm above 1 THz. However, below this frequency, the field increases rapidly for the 80 nm CMG film. Thinner films of 20 and 40 nm do not host a valuable difference in their generation in this sub-THz range, while the 80 nm film shows a sharp increase (nearly a factor 10) in the THz generation efficiency.

Below 1 THz, the spectral content of the films shows an anomalous increase vs. thickness, suggesting a distinct generation mechanism that cannot be linked to the bulk, but rather to the surface states. Indeed, as previously demonstrated, CMG films of thicknesses comprised between 20 and 60 nm display a thickness-independent magnitude of the anomalous Hall conductivity (AHC) of intrinsic origin (arising from Berry curvature)[101]. Whereas for the thickest film, of 80 nm, the AHC is found to increase by about 40%, and attributed to an enhanced intrinsic contribution from topological Weyl points and nodal lines, as supported by ab initio calculations[101]. The results for the sub-THz generation (see Fig. 3.8a) presents a behavior similar to AHC data as a function of thickness, thus suggesting a topological origin of this emission, as induced by a linear photogalvanic effect from the surface states.

Further differences between the 80 nm and the thinner films can be observed in Fig. 3.8b. Here, one shows the behavior of the THz electric field amplitude vs. the pump fluence F. All films show a first linear increase with F further followed by a saturation behavior. However, the saturation effect is faster for the 80 nm film than the other two thicknesses, which behave very similarly. This difference cannot be linked to the bulk response, as suggested by the equal saturation fluence effect for the 80 and 40 nm film reflectance (see inset of Fig. 3.8b), which is mainly determined by the bulk carriers. Indeed, the optical penetration depth at 800 nm is ~ 50 nm (as measured by transmission spectroscopy), comparable to the film thickness. The faster THz saturation effect vs. F in the 80 nm film can then be related to its surface contribution, being dominant with respect to the bulk response due to the higher Berry curvature as measured by AHC.

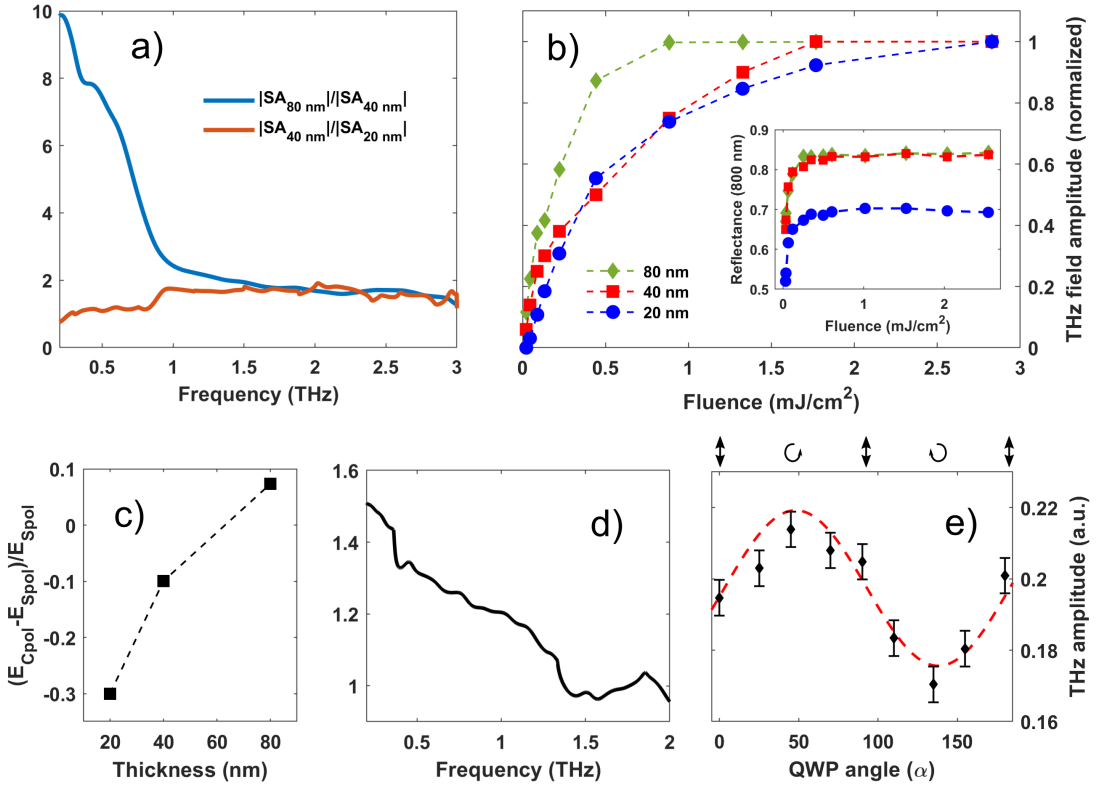

Figure 3.8: Fluence and Polarization dependence of the THz emission from Co_2MnGa thin films. a) Ratios between the 80 nm and the 40 nm spectral amplitudes (blue) and between the 40 nm and 20 nm spectral amplitudes (red). **b)** Fluence dependence of the emitted THz amplitude. The inset shows the nonlinear enhancement of the films reflectance at 800 nm. **c)** Ratio between the THz peak-to-peak amplitude emitted after a linearly (S-pol) and circularly polarized 800 nm pulse. **d)** Ratio between the THz spectral amplitude generated by a 80 nm CMG film when pumped by a circularly over linearly (S-pol) polarized beam. **e)** THz field amplitude from the 80 nm film illuminated by an optical pump with variable polarization, as modified by a quarter waveplate (of angle α). An angle $\alpha = 45°$ identifies a left-circularly polarized light, while $\alpha = 135°$ a right-circularly polarized one. The sinusoidal red curve identifies a 2α fit.

Moreover, the saturation behavior having a $\sqrt{F}$ functional form is in accordance with the Floquet two-band model for the production of shift currents[77].

From the previous discussion, it is straightforward to distinguish two mechanisms for THz generation in Co_2MnGa. A first mechanism, following a linear increase with thickness and therefore related to bulk carriers, can be associated to a (non-topological) photon-drag effect (see below), and a surface mechanism associated to the topological properties of Co_2MnGa, mainly contributing to the sub-THz spectral region. The superposition of two THz signals, originating from different mechanisms, complicates the interpretation of photocurrent generation experiments. However, polarization-dependent measurements are a useful probe to separately investigate the two mechanisms. Indeed, topological photocurrents are known to be sensitive to the circular polarization of light due to the circular photo-galvanic effect (CPGE)[80,81]. This dependence is explained in terms of an asymmetric depopulation of spin-polarized surface states by optical selection rules, generating a spin-polarized photocurrent.

Fig. 3.8c shows the ratio $(E_{Cpol} - E_{Spol})/E_{Spol}$ for the three films, where E_{Cpol} and E_{Spol} are the THz (peak-to-peak) amplitude originating from the circularly and linearly (S-) polarized 800 nm pump, respectively. The ratio is negative for the 20 and 40 nm films indicating a substantial contribution in the THz emission from the bulk states, as discussed after, and becomes positive in the 80 nm film, where topological surface states provide the major contribution. Fig. 3.8d shows the ratio of the THz spectral amplitude generated by the 80 nm film between the circularly and linearly (S-pol) polarized pump signal. The bulk generation decreases slightly, while the sub-THz one emitted by the surface states improves drastically, further supporting the picture of the two generation mechanisms. The contribution from the CPGE to the THz generation is also confirmed in the 80 nm sample by the peak-to-peak value of the electric field, measured as a function of a quarter wave-plate orientation α, converting the 800 nm pump from a linear to a circular polarization. Fig. 3.8e shows how the THz generation follows a 2α behavior, as expected from a CPGE generation mechanism[80,113,114].

3.3.1 Generation by Photon Drag Effect

As discussed previously, the emission above 1 THz, due to its scaling with thickness, can be associated to the CMG bulk. In this case, due to the cubic lattice structure of CMG and therefore to the corresponding parity conservation, the main THz emission mechanism can be attributed to the photon-drag effect[134–137]. The photon-drag mechanism was already observed in metallic thin films due to an effective transfer of momentum from photons to electrons, thus creating a current along the direction of propagation of light[134,136]. When the light is sent on the film with an angle of incidence different from 0°, the photon-drag current will travel parallel to the material surface and emits P-polarized THz light. This process takes place in CMG, as proved by the following study of the THz emission polarization properties.

The THz signal was probed after being transmitted by a rotating (θ) wire grid polarizer, thus scanning the polarization direction of the beam. The Malus curves for the

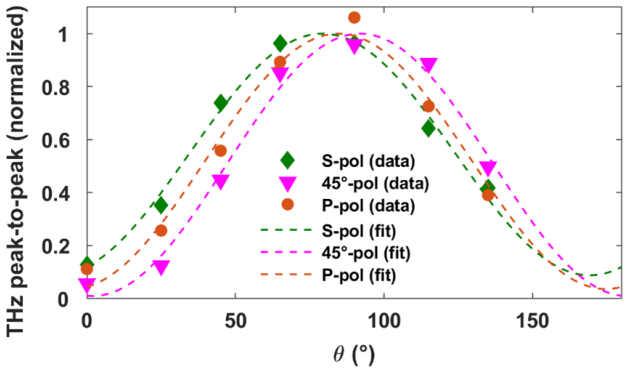

Figure 3.9: Normalized Malus curves of the emitted THz from a Co_2MnGa thin film. The THz signal from the 40 nm film is plotted for three linear polarization orientations of the 800 nm pump. A *S*-polarization means an electric field fully lying on the sample surface.

emitted THz polarization, as obtained by a linearly polarized optical pump, are shown in Fig. 3.9 for the 40 nm thickness. This film hosts the best bulk-over-surface generation efficiency (see Fig. 3.8a). The results highlight the THz polarization to be mainly *P*-oriented ($\theta = 90°$), in accordance with a photon-drag generation mechanism [134–137], where the photocurrents are generated by the transfer of momentum from the photons to the free electrons. A further possibility of a bulk generation induced by a change in carriers direction caused by the Lorentz force [138] has been excluded. In fact, given the in-plane magnetic easy axis, the generation has been found independent from the crystal rotation. Moreover, the THz polarization, being almost independent from the pump linear polarization (see Fig. 3.9), does not support rectification processes, induced by a parity breaking due to the thin film geometry, as the main bulk THz generation mechanism. The minor shifts from the *P*-orientation in Fig. 3.9, observed when the half wave-plate angle is changed, might originate from the reduction in magnitude (with respect to the surface generation) of the photon-drag effect when sending a polarization with components normal to the film surface. However, the polarization dependence is rendered more difficult when also addressing the possibility of a modulation of the shift currents by the linear polarization, as found for the topological semimetals like TaAs [114] and Mg_3Bi_2 [115].

The bulk photon-drag mechanism can also describe the dampening of the electric field magnitude for the 20 and 40 nm films in Fig. 3.8c. This is expected by the well-known surface scattering of electrons: the surface photogalvanic effect (SPGE) [136,139]. During illumination, below the film surface, free electrons are created by the interband transitions and accelerated by the optical electric field, creating positive and negative currents along the polarization direction. Indeed, for *S*-polarized light no net current from the SPGE can be generated (positive and negative currents cancel exactly). However, for *P*-polarized light, due to the presence of surface backscattering, an unbalance current is generated in the direction opposite to the photon-drag current, thus dampening the total photocurrent. Polarization shifts can be observed also by pumping with a circular polarization. Fig. 3.10a,b show the Malus curve for the 40 nm (a) and 80 nm (b) films when pumped by a linear (*S*-polarized) and circular polarization. The shifts measured are plotted as a function of thickness in Fig. 3.10c, highlighting a greater shift coming

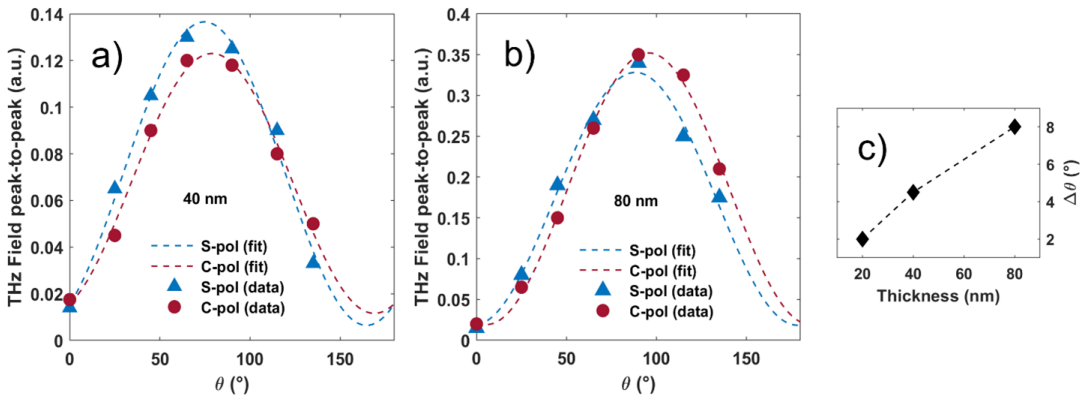

Figure 3.10: Circular polarization dependence of the THz emission from Co2MnGa thin films. a)-b) Malus curves for the THz emitted by the 40 nm and 80 nm films after illumination by a S-polarized (blue) and circular polarized (red) 800 nm pump. **c)** THz polarization orientation shift after illumination by a circularly polarized light.

from the 80 nm sample, as expected by the stronger topological photocurrents.

3.4 Conclusions

The results reported in this chapter highlight the frequency- and time-domain optical spectroscopy of the topological nodal semimetal Co_2MnGa, grown as a thin film over a MgO substrate. The extraction of the broadband optical conductivity for different films of variable thickness reveals how the AC transport features are affected by the film depth, resulting in variable responses both for the intraband and interband excitations. To better understand the charge carriers behavior, temporal-resolved pump-probe and THz emission spectroscopy are used. Indeed, understanding the sub-ps dynamics of topological materials, like CMG, allows the exploration of the interaction between the electronic, lattice and magnetic degrees of freedom in view of their possible applications as electro-optical devices.

The out-of-equilibrium low energy response, studied through optical pump-THz probe measurements, reveals the formation of polaronic quasiparticles with a direct dependence over the pumping wavelength, fluence, and sample thickness. These results suggest a strong coupling between the electrons and the lattice, with a subtle dependence with the thickness in terms of the higher strain effects applied by the substrate to the thinner films. However, applying an external optical pump to the films does not lead only to a change in charge carriers mobility, but also induces the production of photocurrents whose evolution in time cause the emission of THz radiation. The study of the emitted THz from CMG, when pumping at 800 nm, reveals the presence of two microscopic mechanisms of different origin: a photon-drag mechanism of non-topological

nature originating from the bulk of Co_2MnGa and providing a spectral range up to 3 THz, and a surface topological photo-galvanic mechanism mainly responsible for the sub-THz emission. The photon-drag bulk generation mechanism highlights a major difference with respect to other topological semimetals (like TaAs), studied through THz emission spectroscopy[112–114]. There, the THz generation is dominated by the topological features of the bulk due to the breaking of parity symmetry. Instead, in Co_2MnGa, the combination of topological surface states plus bulk THz emission represents the major novelty, suggesting a possible application in terms of tunable THz emitter[114]. Indeed, recently there has been a shift in interest from semiconductors to semimetals for optical THz generation efficiency. While the latter can host well known generation mechanisms like the photo-Dember[140] effect or optical rectification[141], the ones regarding THz generation in semimetals are still partially unknown. Indeed, over semiconductors, semimetals have the advantage of hosting topological quantum phases, allowing the production of tunable ultrafast photo-currents. In this framework, the investigation of the THz emission from Co_2MnGa adds an important piece in the puzzle of THz technological cutting-edge research field.

Chapter 4

Optical Sampling of Dirac States in $MnBi_2Te_4$ Films

The introduction of magnetic elements into a protected topological insulator breaks the time-reversal symmetry and the magnetic interaction can open a gap in the otherwise gapless topological Dirac surface states (DSSs)[23]. This allows various novel topological quantum states to be generated, like the magnetic topological insulators[23,41,82], magnetic Weyl semimetals[83,84] and axion insulators[76]. A plethora of magneto-electric effects is predicted from the topological invariants of these novel materials, like the Quantum anomalous Hall effects (QAHE)[73–75], with the appearance of chiral dissipationless edge channels, half-quantized surface anomalous Hall conductivity[76], nonlinear effects like multiple harmonic generation (MHG)[78,79] and the circular photogalvanic effect (CPGE)[80,81]. The doping with magnetic elements is the usual mean for exploring the interaction between topology and magnetism[42]. However, doping inhomogeneity leads to complex magnetic ordering and small exchange gaps[43]. As a consequence, the various topological quantum effects appear at very low temperatures. Therefore, intrinsic magnetic topological insulators are highly desired for increasing those temperatures and for investigating topological quantum phenomena.

$MnBi_2Te_4$ (MBT) is a novel intrinsic magnetic topological insulator where an additional layer of Mn atoms is inserted in the tetradymite structure of Bi_2Te_4, creating a septuple-layer of atoms with a Te-Bi-Te-Mn-Te-Bi-Te sequence[142,143]. The layers are then stacked through van der Waals (vdW) forces, crystallizing in a rhombohedral layered structure with the space group R-3m, and creating a layered magnet similar to the transition metal halides like CrI_3[144–146]. In MBT, the distance between the Mn layers causes weak magnetic interlayer coupling[147], resulting in an A-type antiferromagnetic ground state with a Néel temperature of $\sim 24\ K$, while preserving a ferromagnetic long range order in the single SLs[148–151]. Therefore, magnetism and topology are structurally separated in MBT, with Mn layers inducing magnetism and the Bi-Te layers generating the topological states. This structural separation makes MBT a case-study for investigating quantum topological phenomena[152,63,107].

The non-trivial topology results in the presence of electronic Dirac Surface States

(DSSs) at the Γ point in the Brillouin Zone (BZ), which have been observed both in single crystal[153,154] and thin films[155] by Angle-Resolved Photoemission Spectroscopy (ARPES). Below the Néel temperature, the time-reversal symmetry is broken by the magnetic ordering, causing the system to enter a magnetic topological phase. In this magnetic phase, the surface Dirac states lose their protection, causing the opening of an energy gap at the Dirac point whose entity, however, is still under debate[107,156].

Although many MBT properties were already measured in single crystals or thin flakes, it is known that topological insulators crystals can be strongly affected by impurities and stoichiometric defects[157]. Therefore, the growth of MBT thin films with well controlled properties may drastically remove defects and impurities plaguing the single crystal properties[157–161]. Indeed, nearly pure DSSs are expected at the Fermi level for thin films[155], differing from the flakes cleaved by single crystals which have shown to host additional electronic contributions from bulk states[153,154]. Moreover, due to the anti-ferromagnetic coupling between the Mn layers, the magnetic properties of the MBT films can be tuned in the thin film geometry by simply changing the number of SLs, with a QAHE and an axion insulator state predicted for an odd and even number of layers, respectively[162].

This chapter reports on the investigation of the electrodynamics of high-quality $MnBi_2Te_4$ thin-films, synthesized at different thicknesses through an evaporation process on a HRFZ-Si(111) substrate.[1] In particular, the optical conductivity of five films with different thickness (7, 12, 20, 30, and 40 SL) are studied through optical spectroscopy across a very broad spectral range, from Terahertz (THz) to Ultraviolet (UV), as a function of both thickness and temperature. The rhombohedral crystal structure of $MnBi_2Te_4$ (R-3m space group) is shown in Fig. 4.1a. Bismuth (Bi) and Tellurium (Te) atoms are bonded to form an ordered structure with a Manganese (Mn) additional layer, forming a septuple layer structure: Te-Bi-Te-Mn-Te-Bi-Te, and granting the intrinsic magnetic properties. The black arrows indicate the a, b and c crystal axes, while the red ones the anti-ferromagnetic coupling between the Mn layers which are stacked and linked through van der Waals forces.

4.1 Determination of the Dirac States Conductivity

Transmission and reflection measurements were taken through a Vertex 70v FTIR broadband interferometer, coupled with different detection systems to scan the spectral range from THz (20 cm^{-1}) to NIR (10000 cm^{-1}). Reflectivity measurements were collected at higher frequency up to the ultraviolet (30000 cm^{-1}) by a JASCO V770 spectrometer. Fig. 4.2a shows the real part of the extracted optical conductivity $\sigma_1(\omega)$

[1] The Si(111) substrates (resistivity 10000 Ohm cm) are cleaned by flashing to 1200 °C in ultra-high vacuum chamber for MBE growth (base pressure 10^{-9} mbar). The treated Si(111) substrates show sharp 7x7 reconstruction patterns from reflection high energy election diffraction (RHEED). High purity Bi (99.9999%), Mn (99.9999%) and Te (99.9999%) are co-evaporated onto the substrates which are kept at a certain temperature of 230℃. The growth is carried out under Te-rich condition, and the flux ratio between Mn and Bi is kept nominally 1:2. The growth rate is 1 SL/7 min. Post-annealing at 250 °C is carried out to improve the crystalline quality[87].

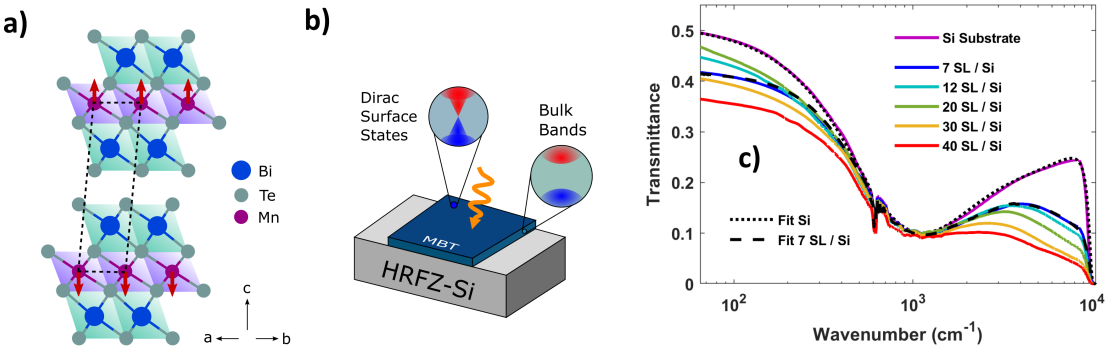

Figure 4.1: Optical spectroscopy of MBT thin films. a) View of the crystal structure of $MnBi_2Te_4$. The Bi, Te and Mn atoms are bonded to form a septuple layer structure, with an anti-ferromagnetic exchange between the Mn layers. The arrows indicate the crystal axes. The dotted lines highlight the unit cell. **b)** Schematic description of the thin film samples over a HRFZ-Si(111) substrate. The two surfaces are expected to host Dirac states due to the non-trivial topology of the bulk gapped bands. **c)** Experimental transmittance of MBT films over a silicon substrate. The black curves correspond to a Drude-Lorentz fitting (see main text), on the transmittance of the bare Si substrate (black points) and on the 7 SL film (black dashed line).

of MBT films with different thicknesses, across the whole measured spectrum. $\sigma_1(\omega)$ is obtained through a Kramers-Kronig constrained simultaneous fitting of reflectance and transmittance data, described through a multi-layer model using the RefFIT software[118]. Examples of the transmittance fit are shown as black lines in Fig. 4.1c. The measured HRFZ-Si(111) optical parameters are used as inputs in the RefFIT procedure. The optical conductivity for all thicknesses is dominated by a broad absorption band located between 15000 and 20000 cm^{-1} which can be associated to bulk interband transitions in good agreement with data for single crystals[164]. This broad peak is well separated from a low-energy metallic contribution appearing for all films below 1000 cm^{-1} (see Fig. 4.2b).

An estimation of the electronic gap E_g can be obtained by taking the zero crossing of a linear fitting curve for the interband conductivity onset. This fitting is plotted for all films in the inset of Fig. 4.2a through dashed black lines. Their intersections with the frequency axis provide an estimation for the energy gap. E_g is of the order of 5000 cm^{-1} (0.62 eV) for the three (20, 30 and 40 SL) thicker films. The gap is subjected to a red shift with decreasing thickness, reaching nearly 3000 cm^{-1}(0.37 eV) in the 7 SL film. Although the gap values estimated from our optical measurements are higher than the absorption edge obtained from bulk MBT[148,163,153,164] (nearly 200 meV), they are in good agreement with ARPES studies on the same films[155]. Moreover, near 2500 cm^{-1} (0.3 eV), an additional absorption feature appears for the 7 and 12 SLs films at variance with the thicker films, hosting instead a smooth decreasing behavior. Given its energy range, this extra peak could be associated to transitions from the lower energy Dirac

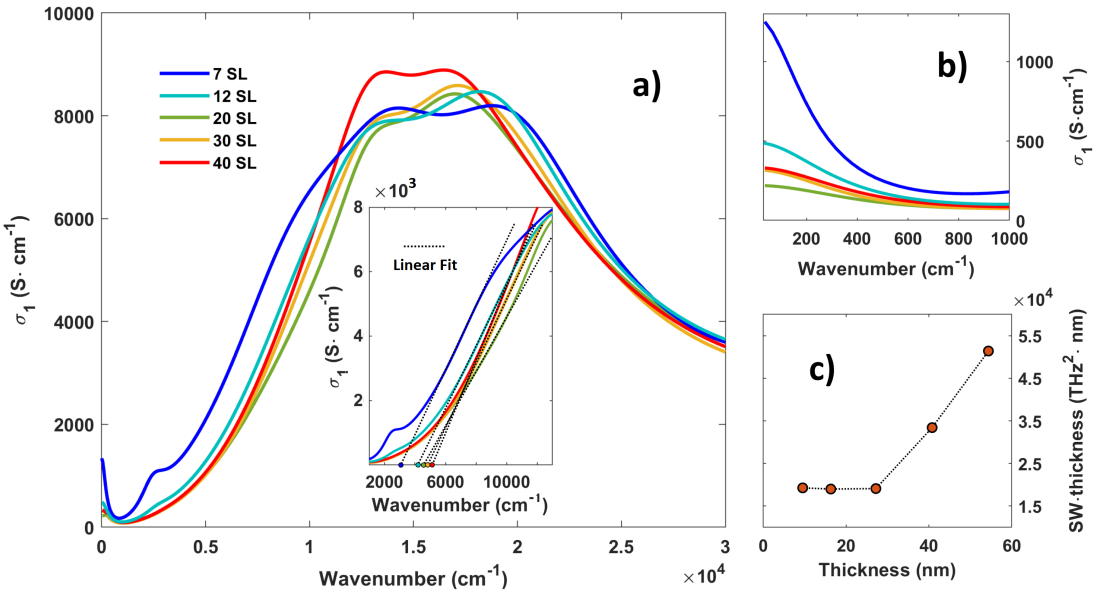

Figure 4.2: Room temperature optical conductivity at different thicknesses for MBT thin films. a) Optical conductivity of MBT films from THz to UV, as extracted for each thickness by the reflectance and transmittance measurements. The inset shows the fit of the MBT films bulk transitions. An electronic gap $E_g \sim 5000$ cm^{-1} (0.62 eV) is extracted for the three thicker samples. E_g instead softens to 3000 cm^{-1} (0.37 eV) in the 7 SL film. **b**) THz conductivity for the five films with different thicknesses. **c**) Drude spectral weight (SW) times the thickness (SW·thickness) as a function of thickness. The free carriers response of MBT shows a monotonic linear decreasing behavior with thickness, reaching a plateau below 25 nm due to the presence of DSSs.

cone to the upper one, in analogy to the Pauli blocking transitions in graphene.

Fig. 4.2b shows the real part of the optical conductivity in the terahertz spectral range, highlighting the metallic absorption edge coming from the low energy states. Strong thickness dependent changes can be observed, with the thinner 7 SL sample hosting a conductivity almost 4 times higher than the 40 SL film. To highlight the contribution of the surface states to the low-energy electrodynamics of MBT, the low-energy optical conductivity is fitted with a Drude term characterized by a a scattering rate Γ and a spectral weight $SW = {\omega_p}^2/8$, where ω_p is the plasma frequency. To understand the surface contributions to the Drude response, the spectral weight is multiplied by the thickness d of films. This result is plotted in Fig. 4.2c as a function of d. Here, the metallic contribution is nearly constant for the 7, 12 and 20 SL films, and grows roughly in a linear way at larger thicknesses. The nearly constant value of $SW \times d$ for films between 7 and 20 SLs suggests that in those films the free-charge contribution mainly comes from Dirac surface states. This result also supports a surface-related

origin for the E_g red shift and the increase in strength of the oscillator near 2500 cm^{-1} (see Fig. 4.2a), both found in the thinner films where the topological surface states are expected to contribute strongly to the optical conductivity.

For the 7 SL film, it is possible to estimate a surface DC conductance value of $\sim 1.3 \times 10^{-3}$ S, nearly 17 times the quantum conductance $G_0 = 2e^2/h \simeq 7.75 \times 10^{-5}$ S. This result can be compared with materials like graphene, hosting a conductance of $\sim 2 \times 10^{-3}$ S[165,166], and Bi_2Se_3, with a conductance of $\sim 1.1 \times 10^{-3}$ S[167]. Supposing the conductivity of the 7 SL film fully originates from the 2D surface states, it is possible to link its Drude spectral weight to the density of carriers n_{2D} as[168]

$$\omega_p^2 d = \frac{n_{2D} e^2}{m^* \epsilon_0} \tag{4.1}$$

where m^* is the mass for the Dirac fermions of the surface states, obtained as the ratio of the Fermi momentum k_F and velocity ν_F: $m^* = \hbar k_F / \nu_F$. Considering the surface state dispersion as purely linear near the Fermi level[155], the right part of Eq. 4.1 can be written as[168]

$$\omega_p^2 d = \frac{G_0}{\hbar} \frac{E_F}{\epsilon_0} \tag{4.2}$$

where G_0 is the quantum of conductance ($G_0 = 2e^2/h \simeq 7.75 \times 10^{-5}$ S) and $E_F = \hbar k_F \nu_F$ is the Fermi energy. From the Drude fitting we can thus determine $E_F \sim 120\ meV$ and, using the constant Fermi velocity $\nu_F = v_F = 5.5 \times 10^5$ m/s extracted by ARPES measurements[155], a Fermi wavevector $k_F \sim 0.04$ $Å^{-1}$ is estimated, which can be compared to the result $k_F \sim 0.07$ $Å^{-1}$ obtained by ARPES[155].

4.2 Temperature Evolution of the Dirac Carriers

The spectroscopy set-up for the measurements at low temperatures is based on the Michelson interferometer discussed in section §2.3. As shown in the previous section, the optical conductivity of the 7 SLs thin film is dominated by Dirac surface states. Therefore, its optical behavior is investigate as a function of temperature to study the effect of the magnetic order and then of the time-reversal breaking on the Dirac surface states. In this regards, optical transmittance measurements weren performed between 20 and 10000 cm^{-1} from 300 K to 5 K, crossing the Néel temperature at about 24 K. The real part of the optical conductivity is shown in Fig. 4.3a, as extracted from transmittance measurements through the RefFit program.

As evident from the Figure, the optical conductivity from 300 to 50 K (above the Néel temperature) is nearly constant, showing a Drude term (associated to mobile Dirac surface states) below 1000 cm^{-1}, an absorption band in the Mid-Infrared (MIR) around 2500 cm^{-1} (310 meV) and, at higher frequency, the absorption tail related to interband bulk transitions, whose linear extrapolation to the frequency axis provides an electronic gap of about 3000 cm^{-1} (see above). The inset in Fig. 4.3a schematically describes these electronic transitions. Below $T_N \simeq 24$ K, the optical conductivity decreases in the whole spectral range with respect to all other temperatures. More specifically, the electronic

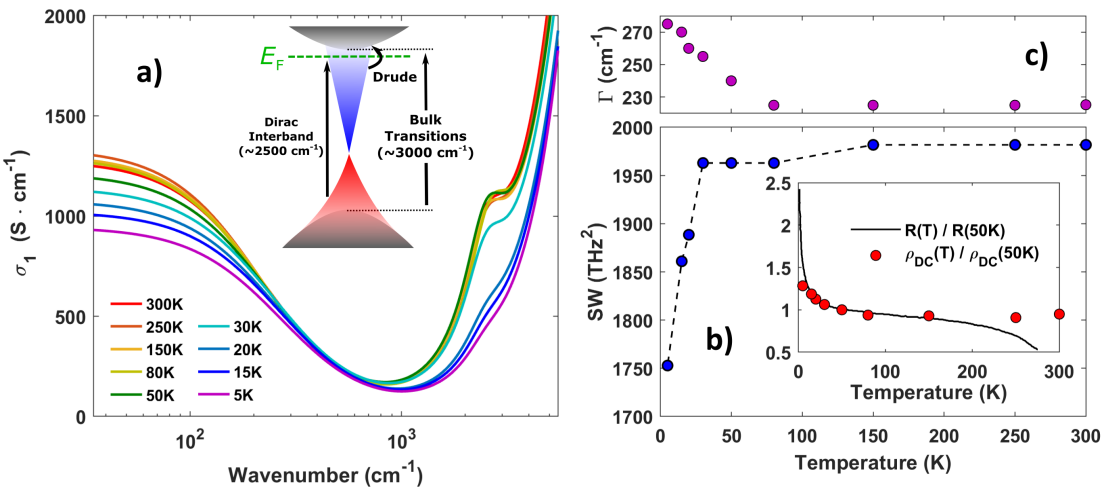

Figure 4.3: Temperature dependence of the optical conductivity for the 7 SL MBT film. a) Real optical conductivity at different temperatures. The inset shows the electronic transitions accounting for the optical conductivity features. **b)** Drude spectral weight (SW) as a function of temperature. The inset shows the ratio of the SW at different temperatures with respect the one at 50 K over the same ratio for the film resistance. **c)** Temperature dependence of the Drude scattering rate.

gap hardens to about 4000 cm^{-1}, the Drude term is reduced in intensity, and the MIR absorption band nearly disappears. This is at variance with single crystal measurements, where an increase of the optical conductivity with decreasing temperature is observed, as given by the reduced scattering of the bulk electrons [148,164].

The effect of magnetism on the topological surface states can be quantified by plotting the Drude spectral weight SW as a function of temperature (see Fig. 4.3b). Here, the SW is approximately constant above 30 K, while decreasing rapidly without disappearing down to 5 K, *i.e.*, well below the Néel temperature. The optical conductivity measurements well reproduce the DC behavior of the resistance R on a film of the same batch, as shown in the inset of Fig. 4.3b. Here the ratio $R(T)/R(50K)$ vs. T (black line) is compared to the zero-frequency extrapolation of the optical resistivity ($\rho_{DC} = 1/\sigma_1(\omega = 0)$) normalized at 50 K ($\rho_{DC}(T)/\rho_{DC}(50K)$). Besides some discrepancies observed around room temperature (probably caused by an extra temperature dependence of the silicon substrate), the two ratios behave in a very similar way, with a slow rise below 50 K induced by the scattering rate change (see Fig. 4.3c) and a sharper one below the Néel temperature linked to the reduction of the Drude spectral weight as induced by the breaking of the time-reversal symmetry. Indeed, broken time-reversal symmetry is expected to remove the topological protection of DSSs [41], inducing the formation of a gap at the Dirac node. In this framework, the gap opening modifies the linear (Dirac) energy-momentum dispersion which, in the magnetic phase, should become $E(k) = \pm\sqrt{\hbar^2 v_F^2 k^2 + \Delta^2}$, where 2Δ is the gap value [41]. Since in MBT the Dirac

node is located well below the Fermi level ($\simeq -0.12$ eV), the gap opening should only partially affect the electronic transitions near the Fermi level like the Drude term, whose spectral weight gets dampened due to the modified energy-momentum dispersion. In other terms, the gap opening corresponds for the Dirac quasiparticles to acquire an effective mass, thus decreasing their mobility and conductivity contribution. An estimate of the gap value can be achieved from the Drude SW reduction below T_N, using again Eq. 4.1, from which it is possible to link the ratio between the SW of the film at two different temperatures, T_1 and T_2, with the change of the effective mass m^* and the 2D surface electron density n_{2D} as follows

$$\frac{SW_{T_1}}{SW_{T_2}} = \frac{m^*_{T_2}}{m^*_{T_1}} \frac{n_{2D,T_1}}{n_{2D,T_2}} \tag{4.3}$$

To understand the effect of the magnetic phase transition on the spectral weight, the experimental temperatures $T_1 = T_> > T_N$ and $T_2 = T_< < T_N$ are chosen, respectively above and below the Néel temperature T_N. The 2D electron density for a single surface takes the form $n_{2D} = k_F^2/4\pi$[168], while the effective mass is $m^* = \hbar k_F/\nu_F$, where $\nu_F = (1/\hbar)\partial E_F/\partial k_F$ is the Fermi velocity. By using the gapped energy-momentum dispersion $E_F = \sqrt{(\hbar v_F k_F)^2 + \Delta^2}$ for $T_<$, where 2Δ is the gap[41], Eq. 4.3 can be written as

$$\frac{SW_{T_>}}{SW_{T_<}} = \sqrt{\frac{E_F^2 + \Delta^2}{E_F^2 - \Delta^2}} \tag{4.4}$$

that describes a reduction of the Drude spectral weigth in the magnetic ordered state, quantified by the gap value. Using the experimental data, i.e., $T_< = 5\ K$, $T_> = 50\ K$, and E_F as obtained by Eq. 4.2 (the Fermi energy is approximately constant across the transition), a gap value $2\Delta \simeq 80\ meV$ is obtained. This result is at variance with recent high-resolution ARPES data on single crystals[153], highlighting an unperturbed Dirac node even below T_N. However, they are in good agreement with recent ARPES results obtained on MBT thin films grown via MBE[169], which propose a large energy gap (> 70 meV) below the Néel temperature for a 5 SL film on silicon. This result confirms the importance of thin films geometry in highlighting the magnetic gap opening and as a platform where topological surface states, overcoming bulk contribution, can be used for device applications. Moreover, our results are in good agreement with theoretical calculations[107] and point contact tunneling spectroscopy results[170]. These propose a magnetic gap of about 50-60 meV ($\sim 400 - 500$ cm^{-1}), slightly lower than the value extracted in this work, $2\Delta \simeq 80\ meV$. Therefore, the evidence of a gap opening below T_N, along with the dominant surface states behavior at the Fermi level, highlight the intrinsic topological character of MBT thin films, in stark contrast with single crystal and thin flakes.

4.3 Conclusions

In this chapter, the optical properties in a broad spectral range, from Terahertz to UV, of the intrinsic magnetic topological $MnBi_2Te_4$ material are reported. High quality

MBT thin films were studied at room temperature with different thickness, from 7 to 40 septuple-layers, allowing the separation between the contribution of Dirac surface free-electron states in the optical conductivity from bulk electronic transitions. In the 7 SLs (where the Dirac surface states provide the major contribution to the low-energy conductivity), the behavior of these states is studied by crossing the Néel critical temperature at nearly 24 K and entering the magnetically time-reversal broken state. The temperature-dependent optical conductivity measurements indicate the opening of a gap at the Dirac node, as induced by the broken time-reversal symmetry, in stark contrast to ARPES measurements in both single crystals and thin flakes, where contradictory results have been obtained. From the reduction of the Drude spectral weight below T_N, a gap of the order of 80 meV can be estimated, in good agreement with calculation and tunneling measurements. This optical study indicates that an intrinsic topological behavior is observed in $MnBi_2Te_4$ thin films, opening the road for exploring the interaction between magnetism and topology and the appearance of novel electrodynamics effects[155,171,172,163].

Chapter 5

Spectroscopy of the Layered Ferromagnet CrI_3

The spin liquid phase introduced in section 1.4 and, in particular, the Kitaev honeycomb model, can be used to describe the newly found physical processes that take place in materials like the Mott-Hubbard insulator α-$RuCl_3$. Here, experimental results reveal the presence of fractionalized charges, as suggested by a broad continuum resonance observed through optical means (Raman[173] and THz-TDS[174,175]). This continuum cannot be explained in terms of conventional two-magnon scattering or structural disorder, but rather by the Kitaev model predictions. The excitation appears to persist up to 100 K and even below the magnetic ordering temperature (14 K). These results brought additional interest to the already fascinating research of vdW layered ferromagnets, in particular to compounds like CrI_3 and VI_3 that are isostructural to α-$RuCl_3$, thus are candidates to host the spin liquid phase.

Apart from the spin liquid candidate role, three-dimensional (3D) layered van der Waals (vdW) crystals[176–178] are systems preserving the 2-Dimensional (2D) phenomenology while guaranteeing significant advantages over their applications in 3D bulk devices[179–181]. Their emerging functional properties are associated with non conventional electronic behaviors like excitonic interactions and dynamics[182] and spin/valley physics[183,184]. These exotic electronic properties combined with intrinsic ferromagnetic order have been found in vdW transition metal halides like CrI_3 and $CrCl_3$[144,185–189]. Here, ferromagnetism may sustain novel phases of matter, like the Quantum anomalous Hall Effect (QAH)[41,74] or the spin liquid state already mentioned[11,190], opening numerous opportunities for magneto-optical applications[191–193]. Moreover, bulk layered vdW magnets can be exploited as substrates, interfacial layers and tunnel barriers for engineering magnetic proximity effects[194,195] and designing novel spintronic applications[196,197].

Chromium trihalide CrI_3 has been shown to be a cleavable magnetic material with a great tunability of its magnetic properties with thickness[85,198,199]. Bulk CrI_3 is a layered c-axis anisotropic ferromagnetic insulator with a Curie temperature of 61 K and a rhombohedral layer stacking below $\sim$220 K, where a first order structural phase transition converts the unit cell from a monoclinic room temperature phase[200].

In each layer, the Cr atoms form a honeycomb structure (Fig. 5.1a), with each of them surrounded by six Iodine atoms in an octahedral coordination[85]. Remarkably, few-layer CrI_3 has been proved to host anti-ferromagnetic order between the layers, with a Néel critical temperature of 45 K and a monoclinic stacking[198]. CrI_3 has been theoretically predicted[201,202] to host strong interactions among electronic, phononic and magnetic degrees of freedom, including a strong spin-orbit coupling (SOC)[203–205], with the appearance of exotic responses like nonreciprocal magneto-electric effects[206,207,197]. As a result, CrI_3 is a candidate material to host subtle, low energy, emergent phases of matter[20,21]. Indeed, recent results[208,173,209] have proved how an isostructural compound like α-$RuCl_3$ is able to host low energy fractionalized excitations reminiscent of a Kitaev spin liquid phase. Moreover, neutron magnetic scattering measurements on CrI_3[210] have suggested the presence of topological magnon dispersions[211], with the appearance of magnon edge states, analogous to topological insulators for electronic systems. Additional studies on the magnetic order revealed how the breaking of the spin-rotation invariance may be caused by large SOC, rather than the crystal field anisotropy[204]. All these results lead to a very complex picture of all degrees of freedom interactions in CrI_3.

Although theoretical and experimental data suggest CrI_3 to be a candidate material for hosting subtle emergent phases of matter, its bulk electronic and vibrational properties have never been investigated. The results reported in this chapter address this gap, by investigating the optical properties of a bulk CrI_3 single crystal in its whole phase diagram covering both the paramagnetic and ferromagnetic phases. CrI_3 single crystals were synthesized by a chemical vapor transport technique[1]. The crystal structure of CrI_3 is shown in Fig. 5.1a. The Chromium (Cr) and Iodine (I) atoms are bonded to form honeycomb ordered layers. The arrows indicate the a, b and c crystal axes. The bulk crystal structure of CrI_3 at room temperature is described by a monoclinic (space group C2/m) unit cell. Below the structural phase transition at $T_{struc} \sim 220$ K, this changes to a rhombohedral symmetry (space group $R\bar{3}$)[200].

Reflectance (R) and Transmittance (T) measurements were performed in a broad spectral range from THz (20 cm^{-1}) to NIR (15000 cm^{-1}) ($\sim$ 2.5 meV – 1.86 eV) and temperatures from 5 to 300 K. The spectroscopy set-up is based on the Michelson interferometer discussed in the previous chapter. Fig. 5.1b reports the room temperature R and T of a CrI_3 single crystal with a 300 μm thickness. Fig. 5.1c shows the real part of the refraction index, while Fig. 5.1d the corresponding absorption coefficient, both extracted through the RefFit Kramers-Kronig consistent fitting process[118]. The reflectance spectrum is dominated by a strong phonon absorption near 230 cm^{-1}, which can be associated to the in-plane E_u collective oscillations of Cr atoms[201] (see Fig. 5.1e). In the far-infrared transmittance, it is possible to resolve additional low energy absorption peaks, extending to nearly 400 cm^{-1}. Above 400 cm^{-1}, a flat transmittance (absorbance) is observed, extending up to the crystal-field electronic gap that can be

[1] A 1 g mixture of the stoichiometric ratio of Cr metal and I_2 pieces (Alfa Aesar, 99.99%) was packed in a sealed evacuated quartz glass tube (22 cm long and 16 mm wide) and heated in a three zone furnace, set at zone temperatures 650, 550, and 600 °C, for one week. The "charge" was placed in the 650 °C zone. Many CrI_3 crystals were formed in the 550 °C zone. The crystals are stable in air for a few hours.

observed both in transmittance and reflectance at room-T around 9200 cm^{-1} (1.14 eV). The transmittance minima (broad weak maxima in the absorption coefficient, Fig. 5.1d), appearing on the IR plateau at about 1600 and 3600 cm^{-1}, are instead associated to the bending and stretching vibrations of few intercalated water molecules among the CrI_3 layers[212]. Indeed, layered systems are common hosting materials for various intercalant species, ranging from small ions to atoms and molecules[213].

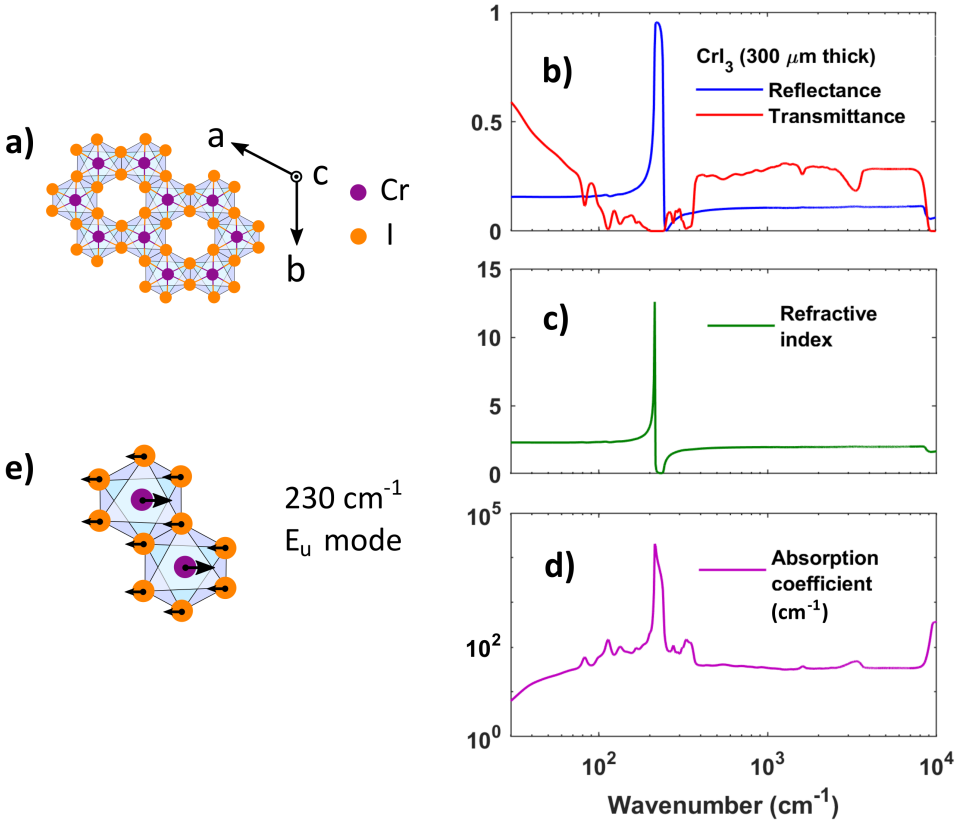

Figure 5.1: Infrared spectroscopy measurements of a CrI_3 single crystal. a) Top view of the crystal structure of CrI_3. The Cr and I atoms are bonded to form honeycomb ordered layers. The arrows indicate the crystal axes. **b)** Optical reflectance and transmittance of a 300 μm thick CrI_3 crystal at 300 K. The reflectance is dominated by a single phonon mode at 230 cm^{-1}. The measured transmittance highlights instead a plethora of far infrared vibrational modes and a band-gap around 9200 cm^{-1}. **c)** Real part of the refractive index of CrI_3 at 300 K. **d**) Absorption coefficient at 300 K of CrI_3. **e** In-plane phonon mode of the Cr atoms, associated to the strong vibrational mode at 230 cm^{-1} in the bulk CrI_3.

5.1 Temperature dependence of the electronic gap

The temperature dependent transmittance measurements in the NIR spectral region are highlighted in Fig. 5.2a. Here, a huge blue shift (nearly 2000 cm^{-1}) of the electronic gap E_g can be observed with decreasing temperature from 300 K to 5 K. E_g(T) values are extracted by a linear fitting of the decreasing transmittance through its intercept with the frequency axis[214]. E_g(T) as a function of temperature is reported in Fig. 5.2b. In this Figure, both the ferromagnetic Curie temperature T_c and the structural transition temperature T_{struc} have been indicated by vertical dotted lines. While across the structural transition the electronic gap presents a smooth behavior, at the paramagnetic/ferromagnetic transition a discontinuity appears with a robust increase in the gap value below T_c. Both the lattice expansion and the electron-phonon interaction may induce a temperature dependence of the electronic gap[215,216]. Both terms can be modeled through the Manoogian and Leclerc empirical equation[215,217]

$$E_g(T) = E_g(T=0) + UT^s - V\epsilon\,(\coth(\epsilon/2k_BT) - 1) \tag{5.1}$$

where U, s, V and ϵ are temperature independent coefficients. U and V are the coupling constants weighting the lattice expansion and electron-phonon interaction contributions, respectively, while ϵ is an energy averaging all the acoustic and optical phonons. E_g data in Fig. 5.2b for the paramagnetic phase have been fitted through Eq. 5.1. The result is shown in Fig. 5.2b through a dashed purple line. Fitting coefficients in Eq. 5.1 are presented in Table 5.1, compared to other semiconductors from literature. The lattice expansion, parametrized by U, has been found to give a negligible contribution to the temperature dependence of E_g. The strongest effect is thus given by the electron-phonon interaction, whose intensity is measured by the coefficient V, higher than the one found in most of the known semiconductors (see Table 5.1). The further blue shift of the electronic band gap below the Curie temperature suggests a further dependence of the electronic gap from the magnetic degrees of freedom.

To quantify this discontinuity, an extra gap-value $\Delta E_g(T)$ can be defined as the difference between the actual gap value $E_g(T)$ and that corresponding to the paramagnetic extrapolation below T_c, $\Delta E_g(T) = E_g(T) - E_{fit}(T)$. $E_{fit}(T)$ is determined by using the Eq. 5.1 fitting process (see Fig. 5.2b). At 5 K (the minimum temperature we reach in our optical measurements), $\Delta E_g(T) = 35\ meV$. This value cannot be related to a modification of the electron-phonon interaction, since the phonon spectrum is unaltered across the transition (see Fig. 5.3c). From the theoretical point of view, a recent work[201] calculates the electronic structure of CrI_3 monolayers both in the magnetic and non-magnetic phase. This paper suggests that the electronic band structure is strongly perturbed by the magnetic state and depends on the magnetization (M) easy axis direction. In particular, the electronic gap is larger when M is along the c-axis than in the ab plane of the CrI_3 structure. This result, calculated for CrI_3 monolayer, seems to be valid also for bulk CrI_3 bulk[201]. In this framework, magnetic measurements[218] show that magnetization, in bulk single crystal, develops along the c-axis. In order to establish a correlation between optical and magnetic data, in the inset of Fig. 5.2b

we show $\Delta E_g(T)$ normalized to $\Delta E_g(T = 5)$. In the same inset, we also plot the magnetic moment along the c-axis[218] normalized to its lowest T (5 K), $M(T)/M(5)$. As evident from the figure, both quantities follow a very similar trend, suggesting that the extra gap value is related to the development of the magnetic state. These results highlight a complex degrees of freedom interplay in CrI_3, suggesting that the electronic gap hardening might be related to a non-trivial coupling between the electrons and the magnetic order[197,199,205].

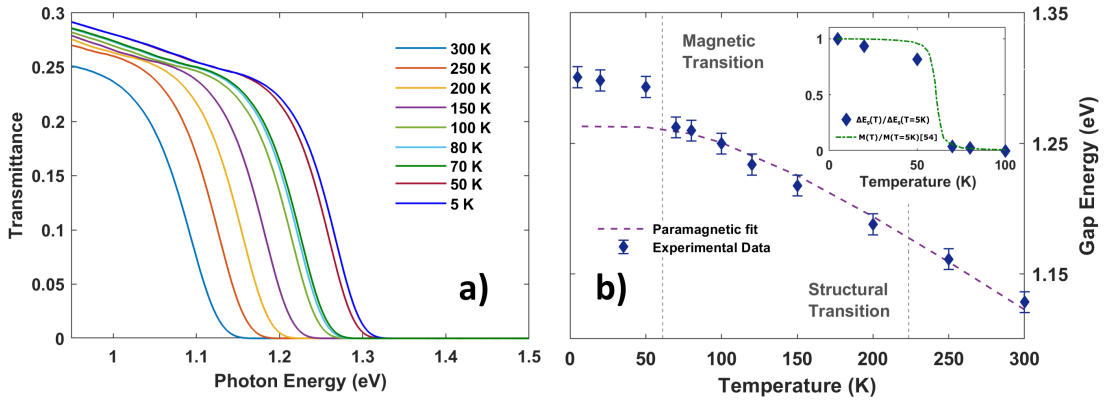

Figure 5.2: Electronic band gap variation with temperature of CrI_3. a) Measured NIR transmittance for a 300 μm CrI_3 slab at various temperatures. A strong red shift towards higher temperatures is visible. **b)** Optical band-gap as a function of temperature. The dotted lines highlight the magnetic and structural transition temperatures. The paramagnetic phase is fitted through the model in Eq. 5.1. Inset: comparison of the extra-gap values $\Delta E_g(T)$ (normalized to $\Delta E_g(5K)$, see text) and the magnetization order parameter $M(T)$ normalized at the lowest temperature[218].

5.2 Far infrared response

The far-IR transmittance (T) and reflectance (R) at different temperatures are shown in Fig. 5.3a,b. The reflectance spectrum is limited to the strong phonon absorption dominating the response. Fig. 5.3c shows the absorption coefficient as extracted through the RefFit Kramers-Kronig consistent fitting process of R and T[118], using a combination of Lorentzian functions to reproduce the complex dielectric function

$$\epsilon(\omega) = \epsilon_\infty + \sum_j \frac{\nu_{pj}^2}{(\nu_{0j}^2 - \nu^2) - i\gamma_j \nu} \tag{5.2}$$

where ν is the frequency, ν_{0j} is the central frequency of the j-th excitation, γ_j is the damping factor or line-width and ν_{pj} is the amplitude. The spectra are composed by several peaks located between 70 and 360 cm^{-1} and we observe an overall decrease of the

	$E_g(0)$ (eV)	ϵ (meV)	V
CrI_3 (paramagnetic)	1.26	26	4.68
$CuGaS_2$ [219]	2.5	38	1.53
$CdGeP_2$ [217]	1.89	-	3.2
$CdGeAs_2$ [217]	0.595	-	1.27
$ZnSnSb_2$ [217]	0.66	-	3.74
Ge [216]	0.74	-	2.77
Si [216]	1.17	-	2.74
GaAs [216]	1.52	-	3.14

Table 5.1: Coefficients for the band gap frequency shift of semiconductors as a function of temperature, as obtained by the model of Eq. 5.1. The symbol "-" highlights missing values from literature.

absorption by reducing T. Due to the van der Waals nature of the CrI_3 crystal and the in-plane polarization of the incident radiation in this experiment, a single layer model for the lattice vibrations is expected to describe the experimental phonon absorption peaks. Indeed, CrI_3 layers can be described by the D_{3d} point group symmetry [201,220], which predicts five IR-allowed transitions, namely three E_u modes and two A_{2u} modes, three inactive modes (one A_{1u} and two A_{2g}), and six Raman-active modes (two A_{1g} and four E_g). Raman spectra have already been measured in previous works [189,221–226], revealing the presence of magnons and a plethora of magneto-optical effect. The corresponding Raman peaks at room-T are reported in Table 5.2, together with numerical calculations (at 0 K) [227,228,221] and the IR absorption peaks observed at room-T in our experiment, as measured by absorption peak maxima. In the theoretical calculation, the heavier iodine atoms are predicted to dominate the phonon spectrum below 150 cm^{-1} [201,229], therefore being related to the strong absorption peaks at 82 and 114 cm^{-1} (E_u modes) and 133 cm^{-1} (A_{2u} mode). At higher energies, above the strong absorption at 230 cm^{-1} (E_u symmetry, mainly due to Cr vibrations), a series of peaks can be seen in Fig. 5.3c, with a strong spectral weight from 300 to 360 cm^{-1}. These higher frequency excitations are not predicted by the ab-initio calculations for CrI_3 [201,229,227]. However, their frequencies can be captured by a linear combination of Raman and IR fundamental modes as reported in Table 5.2, suggesting an important role of anharmonicity in the phonon spectrum of CrI_3.

Further differences from the D_{3d} point group symmetry predictions can be found in the presence of extra absorption shoulders at nearly 100, 150, 170 cm^{-1} and near the strong E_u peak at 230 cm^{-1}. The presence of these excitations has been investigated in recent DFT calculations of monolayer CrI_3 [229], showing their dependence from the magnetic ordering. Indeed, their temperature dependence (they nearly disappear below T_c) is not trivial. A similar result is obtained for the A_{2u} predicted in-plane phonon at 133 cm^{-1} (as measured at $T = 300\ K$), which seems to disappear at low temperatures.

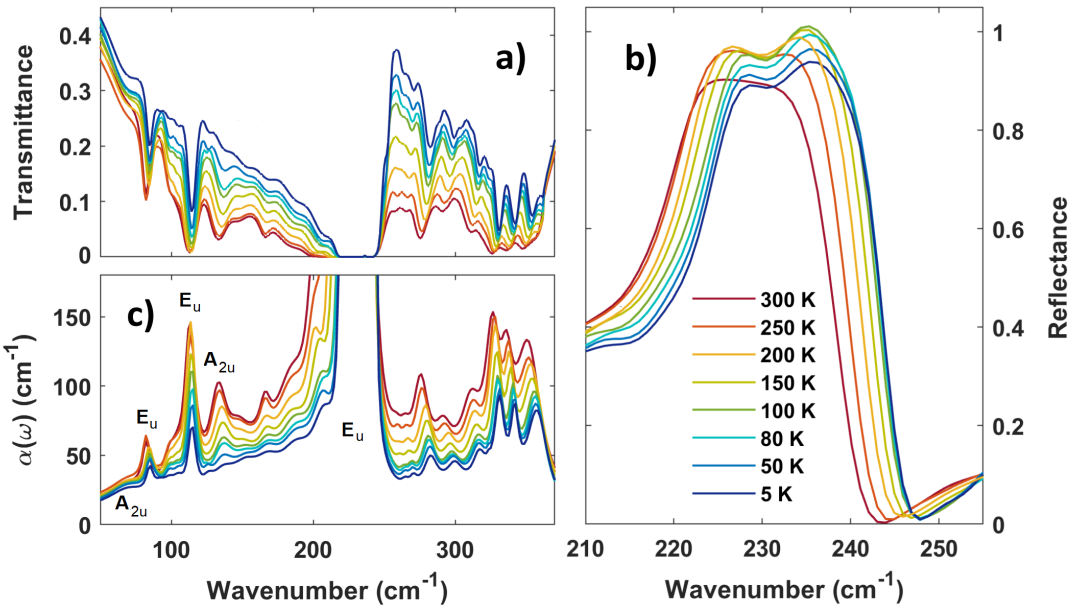

Figure 5.3: Far infrared spectroscopy of a CrI_3 single crystal. **a)** Optical transmittance at different temperatures for a 300 μm thick CrI_3 single crystal. **b)** Optical reflectance window of a 300 μm thick CrI_3 at 300 K. The reflectance is dominated by two phonon modes near 230 cm^{-1}. **c)** Absorption coefficient at various temperatures as extracted from the transmittance measurements fitting process. A general transparency is observed with decreasing temperatures, along with the disappearance of three modes at very low temperatures. The text highlights the main vibrational modes predicted in accordance with the D_{3d} point group symmetry.

These results have been explained in terms of a strong spin-phonon coupling[229], which predicts the appearance of a gap in the phonon density of states between the two E_u modes at 113 and 230 cm^{-1}.

The low-energy (THz) side of the absorption coefficient suggests the presence of a broad background. Its general shape and temperature dependence can be obtained by a best fitting process of the absorption coefficient at various temperatures, taking into account the phonon peaks previously discussed (see the inset of Fig. 5.4 for an example of fitting at 300 K). An absorption background has been observed in the THz range in α-$RuCl_3$[175,230]. Although strongly debated, this background has been mainly associated to Kitaev spin liquid excitations. In CrI_3, at variance with α-$RuCl_3$, this broad absorption, centered around 70 cm^{-1}, is already present at room-T and decreases with reducing T, nearly saturating below T_c (see Fig. 5.4). The broad temperature-dependent THz background could have electronic, lattice, or magnetic origins. Bulk CrI_3 is a very good electric insulator with an electronic gap around 1.2 eV. This implies that we do not expect thermally-induced free electrons in the material (in particular at low-T), which

Raman-active	IR-active	IR-active (two-phonons)
52 [50.1] (E_g)	60 [56.8] (A_{2u})	276 ($230E_u + 52E_g$)
79 [76.1] (A_{1g})	82 [80.3] (E_u)	291 ($230E_g + 60A_{2u}$)
99 [101.8] (E_g)	113 [114.3] (E_u)	310 ($230E_u + 79A_{1g}$)
105 [107.5] (E_g)	133 [133.3] (A_{2u})	326 ($230E_u + 99E_g$)
128 [129] (A_{1g})	230 [225.3] (E_u)	337 ($230E_u + 105E_g$)
230 [241.1] (E_g)		347 ($230E_g + 113E_u$)

Table 5.2: CrI_3 vibrational modes frequencies (in cm^{-1}) at 300 K. The values in the quadratic brackets highlight the in-plane Raman- and IR-active modes at 0 K, as obtained by DFT results[201]. The first column shows the experimental Raman modes[228,221]. The IR-active experimental modes obtained in this work are shown in the second and third columns.

can affect the absorption in the THz range. This excludes an electronic origin of the THz background. In $RuCl_3$ Kitaev-like material, where many theoretical calculations exist for the 3D magnetism, a similar background (of magnetic origin) increases with decreasing T. In CrI_3, instead, it is a decreasing function of T, nearly reaching an intensity saturation at T_c. Moreover, it is located around 10 meV, an energy larger than the exchange magnetic energy in CrI_3 ($J \sim 3\ meV$)[204]. This difference, associated to the decreasing T-dependence, suggests a non-magnetic origin. The last mechanism, i.e., acoustic phonon assisted absorption, has been proposed some years ago to explain some extra absorption in the THz and sub-THz regions in alkali-halides[231,232]. The extra absorption corresponds to processes in which optical modes are excited by photons concomitantly with the absorption of acoustic modes at high wavevectors. Due to the quasi-continuum distribution of acoustic modes, one expects a broad absorption band, which depend on T due to the modes T-dependence. In conclusion, the characteristic background energy (nearly 10 meV) and its temperature dependence seem to rule out both a magnetic and electronic origins, suggesting instead an acoustic assisted mechanism at the main contributor.

5.3 Anharmonic properties of the optical phonons

Due to the correlations found in CrI_3, and the possibility to exploit them for nanoscale electro-optical, spintronic and caloritronic applications, a study of the lattice anharmonic properties and energy relaxation is also required. Indeed, the electron-phonon (e-ph) and phonon-phonon (ph-ph) interactions play a key role in the electrical transport. The interaction of electrons with vibrational modes (e-ph) is proportional to the number of phonons, which is determined by the balance between their generation and their thermalization times[233]. When the ph-ph interactions are not efficient enough to

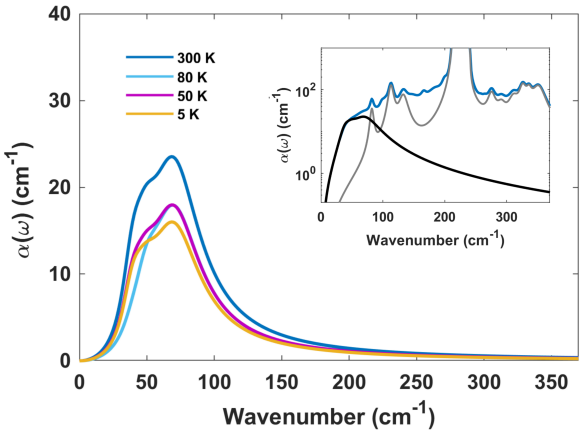

Figure 5.4: Absorption spectrum after removing the predicted in-plane phonon resonances and the few major peaks lacking a clear identification. A general absorptive background is highlighted across the low energy spectrum, showing an increasing transparency with the lowering temperature. The inset shows the contribution of the absorptive background (black curve) to the total absorption coefficient at 300 K (blue curve). The gray curve shows the contributions coming from the known phonon peaks.

thermalize the phonons to the equilibrium Bose-Einstein distribution, a non-thermal phonon population (hot phonons) can build up, eventually limiting the electronic transport properties of the system. This is especially true in 2D materials, where the reduced dimensionality decreases the density of decay channels[234].

The increase in the material transparency to FIR radiation with decreasing temperature, as seen in Fig. 5.3c, suggests an important role of anharmonicity in the vibrational spectrum of CrI_3[235,236,230]. To further analyze these anharmonic effects, we studied the central frequency shift and line-width variation of the phonon absorption peaks as a function of temperature. We highlight this process in Fig. 5.5 and 5.6 for eleven different phononic excitations indexed in terms of their central frequency (at 300 K) and symmetry: P1 (82 cm^{-1}, E_u), P2 (113 cm^{-1}, E_u), P3 (133 cm^{-1}, A_{2u}), P4 (276 cm^{-1}, $E_u + E_g$), P5 (291 cm^{-1}, $E_g + A_{2u}$), P6 (310 cm^{-1}, $E_u + A_{1g}$), P7 (326 cm^{-1}, $E_u + E_g$), P8 (337 cm^{-1}, $E_u + E_g$), P9 (347 cm^{-1}, $E_u + E_g$), Q1 (224.5 cm^{-1}, E_u), Q2 (231.5 cm^{-1}, E_u). Fig. 5.5a shows the contribution of the three lowest-frequency phonons to the absorption coefficient. Their central frequency shifts as a function of temperature are shown in Fig. 5.5b. The values are normalized with respect to the 5 K central frequency of the three modes, while the single curves have been shifted by a vertical offset for clarity. The sharp difference in the central frequency of peak P1 (blue) and P3 (green) between 250 K and 200 K can be associated to the structural first order transition predicted for CrI_3, which converts the crystal structure from monoclinic to rhombohedral, affecting both the in-plane and out-of-plane atomic distances[200]. Apart from these structural changes, only small deviations can be resolved in the frequency softening with increasing temperature, suggesting weak thermal expansion (quasi-harmonic) and phonon scattering (anharmonic) contributions. Indeed, information on the phonon scattering mechanism can be obtained by the study of both the line-widths and frequency shifts of the phonon modes, as highlighted in Eq. 5.5 and 5.4 (see section §5.5), respectively. As we look at the line-widths behavior with temperature in Fig. 5.5c, it is possible to highlight three different patterns. P1 shows weak phonon interactions, as expected for the lowest

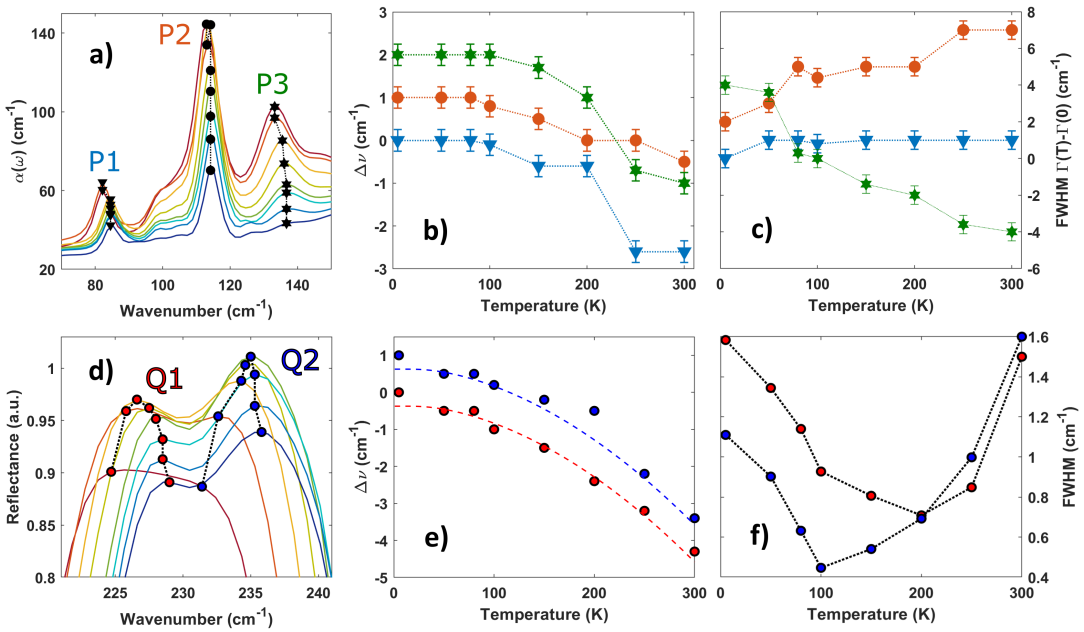

Figure 5.5: Frequency shift and line-width variation of the CrI_3 vibrational modes with temperature. a) Depiction of three low frequency modes in the FIR absorption spectrum. The black points highlight the temperature evolution. **b-c)** Central frequency and line-width evolution of the P1, P2 and P3 phonon modes. The dotted lines are a guide for the eye. The values have been plotted as a difference with respect to the 5 K value, and shifted by an offset for clarity. Error bars are extracted from the best fitting process of the Lorentzian function. **d)** Reflectance window highlighting the Q1 and Q2 phonon modes at varying temperature. **e-f)** Central frequency and line-width evolution of the Q1 and Q2 phonon modes. The values for the frequency shift have been plotted as a difference with respect to the 5 K value, and shifted by an offset for clarity. Discontinuous lines highlight the best fitting procedure in accordance to Eq. 4.3.

energy modes, due to the reduced density of available decay channels. P2, instead, seems to show a minor increase of the line-width with the growing temperature. This is indeed a fingerprint of an anharmonic effect given by ph-ph interaction, since the decay channels due to multiple phonon scattering increase at higher temperatures due to the growing phonon population. P3 follows a complete opposite behavior with respect to P2, as it predicts a decreasing line-width (higher decay times) with the growing temperature. This growth is sharply enhanced below the Curie temperature where the peak also starts to disappear completely from the absorption spectrum. However, above the magnetic transition, the softening of the line-width with the increasing temperature cannot be explained in terms of ph-ph scattering process. The hardening of phonon modes with increasing temperature is usually associated to an e-ph interaction, since the e-ph line-width is proportional to the difference between the occupations of states

below and above the Fermi energy. However, the decay channel of such a low frequency mode suggests the presence of an electronic continuum at low energies and across the whole range of measured temperatures, which is not expected by the band structure and ARPES data for CrI_3[237]. Additional causes contributing to this effect can be found in the structural transition, addressing the modifications between 250 K and 200 K, and in the presence of a residual magnetic scattering pathway above the Curie temperature. Indeed, similar effects have been found in the iso-structural material α-$RuCl_3$, where a broad magnetic continuum has been found to survive up to 100 K[230,175], well above the magnetic ordering temperature of 14 K.

Near 230 cm^{-1} two strong Cr E_u vibrational modes (Q1 and Q2, see Fig. 5.5d) dominate the absorption spectrum. This double nature is hidden at 300 K by the reststrahlen effect and starts to appear at low temperatures due to a reduction of the modes line-width. On purely symmetric grounds, only a single E_u mode is expected by the D_{3d} point group. However, DFT+SOC calculations[201] have proved the presence of an additional nearly degenerate mode. The expected frequency separation is predicted to be smaller than 1 cm^{-1} both in the ferromagnetic and anti-ferromagnetic ground state. This is clearly in contrast to the shift observed experimentally, nearly 7 cm^{-1} and constant with temperature. The splitting of optical phonons in semiconductors is usually related to the long-range Coulomb screening which causes the longitudinal mode to increase in frequency with respect to the transverse ones[238], as described by the Lyddane-Sachs-Teller (LST) relation[239]. Further anharmonic mechanisms given by the ph-ph interaction can also be neglected due to the temperature independence of the frequency difference, altogether with effects coming from the magnetic order, leaving the spin-orbit coupling and Coulomb screening as the possible contributors. Indeed, such a massive frequency separation would suggests a massive SOC in CrI_3, as already pointed out in other works[210]. Moreover, the LST mechanism is ruled out in 2D layered structures[240], thus the future probing of the monolayer CrI_3 infrared activity would shine light on the origin of this splitting.

The temperature modulations of the Q1 and Q2 modes are shown in Fig. 5.5e and 5.5f, for the frequency shift and line-width behavior respectively, obtained from the reflectance analysis fit at different temperatures. From the knowledge of the thermal expansion coefficient and Grüneisen constants for the CrI_3 lattice vibrations[229], the quasi-harmonic term in Eq. 5.4 given by the lattice expansion has been found negligible in the analysis of the frequency shift of all modes. The presence of 3- and 4-scattering anharmonic terms in the Cr E_u modes is thus proved by the frequency shift. The results for the model equation coefficients are shown in table 5.3 and in Fig. 5.5e as discontinuous fitting lines. The four-scattering processes contribute strongly to both Q1 and Q2, while the three-scattering ones have been found non-negligible only for Q2.

This result can be explained in terms of the low DOS of phonons at disposal for the decay process, constraining the Q1 and Q2 modes to interact with many low energy modes. Differently, the analysis of the line-width of Q1 and Q2 cannot be completed through the simple ph-ph scattering processes described by Eq. 5.5. As already visible in the reflectance behavior in Fig. 5.5d, the phonons Lorentzian line-widths follow a

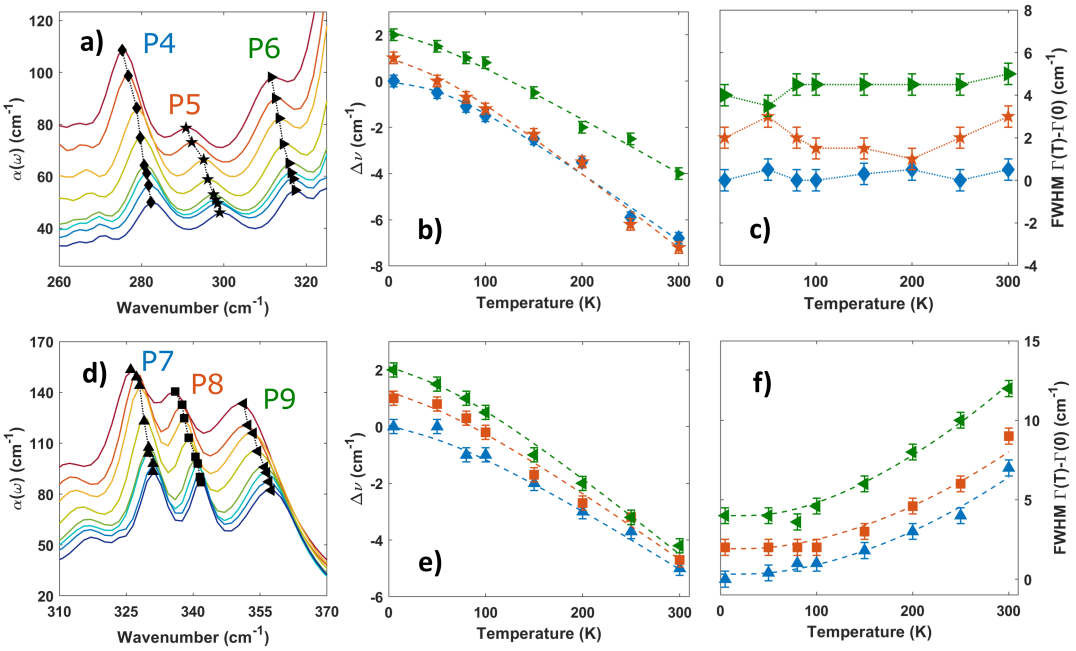

Figure 5.6: Frequency shift and line-width variation of the CrI_3 vibrational modes with temperature. a) Frequency modes in the FIR absorption spectrum: P4, P5 and P6. **b-c)** Frequency and line-width evolution with temperature of the vibrational modes: P4, P5 and P6. The values are plotted as a difference with respect to the 5 K value, and shifted by an offset for clarity. The frequency shifts are fitted (discontinuous lines) by the model of Eq. 5.4. Error bars are extracted from the best fitting process of the Lorentzian function. **d)** Highest frequency modes in the FIR absorption spectrum: P7, P8 and P9. **e-f)** Frequency and line-width variation with temperature for P7, P8 and P9 phonon modes. The values are plotted as a difference with respect to the 5 K value, and shifted by an offset for clarity. Discontinuous lines highlight the best fitting procedure in accordance to Eq. 5.4 and Eq. 5.5.

steep decreasing slope with increasing temperature before slowing down from 100 K and inverting the behavior at 200 K for Q1 and already at 100 K for Q2. Similar features have been observed for the reststrahlen band in α-$RuCl_3$ [230]. This effect has been linked to the stacking sequence, proposing that in α-$RuCl_3$ the stacking order and stacking sequence play a fundamental role in determining the overall reflectance, actually boosting the reflectance by a factor of two across the structural transition. However, this is not the case for CrI_3, where the reflectivity enhancement is merely 10%. Moreover, for the lower energetic phonon modes, the modifications induced by the structural transition do not disperse across a broad interval of temperatures, thus suggesting a different origin for the line-width variation with temperature of Q1 and Q2. At low temperatures, this behavior can be explained in terms of the same processes introduced for P3, while in the high temperature regime the anharmonic phonon processes dominate the temperature

	P4	P5	P6	P7	P8	P9	Q1	Q2
A (cm^{-1})	-2.7	-3.6	-3	-1.8	-2.2	-3.7	0	-0.2
B ($\times 10^{-2}$ cm^{-1})	-4.5	-1.3	-1	-18	-20	-5	-12	-18
C ($\times 10^{-1}$ cm^{-1})	-	-	-	-4	-3.8	-18	-	-
D ($\times 10^{-1}$ cm^{-1})	-	-	-	-5	-5.4	-6	-	-

Table 5.3: Fitting parameters of Eq. 5.4 and 5.5 for the vibrational modes highlighted in Fig. 5.5 and 5.6. For all values, a 20% relative uncertainty must be considered, as extracted by the best fitting process.

dependence. Indeed, these results for Q1 and Q2 also support the idea of a magnetic dissipation pathway existing above the Curie temperature.

Similarly to the mode Q1 and Q2, blue shifts with decreasing temperature can be highlighted also for the higher energy modes seen in Fig. 5.6a. As previously discussed, these modes can be described by a linear superposition of the 230 cm^{-1} E_g Raman or IR modes with further low energy lattice excitations. Since the line-width of these excitations are constant across the temperature range (see Fig. 5.6c, the Q1 and Q2 modes line-width is small with respect to the P4, P5 and P6 one), we report in table 5.3 only the coefficients of Eq. 5.4 for the frequency shift, obtained from the best fit curves shown in Fig. 5.6b as discontinuous lines. The results highlight a dominant contribution given by the three-scattering processes, as expected for high frequency modes due to the high phonon DOS at lower energies participating to the decay mechanism.

To fully conclude the anharmonic analysis, we consider the highest energy modes highlighted in Fig. 5.6d, which are again given by a linear superposition of lower frequency IR- and Raman-active phonons. The frequency shift and line-width variation suggests strong ph-ph scattering processes, with a dominant contribution given by the three-scattering pathways for the frequency shift, similarly to P4, P5 and P6. The best fit results for Eq. 5.4 and 5.5 are shown in table 5.3 and as discontinuous curves in Fig. 5.6e and 5.6f. Indeed, the magnitude of the line-width variation with temperature is a fingerprint of strong anharmonicity caused by the high density of lower energetic decay channels.

5.4 Conclusions

The results highlighted in this chapter suggest a complex low-energy optical response of bulk CrI_3. In the NIR spectral range, it possesses an insulating optical gap around 1.1 eV at 300 K which strongly depends on temperature, showing a robust hardening for decreasing T. This hardening is due to a huge electron-phonon interaction which is reinforced below the Curie critical temperature at nearly 60 K. This indicates a complex interaction scenario among lattice, electronic and magnetic degrees of freedom in CrI_3

system.

By studying the far-IR/THz absorption spectrum, several phonon peaks are observed that can be assigned in agreement to the D_{3d} point group symmetry and DFT calculations. The finding of some magnetic-sensitive peaks could be the first experimental evidence that these lowest-frequency absorptive terms exhibit strong spin-phonon coupling. The phonons absorption is also superimposed to a broad background already visible at 300 K and having a decreasing magnitude with T. This is at variance with the isostructural α-$RuCl_3$ compound, where the absorption background increases at low-T and has been associated mainly to Kitaev spin liquid excitations. Although CrI_3 has been suggested to be a candidate to host similar fractionalizated excitations, as indicated by recent theoretical results[241] and by the discovery of gapped Dirac magnon dispersions[210], this absorption background could have a different origin probably related to the strong lattice anharmonicities. Indeed, the study of the IR phonons reveal significant modes softening and line-width changes with varying temperature, described in terms of multi-phonon and spin-phonon scattering processes. An anomalous behavior of the vibrational modes at 133 cm^{-1} (A_{2u}) and near 230 cm^{-1} (E_u) can be highlighted, suggesting a spin-phonon coupling at lower energies extending for temperatures above the magnetic transition. These results suggest CrI_3 as a material hosting strong correlations, picturing a complex interplay between the lattice, magnetic and electronic degrees of freedom.

5.5 Methods: Models for anharmonic phonon scattering

The variations in line-width and frequency shift of the vibrational modes with temperature can be examined through the theory of anharmonic phonon-phonon interactions and thermal expansion of the lattice[242,243]. In particular, the frequency shift $\Delta\nu$ of the phonons at constant pressure arises from a pure-volume contribution $(\Delta\nu)_{latt}$ resulting from thermal expansion, plus pure-temperature contributions $(\Delta\nu)_{anh}$ given by phonon-phonon scattering anharmonicities[243–245]

$$\Delta\nu = (\Delta\nu)_{latt} + (\Delta\nu)_{anh} \tag{5.3}$$

The cubic and quartic anharmonicities are described by factors which include contributions from three- and four-phonon anharmonic processes. Equation 5.3 can be written as[244,245]

$$\Delta\nu = \nu_0 \left(e^{-\gamma\beta T} - 1\right) + A\left[1 + \frac{2}{e^{h\nu_0/2k_BT} - 1}\right] + \tag{5.4}$$

$$+B\left[1 + \frac{3}{e^{h\nu_0/3k_BT} - 1} + \frac{3}{(e^{h\nu_0/3k_BT} - 1)^2}\right]$$

where ν_0 is the zero Kelvin frequency, approximated by the 5 K experimental value in fitting process. The coefficient $\gamma\beta$ is given by the product of the Grüneisen parameter

γ and the volume thermal expansion coefficient β, while A and B are coefficients that weight the three- and four-phonon anharmonic processes, respectively.

A similar result can be written for the line-width behavior of the vibrational modes, which gives information on the decay processes in act. Indeed, the dominant decay process involves the annihilation of the original phonon and the creation of two or three lower energy phonons. These second-generation phonons are typically acoustic and in turn decay into even lower energy vibrations, eventually reaching equilibrium with the thermal bath. Since the ph-ph scattering processes are sensible to the phonon population, this induces a dependence of the line-width of the single modes from temperature. The resulting relation follows the same analytical form of Eq. 5.4, but with the benefit of having a null dependence on the quasi-harmonic term induced by the lattice dilation

$$\Gamma(T) = \Gamma_0 + C\left[1 + \frac{2}{e^{h\nu_0/2k_BT} - 1}\right] + D\left[1 + \frac{3}{e^{h\nu_0/3k_BT} - 1} + \frac{3}{(e^{h\nu_0/3k_BT} - 1)^2}\right] \quad (5.5)$$

Here Γ_0 is the line-width at $T = 0$ K and the coefficients C and D are constants characterizing the contribution of the three- and four-phonon processes to the line-width, respectively.

Part II

High Temperature Superconductivity in Nickelates

Chapter 6

Optical Study of Superconductivity in $Nd_{1-x}Sr_xNiO_2$

In the years after the discovery of the first theoretical models for superconductivity, higher values of T_c for the conventional theory seemed impossible to achieve, which led Cohen and Anderson to postulate in 1972 that a hard limit of 25 K must exist for the T_c of conventional superconductors. This idea, based on several misconceptions on material properties and stability limits, had a long-lasting detrimental impact in the field for the following decades. High-T_c cuprates, discovered in 1986, and iron-based superconductors, discovered in 2006, technically did not contradict the Cohen-Anderson limit, since in these cases superconductivity is not of conventional electron-phonon origin.

High temperature superconductivity (HTSC) remains a key problem in condensed matter. The challenge is well described by the cuprates, highly-correlated materials whose superconducting and normal-state properties are puzzling scientists even 35 years after their discovery[246]. One way to overcome this impasse is a "reasoning-by-analogy" approach, meaning the study of similar systems with a controlled degree of correlation. As such, the discovery of iron-based superconductors reinvigorated the field[247,248], while twisted bilayer graphene extended the question beyond bulk systems[249,250]. Due to the similar crystal and electronic structure with respect to cuprates[251,252], the family of nickelates is also a candidate for the study of HTSC. The compounds of this family have the perovskyte chemical formula $RNiO_3$ (R = rare-earth). Their structure can be modified into an infinite-layered one, analogous to cuprates, by removing the apical oxygens from the NiO_6 octahedra with reducing agents such as hydrogen (see Fig. 6.1). This is the so-called topotactic reduction which, in practice, may have unwanted consequences such as hydrogen intercalation into the sample[253]. The new Ni-based structure is built from 2D planes of NiO_2 interchanged with dopant ions that form spacer layers, equivalent to the CuO_2 planes in cuprates. The Ni atom features a nominal 1^+ oxidation state that provides the same $3d^9$ electronic configuration of Cu^{2+}

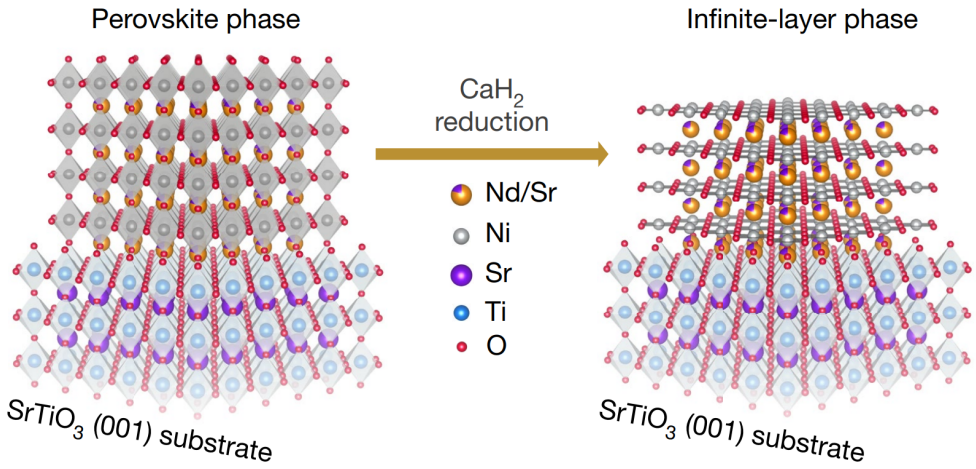

Figure 6.1: Topotactic reduction of nickelate thin films. Schematic crystal structures of $Nd_{0.8}Sr_{0.2}NiO_3$ (left) and $Nd_{0.8}Sr_{0.2}NiO_2$ (right) thin films on a $SrTiO_3$ (001) substrate. The figure is adapted from ref.[254].

in isostructural high-T_c cuprates. In reality, however, there are qualitative differences between the properties of these systems. For example, $LaNiO_2$, the first synthetized compund of this type, is weakly conducting and posses no magnetic order[255,256], while the cuprates on the contrary are insulating antiferromagnets in their parent phases.

Moreover, no superconductivity has been found so far in the parent phases of nickleates. This can emerge only via charge carrier doping as in the cuprates, which represents an additional challenge since it has only been achieved by means of thin-film growth (limited to ∼10 nm) techniques like pulsed laser deposition (PLD) and molecular beam epitaxy (MBE)[257], while superconductivity in doped bulk samples is yet to be reported. In this context, a superconductive phase was recently verified experimentally in Sr-doped $NdNiO_2$ thin films grown on STO substrates, more than 20 years after their first theoretical prediction[258]. It was soon followed by the discovery of a superconductive phase in Sr-doped (Pr/La)NiO_2 and Ca-doped $LaNiO_2$.

The infinite-layer nickelate $Nd_{1-x}Sr_xNiO_2$ is synthesized via softchemistry topotactic reduction[259] on a STO substrate. The phase diagram of $Nd_{1-x}Sr_xNiO_2$ shows a superconductive dome, with the highest critical temperature (of about 15 K) at Sr doping $x = 0.2$[260]. The presence of the STO substrate is essential for producing the superconductive phase, giving an unusual picture in which the substrate both strains the crystal and stabilizes this phase. Moreover, Hall measurements[254] and ab-initio simulations[261–265] highlighted a complex picture behind the symmetry of the order parameter, in which the superconductive mechanism appears inconsistent with the picture of a simple hole doped electronic band. Indeed, the description of the electronic structure near the Fermi level might require up to three bands and their hybridization[266], and contributions coming from the $4f$ shells have also been proposed[267]. Furthermore, the role of electronic correlations has been pointed-out recently[268], although an estimate of

their importance is still lacking. On the other hand, the electron-phonon coupling has been ruled out as the exclusive origin of the observed superconductivity [266], with spin fluctuations playing a key role despite the absence of long-range magnetic order [265,269].

To determine the superconducting gap (2Δ) and the pairing mechanism of the superconducting state, Terahertz (THz) or microwave absorption spectroscopy [270–272], tunneling spectroscopy [273], specific heat [274,275], and London penetration depth techniques are the prevailing experimental methods. In the case of $Nd_{1-x}Sr_xNiO_2$, London penetration depth measurements produce consistent data between different independent reports [276,277], but the paramagnetic background and limited quality of the samples leave the interpretation open for further debate. Moreover, tunneling measurements on $Nd_{1-x}Sr_xNiO_2$ were also performed [278], suggesting the presence of two different superconducting gaps at 3.9 meV and 2.35 meV.

On the other hand, no optical investigations of superconductive $Nd_{0.8}Sr_{0.2}NiO_2$ films were reported, due in part to the presence of the $SrTiO_3$ substrate, reflecting close to 100% of the THz light through its soft phonon mode. Since optical investigations contributed a great deal to shed light on the high temperature superconductivity mechanism through evaluations of the superconductive gap, the penetration depth, the scattering mechanism and coherence effects [279–284], these measurements are highly longed for.

This chapter reports on the optical reflectance $R(\omega)$ of an optimally doped $NdSrNiO_2$ film over a STO substrate across a broad range of frequencies ω, from Terahertz (THz) to visible light (VIS), as obtained by combining THz radiation, generated from the AILES beamline@Soleil third generation synchrotron machine, with conventional optical spectroscopy. The normal-state optical conductivity, derived from these measurements, is described by a superposition of a Drude term and an absorption band in the Mid-IR. This scenario is common to other metallic oxides including cuprates and suggests an important role of electronic correlations in the NiO_2 plane. In the superconducting state, the energy gap (2Δ) is evaluated by fitting the THz reflectance at different temperatures with the Mattis-Bardeen model. Additionally, an estimation of the magnetic penetration depth is obtained through the study of the Drude spectral weight transfer to the Cooper pairs.

6.1 Normal State Analysis

All reflectance measurements were performed on a 10 nm thick, optimally doped $Nd_{0.8}Sr_{0.2}NiO_2$ film, grown on a 500 μm $SrTiO_3$ (STO) (001) substrate (see Fig. 6.2a), through the soft chemistry topotactic reduction using CaH_2 as described in ref. [260]. The film optical properties from THz to VIS have been probed using a combination of different spectrometers. The THz reflectance measurements have been performed at the infrared spectroscopy beamline AILES (Advanced Infrared Line Exploited for Spectroscopy), Synchrotron SOLEIL [285]. Exploiting the high brightness of the synchrotron radiation source. THz spectra in the $10-600$ cm^{-1} range were obtained using a Bruker IFS125HR Fourier transform spectrometer evacuated at pressures lower than 10^{-4} mbar to avoid absorption by water and residual gas. The ($10-60$ cm^{-1}) spectral range has been

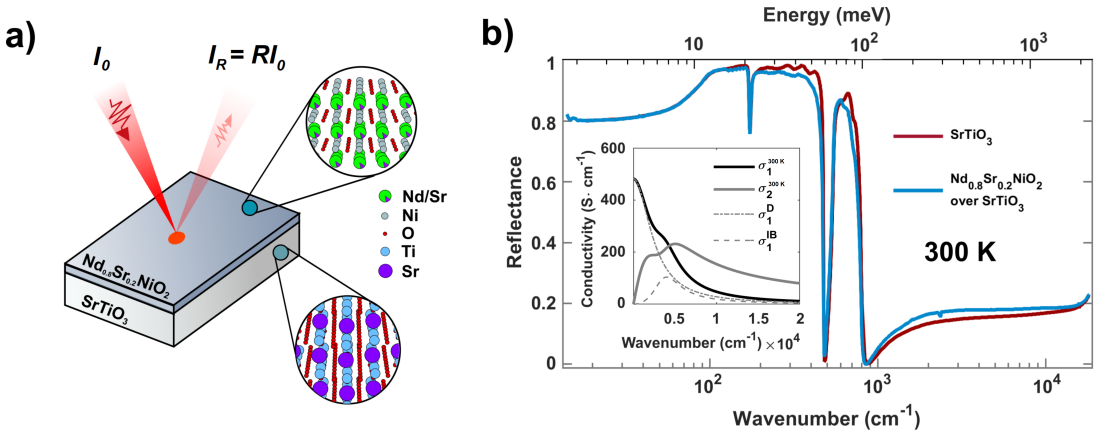

Figure 6.2: — Reflectance spectroscopy of a $Nd_{0.8}Sr_{0.2}NiO_2$/STO thin film. **a)** Schematic view of $Nd_{0.8}Sr_{0.2}NiO_2$/STO thin film sample and incoming I_0 and reflected light intensity $I_R = RI_0$ (R is the reflectance). Crystal structures are represented in the magnification circles. **b)** Broadband reflectance spectra of $Nd_{0.8}Sr_{0.2}NiO_2$/STO thin film (light blue line) and STO substrate (red line) at room temperature. The real (σ_1) and imaginary (σ_2) part of the film's optical conductivity at 300 K are plotted in the inset together with the (σ_1^D) Drude (dashed-dotted line) and (σ_1^{IB}) Mid-IR band (dashed line) fitting results.

measured with a resolution of 0.5 cm^{-1} using a 50 microns Mylar beamsplitter combined with a bolometer cooled at 1.6 K having a signal-to-noise ratio of 1700:1. The error bar on the measured reflectivity is 0.2%. For the (40 – 600 cm^{-1}) range, the spectral resolution of 2 cm^{-1} were obtained using a 6 microns Mylar combined with a bolometer cooled at 4.2 K. Above 600 cm^{-1}, a MCT detector cooled at 4.2 K was used, together with a KBr beamsplitter. A low vibration pulse tube cryostat was used to achieve temperatures down to 5 K from room temperature. This system contains a sample holder which is mechanically decoupled from its cold finger, allowing minimum sample vibrations. The absolute reflectance spectra were obtained by measuring the signal reflected in the THz divided by the signal of the gold evaporated sample. Broadband room temperature measurements have been obtained at the Sapienza Terahertz Laboratory at Sapienza University of Rome, through a Vertex 70v FTIR broadband interferometer, for frequencies between 50 and 5000 cm^{-1}, and a JASCO v-770 IR-UV spectrometer for the interval from 3000 to 20000 cm^{-1}.

The optical reflectance measured at room temperature is shown in Fig. 6.2b, across a wide range of frequencies, from THz to VIS for both $Nd_{0.8}Sr_{0.2}NiO_2$ film and bare STO substrate. For the STO substrate, a series of strong transverse optical (TO) phonon modes is observed. Starting from lower frequencies, these can be identified as[286,287]: TO_1 at 100 cm^{-1} (soft mode), TO_2 at 176 cm^{-1} and TO_3 at 540 cm^{-1}. The reflectance of $Nd_{0.8}Sr_{0.2}NiO_2$ film shows a similar behavior of STO with a small decrease above 200 cm^{-1}, mainly related to the Drude metallic absorption, and an increase above 1000

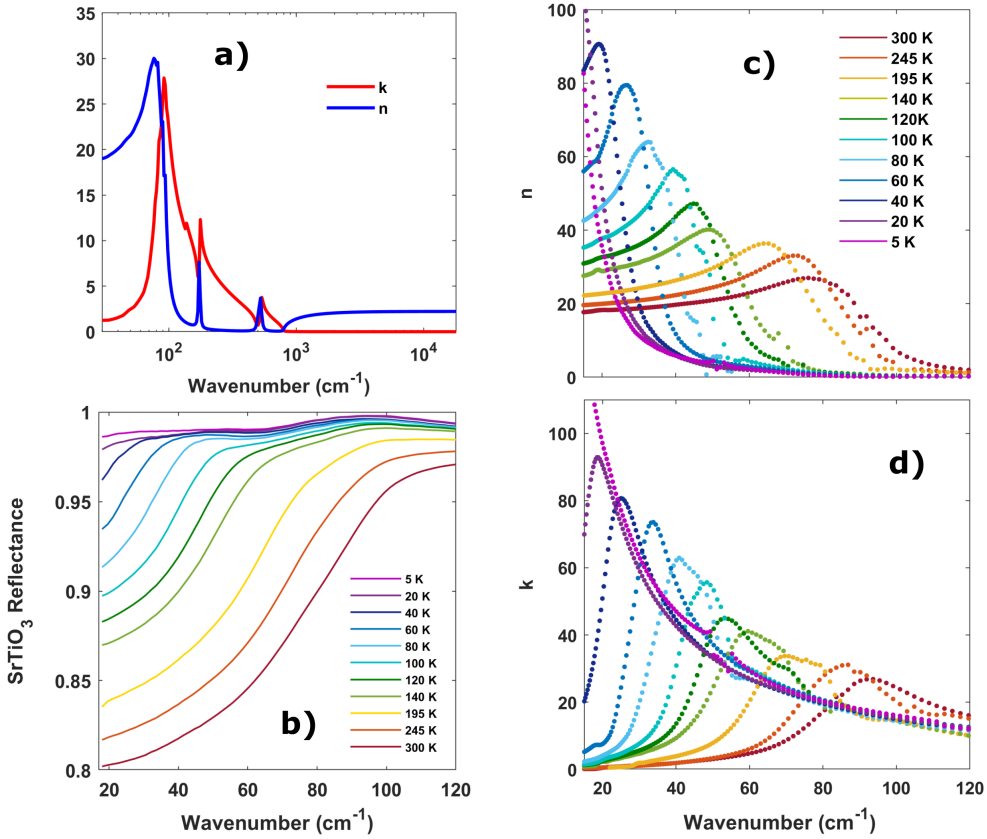

Figure 6.3: a) Broadband optical indices of the $SrTiO_3$ substrate at 300 K. The results are in accordance with previous works[288]. **b)** THz reflectance of the $SrTiO_3$ substrate as a function of temperature. The soft phonon mode is clearly shifting toward lower frequencies by decreasing temperature. **c-d)** Extracted optical constants n (c) and k (d) for the STO substrate for temperatures between 5 and 300 K in the energy range below 120 cm^{-1} (soft mode region).

cm^{-1} associated to an absorption band in the infrared spectral region (see discussion of Eq.6.1). Due to its limited thickness, below 200 cm^{-1} the film absorption dampens and the reflectance converges to the one of the bare substrate.

To analyze the behaviour of the $Nd_{0.8}Sr_{0.2}NiO_2$ film, it is necessary to consider the optical response of the substrate. The $SrTiO_3$ substrate possesses well known optical features in the low energy spectrum. In particular, due to its incipient ferroelectric nature, a soft phonon mode is expected, with a strong dependence on temperature. This can be seen in Fig. 6.3b, where the absolute reflectance increases at THz frequencies with decreasing temperatures. This is due to the strong red shift of this soft mode. The absolute reflectance of the substrate was fitted using a Kramers-Kronig constrained fit of a multi-oscillators Lorentz model. The results are shown in Fig. 6.3, being in

accordance with the known literature[288]. The $Nd_{0.8}Sr_{0.2}NiO_2$ film is modeled in terms of an air/film/STO trilayer (see Eq. B.1) and fitted through the RefFit program. In particular, the optical properties of $Nd_{0.8}Sr_{0.2}NiO_2$ have been described in the normal state in terms of a Drude-Lorentz model. The complex conductivity expressed in units of $S \cdot cm^{-1}$ takes the form[289]

$$\sigma(\omega) = \frac{2\pi}{Z_0}\frac{\omega_p^2}{\Gamma - i\omega} + \frac{2\pi}{Z_0}\frac{\omega\omega_{p_L}^2}{\gamma\omega - i(\omega_0^2 - \omega^2)} \tag{6.1}$$

where Z_0 is the free space impedance (377 Ω) and the frequencies are expressed in units of cm^{-1}. In the Drude term, ω_p is the Drude plasma frequency while $\Gamma = 1/\tau$ is the scattering rate, with τ being the scattering time. The Lorentz oscillator is instead described by its characteristic frequency (ω_0) and intensity ($\omega_{p_L}^2$) and scattering rate γ. In the fitting procedure, the real (n) and imaginary (k) parts of STO refraction index have been used as inputs in Eq. B.1, taking into account the contribution to the reflectance coming from the substrate layer.

The use of a two-oscillators model (Drude+MIR band) might seem trivial for the understanding of such a complex material. However, the best fit procedure suggests the presence of a broad Drude contribution coming from the high intraband scattering rate. This is actually in agreement with the bad metallicity predicted for this material[254], which is 10 times smaller than the one expected from cuprates single crystals like BSCCO[290], even if a high density of carriers is predicted by Hall measurements ($\sim 10^{21}$ cm^{-3})[260]. Moreover, the use of the model in Eq. 6.1 is supported by the literature covering the optical conductivity of cuprates[280]. Here, the description of the optical conductivity strongly depends on temperature, doping, and the type of cuprate family[291–294]. In such a complex framework, the modeling of the conductivity, in particular for thin films, should minimize the number of absorption terms to be put in Eq. 6.1. The model based on two oscillators is sufficient to fit the reflectance curve for $Nd_{0.8}Sr_{0.2}NiO_2$ up to the VIS spectrum, where the differences in reflectance between the bare substrate and the film/substrate are small and can be fitted by the MIR interband and Drude tail contributing to the optical conductivity. Indeed, the MIR band may be contaminated by coherent contributions coming from transitions between bands close to the Fermi level or more generally by the interband transitions, which could be located at energies higher than the MIR feature. However, these contributions are expected to just add a small amount of spectral weight[295].

The inset of Fig. 6.2b shows the real ($\sigma_1(\omega)$, black line) and imaginary part ($\sigma_2(\omega)$, gray line) of the optical conductivity for the $Nd_{0.8}Sr_{0.2}NiO_2$ film in its normal-state together with the Drude term (dashed-dotted line) and the MIR band (dashed line). A Drude plasma frequency $\omega_p \simeq 8500$ cm^{-1} is extracted from the fitting, together with a scattering time $\tau \sim 1.39 \times 10^{-14}$ s. Such a low scattering time is probably related to the quasi-2D geometry of the material. The DC conductivity is comparable to the best films produced[260]. However, a direct comparison with literature is not possible since the resistivity might be affected by the presence of more intercalating hydrogen during the reduction process[260]. The MIR band is centered at $\omega_0 = 4000$ cm^{-1} with

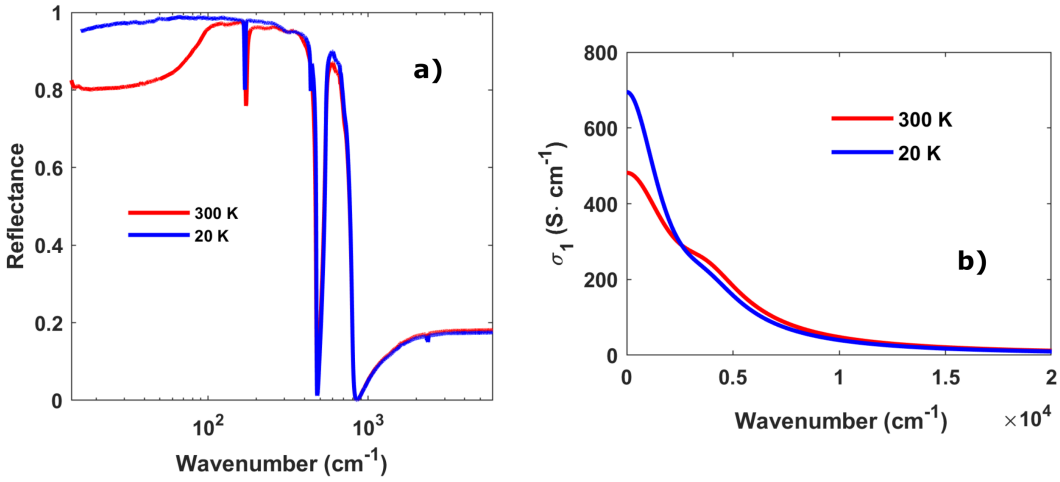

Figure 6.4: a) Infrared reflectance of the $Nd_{0.8}Sr_{0.2}NiO_2$ film over STO at 300 K and 20 K. **b)** Broadband real conductivity of the $Nd_{0.8}Sr_{0.2}NiO_2$ film at 300 K and 20 K.

an amplitude $\omega_{pL} = 5000$ cm^{-1} (all fitting parameters are reported in Table 5.2 of SI). The MIR band is a common feature of many transitional metal oxides including cuprate- and iron-based superconductors, being related to electronic correlations. These usually renormalize the Drude term (coherent charge excitations), transferring spectral weight to an incoherent one at finite frequency (MIR band)[296]. In particular, the $\omega_p^2/(\omega_p^2+\omega_{pL}^2)$ ratio provides an experimental estimate of the degree of electronic correlation of the material[297]. While for weakly correlated metals, such as gold and silver, one obtains $\omega_p^2/(\omega_p^2+\omega_{pL}^2) \to 1$, for $Nd_{0.8}Sr_{0.2}NiO_2$ this ratio reaches a value of about 0.74. This number can be compared to other correlated oxides like V_2O_3 (~ 0.18) and cuprates (0.2 - 0.4)[295], identifying $Nd_{0.8}Sr_{0.2}NiO_2$ as an intermediate correlated system.

At 20 K, above the superconducting transition, the fitting on the reflectance spectrum (see 6.4a) provides similar results for the optical conductivity, with a 20% increase in the Drude scattering time (see Fig. 6.4b), as expected for a coherent metallic transport. A small spectral weight transfer from higher frequencies is also observed when comparing the broadband conductivity at 300 and 20 K, that is a property commonly shown by correlated materials. Indeed, a spectral weight conservation is achieved by integrating the conductivity in this wide spectral range. With the scattering time value at 20 K ($\tau \sim 1.7 \times 10^{-14}$ s), it is possible to estimate whether the nickelate is in a clean limit for superconductivity ($\hbar/\tau \ll 2\Delta$) or in the dirty one ($\hbar/\tau \approx 2\Delta$). As an initial assumption, we may take the $2\Delta = 3.9\ meV$ value as a reference for the superconductive gap, as obtained by tunneling spectroscopy measurements[278]. By calculating the ratio $\hbar/2\Delta = 1.7 \times 10^{-13}\ s$ and comparing it with the scattering time τ, we obtain $\tau < \hbar/2\Delta$. This result suggests that the material is in the dirty limit, granting the possibility to extract the superconducting gap from optical measurements.

The scattering time τ can be also related to the critical temperature T_c of the

superconductor through the well known relation $\hbar/\tau \approx 2k_BT_c$, which is valid for cuprate high temperature superconductors, both in the bulk[289] and thin film limit[298]. This relation finds its origin in the scaling factor for cuprates proposed by Homes et al.[299,300] and supported by Tallon et al.[301], in which the normal state conductivity is established to be proportional to the product of the superfluid density with T_c. The result for the nickelate film, however, strongly departs from this relationship. Indeed, $\hbar/\tau$ is more than one order of magnitude higher than $2k_BT_c$: $\hbar/\tau \sim 38.7\ meV \gg 2.2\ meV \sim 2k_BT_c$. Some of the physical phenomena suggested as origin to this scaling relation in cuprates[301] are a marginal Fermi-liquid state, Josephson coupling between planes, the scattering of impurities for a d-wave order parameter and even a BCS dirty limit superconductivity. Thereby, an exact physical interpretation of these results seems unclear and it adds to the list of differences between the nickelate and cuprate families.

6.2 Superconductive State Analysis

THz reflectance measurements of film and substrate have also been performed as a function of temperature between 5 to 20 K, crossing for the film its superconductive critical temperature at $T_c \sim 13$ K and in the frequency range 15 to 50 cm^{-1} (all curves at different T merge above this frequency). Figure 6.5a shows the STO reflectance in this temperature and frequency range in a very expanded vertical scale. The increase in the substrate reflectance at low frequencies is due to the STO soft mode. In contrast, R(ω) of the film in the same temperature and frequency range (Fig. 6.5b) shows a larger red shift suggesting a further effect induced by the superconducting transition.

To magnify this effect, the relative reflectance spectra $\Delta R/R$ is obtained dividing the deviation from 20 K of the light intensity reflected by the film or STO at all temperatures $(I_R(T) - I_R(20K))$ by the signal $I_R(20K)$ at the reference temperature $T = 20$ K ($> T_c$). The results are shown in a 2D intensity-plot for STO and $Nd_{0.8}Sr_{0.2}NiO_2$ film (Fig. 6.5c,d, respectively) as a function of both temperature and frequency. The 2D plots clearly highlight the differences between the bare substrate and the film Terahertz properties *vs.* T, supporting a different origin for the modification of the reflectance spectra at the lowest temperatures.

To extract the superconducting gap and its temperature dependence, the film relative reflectance $\Delta R/R = [R(T < T_c) - R(20\ K)]/R(20\ K)$ is fitted at various temperatures. In the dirty limit of the electron transport, the fitting process can be worked out by using the Mattis-Bardeen theory[302]. The choice of using the relative reflectance measurements for the understanding of the superconducting transition is mainly justified by to the high substrate absolute reflectance. Indeed, relative measurements grant a higher sensitivity when comparing different temperatures, and the use of the Mattis-Bardeen theory for the study of superconductive materials is well documented[303–305]. The real $\sigma_1^{sc}(\omega)$ and imaginary $\sigma_2^{sc}(\omega)$ parts of the optical conductivity in the superconducting state, normalized to those of the normal state $\sigma_N(\omega)$, take the form[302]

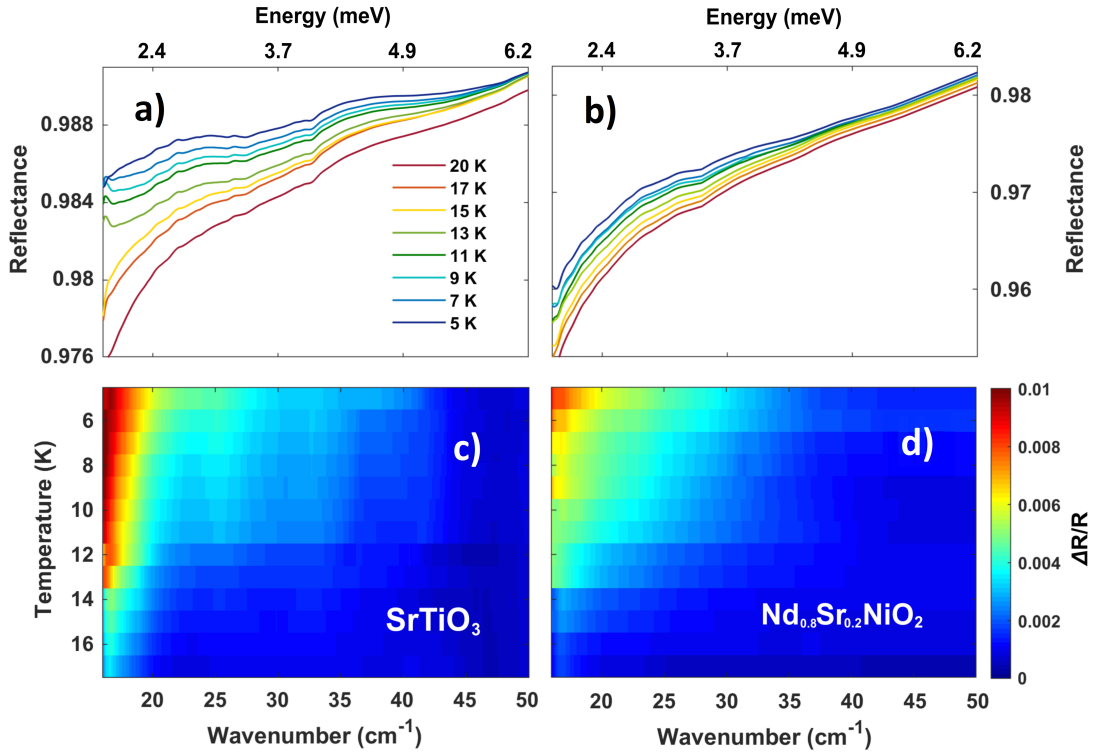

Figure 6.5: Temperature dependent analysis of a $Nd_{0.8}Sr_{0.2}NiO_2$/STO THz reflectivity. a) Absolute THz reflectance of the STO substrate at different temperatures. **b)** THz reflectance of the $Nd_{0.8}Sr_{0.2}NiO_2$ film over substrate at different temperatures. At frequencies ($\omega > 50$ cm^{-1}) the curves merge toward a common absolute value. **c-d)** Contour plots of the relative THz reflectance for both the sample and bare substrate, as a function of temperature (5 to 20 K) and frequency. Spectra were divided by measurement at 20 K.

$$\frac{\sigma_1^{sc}}{\sigma_N} = \left(1 + \frac{2\Delta}{\hbar\omega}\right) E(p) - 2\left(\frac{2\Delta}{\hbar\omega}\right) K(p) \qquad (\hbar\omega > 2\Delta) \tag{6.2}$$

$$\frac{\sigma_2^{sc}}{\sigma_N} = \frac{1}{2}\left\{\left(\frac{2\Delta}{\hbar\omega} + 1\right) E(p') + \left(\frac{2\Delta}{\hbar\omega} - 1\right) K(p')\right\} \tag{6.3}$$

where σ_N is mostly dominated by its real part at THz frequencies. For frequencies $\hbar\omega \leq 2\Delta$, the real part σ_1^{sc} is identically zero. $E(p)$ and $K(p')$ are the elliptical integrals of second and first kind, while the arguments p and p' take the form

$$p = |2\Delta - \hbar\omega|/|2\Delta + \hbar\omega|, \qquad p' = \sqrt{1 - p^2}$$

The best fit provides the value of the superconducting gap 2Δ whose behavior vs. T is shown in Fig. 6.6a. Here, 2Δ opens at T_c in agreement with the resistivity measurements of previous studies[254,260] and rapidly increases for reducing T. The extrapolation of 2Δ at 0 K is possible by fitting the T-dependence through the following equation[283,306]

$$2\Delta(T) = 2\Delta(0)\tanh\left(k\sqrt{\frac{T_c}{T}-1}\right) \tag{6.4}$$

where k is a coupling constant, T_c the critical temperature and $2\Delta(0)$ the superconducting gap at 0 K. Notice that, an error bar of ∼20% on the final gap values can be estimated from the analysis of the χ^2 evolution as a function of the gap (as represented by the gray shaded zone in Fig. 6.6a) Two options for the coupling constant values have been considered: 2.2 (red-dashed line in Fig. 6.6a), and 1.7 (blue-dashed line in Fig. 6.6a), which can be associated to a two-dimensional d-wave pairing mechanism and to a s-wave coupling, respectively[307]. Using $k = 2.2$, the extrapolation at 0 K gives $2\Delta(0)$ of 3.18 meV, while for $k = 1.7$ a slightly higher value of 3.42 meV is obtained. If instead the value of $T_c \sim 13\ K$ is fixed in Eq. 6.4 performing the fit, the values $k = 1.78 \pm 0.19$ and $2\Delta(0) = 3.31 \pm 0.14\ meV$ are obtained. Both values are, nonetheless, in agreement with the high-energy gap as obtained from tunneling measurements[278]. However, due to the strong contribution of the substrate to the reflectance measurements, the uncertainty of the superconducting gap extrapolation is too high to distinguish between the different coupling mechanisms (s-wave, d-wave or multigap superconductivity) proposed for nickelates[276,277].

Another fundamental quantity characterizing the superconducting state is the London penetration depth λ_L. This quantity can be estimated from the Ferrel-Glover-Thinkam Rule[308], describing the partial transfer of the Drude spectral weight to the superconducting condensate. This shift is schematically reported in Fig. 6.6b. The London frequency ω_L (expressed in cm^{-1}) can be calculated by the following equation[309]

$$\omega_L^2 = \frac{Z_0}{\pi}\int_0^{\omega_c}[\sigma_N(\omega') - \sigma_1^{sc}(\omega')]d\omega' \tag{6.5}$$

where the integral, i.e., the SW difference between the SC and normal state, converges when performed up to a frequency cutoff $\omega_c \simeq 500\ cm^{-1}$, containing the whole Drude spectral weight difference and falling in the measured spectral range. From ω_L, it is possible to calculate the penetration depth $\lambda_L = 1/2\pi\omega_L$[309]. The optical value for the penetration depth estimation at low temperature, $\lambda_L(5\ K) \simeq 490$ nm, is in agreement with results obtained with other techniques[276,310].

From a theoretical point of view, Bernardini et at.[311] reported a Density Functional Theory (DFT) calculation suggesting that electronic anisotropy is very high in $Nd_{0.8}Sr_{0.2}NiO_2$. The predicted values for λ_L range from 57 to 290 nm depending on the crystallographic direction and the state intercepting the Fermi level (hole or electron pocket). The largest value of λ_L for the β' electron pocket (∼ 290 nm) is in reasonable agreement with the London penetration depth value determined in this study (∼ 490

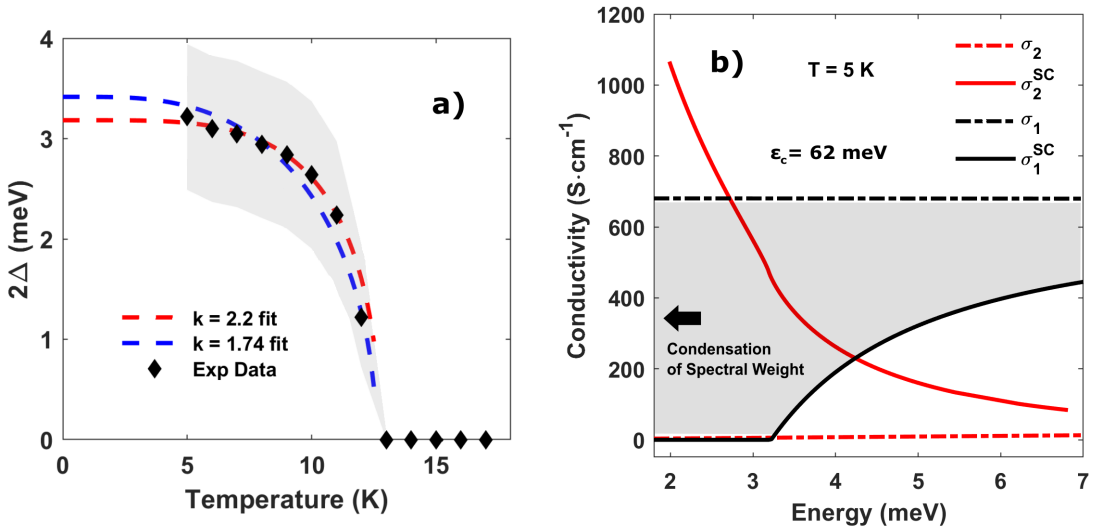

Figure 6.6: Superconducting gap of $Nd_{0.8}Sr_{0.2}NiO_2$ film. a) Superconducting gap value (black diamond) as function of temperature. The gray shaded area corresponds to the uncertainty range extracted from the fitting process, considering a 10% error over the χ^2 minimization. The experimental data can be described by Eq. 6.4, where the coupling constants $k = 2.2$ (red-dashed line) corresponds to a 2D d-pairing while $k = 1.7$ (blue-dashed line) corresponds to an s-wave pairing. **b)** THz plot of the superconductive and normal state optical conductivity of a $Nd_{0.8}Sr_{0.2}NiO_2$ film, as extracted by the Mattis-Bardeen algorithm at 5 K and a Kramers-Kronig constrained fit of the 20 K absolute reflectance, respectively. The grey area highlights the spectral weight difference that is transferred to zero frequency by the Cooper pairs condensation.

nm). As in the β' participates the Nd-4f state, this suggests a multigap nature of the pairing mechanism in $Nd_{0.8}Sr_{0.2}NiO_2$. The discrepancy between the theoretical and the experimental value, however, may come from the ideal bulk material and the absence of the correlations used in the simulation.

6.3 Conclusions

The results reported in this chapter highlight the low-energy electrodynamics of the novel nickelate $Nd_{0.8}Sr_{0.2}NiO_2$ thin film in its normal and superconducting phase. In analogy with most High-T_c cuprates, the normal-state electrodynamics of $Nd_{0.8}Sr_{0.2}NiO_2$ can be described by the Drude model characterized by a scattering time $\tau \sim 1.7 \times 10^{-14}$ s and a plasma frequency $\omega_p \simeq 8500$ cm^{-1} in combination with an Mid-IR absorption band at about $\omega_0 = 4000$ cm^{-1} with an amplitude of $\omega_{pL} = 5000$ cm^{-1}. The $\omega_p^2/(\omega_p^2+\omega_{pL}^2) = 0.74$ ratio can be used to estimate the degree of electronic correlation in $Nd_{0.8}Sr_{0.2}NiO_2$ [297], setting the nickelate infinity layer family in an intermediate level of correlation, well

above the strong correlation values (0.2 - 0.4) corresponding to cuprates[295]. Moreover, the scaling law ($\hbar/\tau \sim 2k_BT_c$) valid for High-T_c cuprates[289] is not satisfied by the $Nd_{0.8}Sr_{0.2}NiO_2$ superconductor ($\hbar/\tau \sim 38.7\, meV \gg 2.2\, meV \sim 2k_BT_c$). This indicates a further difference among charge fluctuations in the CuO_2 and NiO_2 planes. Below T_c, the superconducting gap is extracted from the Terahertz optical data through the Mattis-Bardeen model. The zero temperature vale, $2\Delta \sim 3.2$ meV, is in accordance with tunnelling spectroscopy measurements, suggesting a dirty-limit type-II superconductivity in $Nd_{0.8}Sr_{0.2}NiO_2$, together with the extracted London penetration depth at 5 K of nearly 490 nm.

Conclusions

The aim of this doctoral thesis is to explore the multiple ways in which light can be used to sample the complex dynamics of charge carriers and vibrational lattice modes in quantum materials, with the final goal to understand the relationship among the different degrees of freedom, and the low energy modes emerging from these correlations and/or the topological features of the band structure. In particular, three different spectroscopic techniques have been used: FTIR spectroscopy, performed through a Michaelson interferometre spanning frequencies from THz to Vis, THz time domain spectroscopy, used both to sample the low energy electrodynamics and to induce nonlinear effects by sending THz pulses with a high electric field (up to MV/cm), and optical pump-THz probe, with the use of high fluence optical pulses ranging in wavelength from 2000 to 400 nm. The results shown in this thesis highlight the power of these tools for the characterization of novel quantum materials. In particular, the study of the light-matter interaction at low frequencies (THz and IR) is used to resolve the quantum emergent phenomena that appear in the materials here researched, Co_2MnGa, $MnBi_2Te_4$, CrI_3 and $Nd_{0.8}Sr_{0.2}NiO_2$. The former two, being respectively a topological semimetal and insulator, host a mixed carrier dynamics to which both topological trivial and non-trivial electrons contribute.

For Co_2MnGa (Chapter §3), its study in a thin film geometry with variable thickness highlights an evolution in both the trivial and topological features. In particular, frequency-resolved spectroscopy suggests variable responses both for the intraband and interband excitations, while time-dependent ones expose a subtle electron-lattice correlation, with the formation of polaron quasiparticles, and photocurrents generation, both taking place at a sub-ps scale. The study of the THz emitted by the photocurrents reveals the presence of two microscopic mechanisms of different origin: a photon-drag mechanism of non-topological nature, originating from the bulk of Co_2MnGa and providing a spectral range up to 3 THz, and a surface topological photo-galvanic mechanism mainly responsible for a sub-THz emission. Both the polarons and photocurrents formation give major insights into the photocarriers dynamics in a novel nodal line semimetal like Co_2MnGa, where the study of the low energy dynamics has implications in the development of novel topological-based opto-electronic devices.

The frequency- and temperature-resolved study of the novel intrinsic magnetic topological insulator $MnBi_2Te_4$, in Chapter §4, calls attention to the thickness evolution of the Dirac surface states contributing to the low energy (THz) conductivity. When the

thickness is reduced below 20 nm, the film conductivity appears to be dominated the Dirac electrons of the surface states. This behavior is further proved when crossing the Néel critical temperature at nearly 24 K and entering the magnetically time-reversal broken state. Here, the evolution of the spectral weight suggests the opening of a gap at the Dirac node, of the order of 80 meV, thus underlining the high quality of $MnBi_2Te_4$ thin films as a material hosting the novel magnetic topological insulator phase, whose search is highly longed for due to its anomalous magneto-optical properties and possible implementations as heterostructure layers.

The spectroscopic characterization of layered ferromagnets, like CrI_3 in Chapter §5, reveals many important details about the interplay between different degrees freedom in correlated materials. The study of the optical band-gap evolution with temperature underlines a strong electron-phonon coupling and a stark influence of the magnetic order to the band structure. By studying the far-IR/THz absorption spectrum, several phonon peaks are observed among some magnetic-sensitive peaks that could be the first experimental evidence that these lowest-frequency absorptive terms exhibit strong spin-phonon coupling. Moreover, the study of the IR phonons reveal significant modes softening and line-width changes with varying temperature, suggesting strong anharmonic processes between the lattice vibrations, giving also rise to a broad absorptive term in the optical data. Indeed, these spectroscopic measurements reveal the complex scenario of van der Waals layered magnets, where strong correlations between charge, lattice and magnetic degrees of freedom take place, and elevate these materials as hosting candidates for novel quantum phases and phenomena.

Finally, the optical properties of the high-temperature superconductor $Nd_{0.8}Sr_{0.2}NiO_2$, shown in Chapter §6, highlight a low conductivity and a dirty limit behavior in the normal state, revealing electrodynamical differences between the families of complex materials like nickelates and cuprates. The highly precise relative reflectance measurements further grant an insight into the superconductive phase, from which it is possible to extract the superconductive gap evolution with temperature and the London penetration depth, both in accordance with the most recent results on the same material. Given the thin film constraint (10 nm), it is not possible to shine light on the gap symmetry through the low energy spectroscopic data. However, these results permit to have a solid foundation on the normal state properties and the magnitude of the gap at zero Kelvin.

All the results explored in this thesis point out how the meeting between light and complex matter can open a path toward the discovery and understanding of emergent phases and phenomena. These, together with the possibility of new optical and electronics technological functionalities, contribute to fundamental and general physics yet to be explored from optics and condensed matter.

Part III

Appendix

Appendix A

Berriology

The Berry phase concept is the simplest demonstration of how geometry and topology can emerge from quantum mechanics. It takes its name from a very influential paper by Michael Berry, circulated in 1983 although published in 1984[312]. Berriology is now used as a synonymous for geometry in non-relativistic quantum mechanics. Topological (quantized) invariants are defined via geometrical ones, but many of them (notably the Berry phase) are *purely* geometrical.

The founding concept of geometry is distance. Let $|\psi_1\rangle$ and $|\psi_2\rangle$ be two quantum states in the same Hilbert space: we adopt for their distance an appropriately modified form of the Bures distance[313]:

$$D_{12}^2 = -\ln|\langle\psi_1|\psi_2\rangle|^2$$

The states are defined up to an arbitrary phase factor, and fixing it means a gauge choice. The distance is clearly gauge-invariant and real, while the two states are complex and not separately gauge invariant. The imaginary part meaning of each of the two terms can be written as

$$-\Im\ln\langle\psi_1|\psi_2\rangle = \varphi_{12}, \qquad \varphi_{12} = -\varphi_{21}$$

Besides distance, an additional geometrical concept is needed: the *connection*. This fixes the relative phases between two states in the Hilbert space. The connection is arbitrary and cannot have any physical meaning by itself. Nonetheless, after the 1984 paper by Berry, several physical observables are expressed in terms of the connection and related quantities[314].

A.1 Berry Phase

Suppose to have a general Hamiltonian which depends upon two different kinds of variables $H(x^a;\lambda^i)$. The x^a are the degrees of freedom of the system, meanings the

things that evolve dynamically, the ones that we want to solve in any problem. In contrast, the other variables λ^i are the parameters of the Hamiltonian, which are fixed values determined by some external apparatus. We don't usually exhibit the dependence of H from them. We now place the system in an energy eigenstate $|\psi\rangle$ (the ground state for simplicity) and we assume it to be unique. By varying very slowly the parameters λ, the Hamiltonian changes, and so does the state $|\psi(\lambda(t))\rangle$. However, a theorem in quantum mechanics, known as **adiabatic theorem**, states that, under the considerations done above, the system will cling to that energy eigenstate. This theorem does not consider the possibility of level crossing with varying parameters, indeed these events are rare in quantum mechanics[315].

The idea of the Berry phase arises if we reach again the initial parameters configuration, doing a loop in the Hamiltonian space. Thus the final state must coincide with the initial one, with the only exception of a phase uncertainty

$$|\psi\rangle \to e^{i\gamma}|\psi\rangle$$

We often think of the phase as unphysical, but this is not the case due to the fact that this can be a *phase difference*. For example, we could have started with two states and taken only one of them on this journey while leaving the other unchanged. A subsequent interference between them would highlight the acquired phase. This element will be composed of two contributions: a common dynamical phase $e^{-iEt/\hbar}$, and a geometrical one, which is the mentioned Berry phase.

A.1.1 Construction of the Geometric Phase

The concept of 'geometric phase' made its first appearance in 1956 in a paper written by the young Indian physicist S. Pancharatnam[316], which at the time went largely unnoticed in the Western world. The ideas behind it can be applied with basically no change to the phases of the quantum states of any physical system. The essential feature of Pancharatnam's work is that of considering discrete phase changes, at variance with the more recent works, where continuous phase changes are usually addressed.

The state vectors $|\psi(\lambda(t))\rangle$ are all supposed to reside in the same Hilbert space, meaning that the wave functions are supposed to obey λ-independent boundary conditions. At $t = 0$ we are sure to be in a non-degenerate ground state, and the degeneracy property is maintained at every time. The most natural way of defining a phase difference is

$$e^{-i\Delta\varphi_{12}} = \frac{\langle\psi(\lambda_1)|\psi(\lambda_2)\rangle}{|\langle\psi(\lambda_1)|\psi(\lambda_2)\rangle|}$$

However, in this way $\Delta\varphi_{12}$ will be unphysical, in fact we can always change in an arbitrary way the phase (gauge) of one of the states. This same problem remains between the initial and final state of a discrete path in the Hamiltonian space, and only by closing it into a loop we can make the phase difference to be gauge-invariant, i.e., physical.

Since the phase acquired at every step (with the exception of a gauge change) is characterised by the present and antecedent λ configuration, it seems obvious that the phase at the end of the loop, $\gamma = \Delta\varphi_{12} + \Delta\varphi_{23} + \Delta\varphi_{34} + \Delta\varphi_{41}$, will depend on the chosen path. Moreover, due to the cancellation in pairs of any gauge-arbitrary phase, the overall phase γ will be a gauge-invariant quantity.

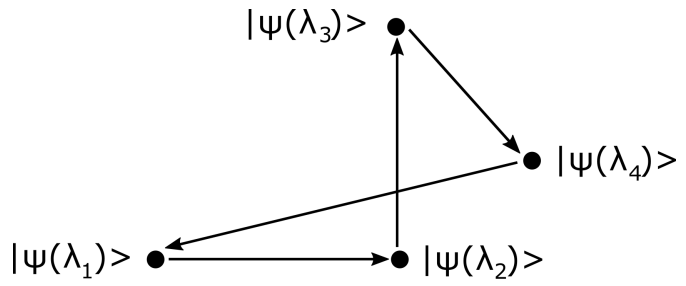

Figure A.1: A closed path joining four states in λ-space.

Switching to a continuous formalism, if we assume that the gauge is chosen such that the phase varies in a *differentiable* way along the path, then we get to leading order in $\Delta\lambda$

$$-i\Delta\varphi \simeq \langle\psi(\lambda)|\nabla_\lambda\psi(\lambda)\rangle \cdot \Delta\lambda$$

with λ a vector of general dimension. In the limiting case of a set of points which becomes dense on the continuous path, the total phase difference γ will converge to a circuit integral:

$$\gamma = \sum_{s=1}^{M} \Delta\varphi_{s,s+1} \to \oint_C d\varphi = i \oint_C \langle\psi(\lambda)|\nabla_\lambda\psi(\lambda)\rangle \cdot d\lambda = -\oint_C \mathcal{A}(\lambda) \cdot d\lambda \qquad \text{(A.1)}$$

where the quantity $\mathcal{A}$, known as *Berry connection*, has been introduced. This is defined up to a gauge transformation, in fact it will depend upon the gauge used to make the phase change differentiable. We could have also used a different general form

$$|\psi'(\lambda)\rangle = e^{i\omega(\lambda)}|\psi(\lambda)\rangle \quad \to \quad \mathcal{A}'(\lambda) = \mathcal{A}(\lambda) + \nabla_\lambda\omega$$

Following the analogy with the gauge theory of electromagnetism, we might expect to find the physical information in the *curvature* of the connection

$$\mathcal{F}_{ij}(\lambda) = \frac{\partial\mathcal{A}_i}{\partial\lambda^j} - \frac{\partial\mathcal{A}_j}{\partial\lambda^i} = -\Im\langle\frac{\partial\psi}{\partial\lambda^i}|\frac{\partial\psi}{\partial\lambda^j}\rangle - (i \leftrightarrow j) \qquad \text{(A.2)}$$

such that from the Stokes theorem

$$\gamma = -\int_S \mathcal{F}_{ij} dS^{ij}$$

where S is a two dimensional surface in the parameter space bounded by the path C. The Berry connection and curvature are also spelled out as *gauge potential* and *gauge field*. One being gauge-dependent and the other gauge-invariant.

The Berry phase will be identified with an observable quantity which *cannot be expressed in terms of any Hermitian operator*. This strangeness is due to the fact that an isolated system cannot show a parametric dependence, hence a Berry phase. Its appearance is the consequence of an underlying interaction of the system with an external environment, and its nature is just a trade-off to highlight some observable effects not included in the initial treatment of the incomplete Hamiltonian[317].

A.1.2 Parallel-Transport Gauge

The main ingredients in Berryology are the $\lambda-$derivatives of the ground state $|\nabla_\lambda \psi_0(\lambda)\rangle$. To lowest order we have

$$|\psi_0(\lambda + \Delta\lambda)\rangle \simeq e^{-i\varphi(\lambda)} \left(|\psi_0(\lambda)\rangle + \sum_{n>0} |\psi_n(\lambda)\rangle \frac{\langle \psi_n | \Delta H | \psi_0 \rangle}{E_0(\lambda) - E_n(\lambda)} \right) \tag{A.3}$$

where $\Delta H = H(\lambda + \Delta\lambda) - H(\lambda)$. The overall phase factor is generally omitted: this corresponds to a specific gauge, called the *parallel-transport gauge*[317]. The name indicates that the first order change in the ground state is chosen to be orthogonal to the state itself. Assuming that $\varphi(\lambda)$ is a differentiable function, the most general Berry connection is

$$\mathcal{A}(\lambda) = i\langle \psi_0(\lambda) | \nabla_\lambda \psi_0 \rangle = \nabla_\lambda \varphi(\lambda)$$

which shows that the arbitrary connection fixes the phase relationship between infinitesimally close state vectors. Thus, within the parallel-transport gauge, the Berry connection is everywhere vanishing. This gauge can be enforced locally at any point λ, but not globally on a closed path C if the Berry phase γ for that path in non-zero.

A.1.3 Chern Number

If we now take a three dimensional parameter space, we can generalize the S surface, which is enclosed in the path to compute the Berry phase, to a closed sphere S^2. If we develop the flux integral of the curvature over this surface, this will remain meaningful, and the key result is that such an integral is quantized. If we divide it by 2π, we would get an integer value called Chern number of first class

$$\mathbb{Z} \ni C_1 = \frac{1}{2\pi} \int_{S^2} \mathcal{F}_{ij} dS^{ij} \tag{A.4}$$

The proof of such a statement is obtained through the Gauss-Bonnet-Chern theorem. This proves the Chern number to be a robust topological invariant of the wavefunction, and is at the origin of observable effects[318].

For the case where the parameter λ is a momentum, as in a periodic crystal, a non vanishing Chern number can only occur in absence of time-reversal symmetry. This is easily seen by the fact that the momentum changes sign, and also does the curvature, making it odd[314]. In the case of reflection symmetry, instead, the condition is for the curvature to be even. If both the symmetries are present, then the curvature is everywhere vanishing, and the Berry phase can be only 0 or π.

A nonzero Chern number can be seen as a failure of Stokes theorem. In fact, the curvature is defined as the curl of the Berry connection, and, since the BZ is a torus without boundaries, a flux integral of the connection would give a zero result. This dilemma is solved by supposing the presence of a singularity (monopole) for the Berry connection inside the BZ. Any Chern number dependent topological property, like Hall conductance, is directly associated to the presence of such a monopole.

Appendix B

Thin films Parameters Extraction

When dealing with the propagation of light across a stack of different materials, like a thin film over substrate, it is useful to treat the light propagation as a plane wave in the Fourier space, which reflection and transmission are defined by the Fresnel relations. If a plane wave, $E(\omega)$, impinges on a thin films over substrate at normal incidence, the transmitted field will be

$$E_T(\omega) = \eta \cdot t_{air,film} \cdot p_{film}(\omega, d) \cdot t_{film,sub} \cdot p_{sub}(\omega, L) \cdot t_{sub,air} \cdot FP(\omega) \cdot E(\omega)$$

where η is the transmission coefficient of free air, d and L are the film and substrate thickness, $t_{a,b} = \frac{2\tilde{n}_a}{\tilde{n}_a+\tilde{n}_b}$ is the transmission coefficient from medium a to medium b, $r_{a,b} = \pm\frac{\tilde{n}_b-\tilde{n}_a}{\tilde{n}_a+\tilde{n}_b}$ is the reflection coefficient (respectively for p and s polarizations), $p_a(\omega, L) = \exp\left[-i\tilde{n}_a\omega L/c\right]$ is the attenuation factor in medium a over distance L, and $FP(\omega)$ describes an etalon dampening inside the material given by the Fabry-Perot multiple reflection at interfaces. Comparing this with a wave traveling the same distance in air, we obtain a transfer function $H(\omega)$ as

$$H(\omega) = \frac{E_T(\omega)}{E_{air}(\omega)} = \frac{2}{\tilde{n}_{film}+1}\frac{2\tilde{n}_{film}}{\tilde{n}_{film}+\tilde{n}_{sub}}\frac{2\tilde{n}_{sub}}{\tilde{n}_{sub}+1}\times$$
$$\times \exp\left[-i(\tilde{n}_{film}-1)\frac{\omega d}{c}\right] \cdot \exp\left[-i(\tilde{n}_{sub}-1)\frac{\omega L}{c}\right] \cdot FP(\omega)$$

The Fabry-Perot terms appear in the transmittance and reflectance measurements as a coherent oscillation as a function of frequency or as an incoherent broadband contribution to the optical response. In most cases these features can be neglected and the $FP(\omega)$ term can be removed from the equation. The film optical indices can thus be extracted once the complete frequency-dependent knowledge of the substrate indices is achieved. This means that an identical substrate to the one used to support the film must be

measured independently. The substrate optical indices extrapolation process is performed through a Kramers-Kronig constrained fit of both the reflectance and transmittance of the bare substrate. Once the substrate optical response is known, it is possible to reproduce the reflectance and transmittance of the entire stack by introducing a model for the film optical response, whose parameters are used as variables for a best fitting procedure.

Indeed, a similar propagation equation can be obtained also for the reflectance geometry. The complex reflectivity ρ of a film over substrate at normal incidence can be calculated explicitly in terms of the frequency-dependent complex Fresnel coefficients $r_{a,b}$ at the mediums interface, and the film thickness d. For a stacking of multiple layers at normal incidence, such as the air/film/substrate trilayer, the reflectivity equation is given by[319,320]

$$\rho = \frac{r_{air,film} + r_{film,sub}\exp(-2i\delta)}{1 + r_{air,film}r_{film,sub}\exp(-2i\delta)} \tag{B.1}$$

where $\delta = 2\pi\tilde{n}_{film}\nu d$ (ν in wavenumbers) and the multiple reflections inside the film are taken into account. The reflection coming from the substrate/air interface is considered negligible. The intensity reflectance can be obtained by taking the absolute value of the complex reflectivity. For the samples studied in this thesis, all the steps required to fit the reflectance and transmittance measurements have been automatized with the aid of the RefFIT software[118].

B.1 Thin Film Approximation

The thin film approximation is a limit where the wavelength and the skin depth are much larger than the thickness of the sample, and the THz field can be regarded as uniform. For materials with a large dielectric constant such as ferroelectrics or metals, the optical thickness ($d_{opt} = n \times d$) could be comparable to the THz wavelength even for nanometric films, and thus classical THz-TDS in transmission can be used to characterise them[49]. The film separates two media, 1 and 2, in which the fields have to satisfy the boundary conditions:

$$\mathbf{n} \times (\mathbf{H}_1 - \mathbf{H}_2) = \int_0^\infty J dz \equiv J_S \; ; \qquad \mathbf{n} \times (\mathbf{E}_1 - \mathbf{E}_2) = 0$$

where $\mathbf{n}$ is the surface normal vector and J_S is the surface current in the thin film. We distinguish s and p polarization, respectively

$$s : \begin{cases} (H_i - H_r)\cos\theta_1 - H_t\cos\theta_2 = J_S \\ E_i + E_r = E_t \end{cases} \qquad p : \begin{cases} H_i + H_r - H_t = J_S \\ (E_i - E_r)\cos\theta_1 - E_t\cos\theta_2 = 0 \end{cases}$$

with i, r and t, symbols for incident, reflected and transmitted light, while θ_1 and θ_2 angles for the reflected and refracted plane wave. The ratio of magnetic and electric fields in the two media is named admittance $Y = \sqrt{\epsilon/\mu}$ ($Y_0 = (377\ \Omega)^{-1}$). From Snell's

law we can write the the condition for a plane-wave electric field as

$$\mathbf{k}_i \cdot r = \mathbf{k}_r \cdot \mathbf{r} = \mathbf{k}_t \cdot \mathbf{r}$$

and the fields as

$$E_i = e^{i\mathbf{k}_i \cdot \mathbf{r}}, \qquad E_r = r_{s/p} e^{i\mathbf{k}_r \cdot \mathbf{r}}, \qquad E_t = t_{s/p} e^{i\mathbf{k}_t \cdot \mathbf{r}}$$

$$H_i = Y_1 e^{i\mathbf{k}_i \cdot \mathbf{r}}, \qquad H_r = Y_1 r_{s/p} e^{i\mathbf{k}_r \cdot \mathbf{r}}, \qquad H_t = Y_2 t_{s/p} e^{i\mathbf{k}_t \cdot \mathbf{r}}$$

Substituting inside the s and p polarization boundary equations, we obtain a form of the coefficients through the effective admittances $Y_\pm = Y_1 \cos\theta_1 \pm Y_2 \cos\theta_2$, such that

$$r_s = \frac{E_r}{E_i} = \frac{Y_- - \sigma_S}{Y_+ + \sigma_S}\ ; \qquad t_s = \frac{E_t}{E_i} = \frac{2Y_1}{Y_+ + \sigma_S} \cos\theta_1$$

$$r_p = \frac{Y_2 \cos\theta_1 - Y_1 \cos\theta_2 + \sigma_S \cos\theta_2}{Y_1 \cos\theta_2 + Y_2 \cos\theta_1 + \sigma_S \cos\theta_2}\ ; \qquad t_p = \frac{2Y_1 \cos\theta_1}{Y_1 \cos\theta_2 + Y_2 \cos\theta_1 + \sigma_S \cos\theta_2}$$

where the current has been written using the conductance σ_S: $J_S = \sigma_S(E_i + E_r)$. These results converge, under $\sigma_S = 0$, to the classical Fresnel relations for an insulating surface.

If we now consider a thin metallic film grown on an insulating substrate, we can write the transfer function for normal incidence as

$$H = \frac{4\tilde{n}_i e^{-i\tilde{n}_i \omega L/c}}{(1+\tilde{n}_i)(1+\tilde{n}_i+\sigma_S Z)} \sum_{k=0}^{\infty} \left\{ \left(\frac{\tilde{n}_i - 1}{\tilde{n}_i + 1} \right) \left(\frac{\tilde{n}_i - 1 - \sigma_S Z}{\tilde{n}_i + 1 + \sigma_S Z} \right) e^{-i2\tilde{n}_i \omega L/c} \right\}^k \tag{B.2}$$

where L and $\tilde{n}_i$ are the insulator thickness and index of refraction, while the sum over k describes a Fabry-Perot contribution. The surface conductivity will be the term of the total matrix associated to the incident electric field direction, thus it will be sensible to polarization variations.

Bibliography

[1] K. v. Klitzing, G. Dorda, and M. Pepper. New Method for High-Accuracy Determination of the Fine-Structure Constant Based on Quantized Hall Resistance. *Physical Review Letters*, **45** (6) : 494-497 (1980)

[2] P. W. Anderson. More Is Different: Broken symmetry and the nature of the hierarchical structure of science. *Science* **177**, 4047 : 393-396 (1972)

[3] D. J. Thouless, M. Kohmoto, M. P. Nightingale, and M. den Nijs. Quantized Hall Conductance in a Two-Dimensional Periodic Potential. *Physical Review Letters*, **49** (6) : 405-408 (1982)

[4] F. D. M. Haldane. Model for a Quantum Hall Effect without Landau Levels: Condensed-Matter Realization of the "Parity Anomaly". *Physical Review Letters*, **61**(18) : 2015-2018 (1988)

[5] A. A. Burkov and L. Balents. Weyl Semimetal in a Topological Insulator Multilayer. *Phys. Rev. Lett.* **107**, 127205 (2011)

[6] N. P. Armitage, E. J. Mele, and A. Vishwanath. Weyl and Dirac semimetals in three-dimensional solids. *Reviews of Modern Physics*, **90**(1) : 1443 (2018)

[7] A. A. Zyuzin and A. A. Burkov. Topological response in Weyl semimetals and the chiral anomaly. *Phys. Rev. B* **86**, 115133 (2012)

[8] A. A. Soluyanov et al. Type-II Weyl semimetals. *Nature*, **527** (7579) : 495-498 (2015)

[9] A. Bansil, H. Lin, and T. Das. Colloquium: Topological band theory. *Rev. Mod. Phys.* **88**, 021004 (2016)

[10] C. Kallin and J. Berlinsky. Chiral superconductors. *Reports on Progress in Physics* **79**, 5 (2016)

[11] G. Jackeli and G. Khaliullin. Mott Insulators in the Strong Spin-Orbit Coupling Limit: From Heisenberg to a Quantum Compass and Kitaev Models. *Phys. Rev. Lett.* **102**, 017205 (2009)

[12] M. Tonouchi. Cutting-edge terahertz technology. *Nature Photonics*, **1** : 97-105 (2007)

[13] C. A. Schmuttenmaer. Exploring Dynamics in the Far-Infrared with Terahertz Spectroscopy. *Chemical Reviews*, **104**(4) : 1759-1780 (2004)

[14] M. Jazbinsek, U. Puc, A. Abina and A. Zidansek. Organic Crystals for THz Photonics. *Appl. Sci.* **9**(5), 882 (2019)

[15] D. J. Cook and R. M. Hochstrasser. Intense terahertz pulses by four-wave rectification in air. *Optics Letters*, **25**(16) : 1210-1212 (2000)

[16] R. B. Laughlin and D. Pines. The Theory of Everything. *PNAS* **97**, 1 (2000)

[17] F. Gebhard. The Mott Metal-Insulator Transition: Models and Methods. Springer Berlin, Heidelberg (2000)

[18] N. Mott. Metal-Insulator Transitions. CRC Press, London (1990)

[19] P. Phillips. Mottness. *Annals of Physics*, **321**, 7 : 1634-1650 (2006)

[20] Y. Tokura, M. Kawasaki, & N. Nagaosa. Emergent functions of quantum materials. *Nature Physics* **13**, 1056–1068 (2017)

[21] B. Keimer, & J. E. Moore. The physics of quantum materials. *Nature Physics* **13**, 1045–1055 (2017)

[22] M. Atiyah. Topological quantum field theories. *Publications Mathématiques de l'Institut des Hautes Études Scientifiques* **68**, 175–186 (1988)

[23] M. Z. Hasan and C. L. Kane. Colloquium: Topological insulators. *Rev. Mod. Phys.* **82**, 4 (2010)

[24] C. Herring. Accidental Degeneracy in the Energy Bands of Crystals. *Physical Review*, **52**(4) : 365-373 (1937)

[25] P. A. M. Dirac. The quantum theory of the electron. *Proceedings of the Royal Society A: Mathematical, Physical and Engineering Sciences*, **117**(778) : 610-624 (1928)

[26] H. Weyl. Gravitation and the Electron. *Proceedings of the National Academy of Sciences of the United States of America*, **15**(4) : 323-334 (1929)

[27] E. Witten. Three lectures on topological phases of matter. *Three Lectrures On Topological Phases of Matter*, arXiv:1510.07698 (2015)

[28] B. A. Bernevig. It's been a Weyl coming. *Nature Physics*, **11**(9) : 698-699 (2015)

[29] J. E. Hirsch. Spin Hall Effect. *Phys. Rev. Lett.* **83**, 1834 (1999)

[30] B. A. Bernevig. *Topological Insulators and Topological Superconductors*. Princeton University Press (2013)

[31] C. L. Kane and E. J. Mele. Quantum Spin Hall Effect in Graphene. *Physical Review Letters.* **95** (22): 226081 (2005)

[32] H. A. Kramers. Théorie générale de la rotation paramagnétique dans les cristaux. Proceedings of the Royal Netherlands Academy of Arts and Sciences **33** (6–10): 959-972 (1930)

[33] M. König et al. Quantum Spin Hall Insulator State in HgTe Quantum Wells. *Science* **318**, 5851 : 766-770 (2007)

[34] L. Fu, C. L. Kane and E. J. Mele. Topological insulators in three dimensions. *Physical Review Letters.* **98** (10): 106803 (2007)

[35] L. Fu and C. L. Kane. Topological insulators with inversion symmetry. *Physical Review B.* **76** (4): 045302 (2007)

[36] D. Hsieh. A Topological Dirac insulator in a quantum spin Hall phase. *Nature* **452** (9): 970–4 (2008)

[37] D. Hsieh et al. A tunable topological insulator in the spin helical Dirac transport regime. *Nature* **460**, 1101–1105 (2009)

[38] X.-L. Qi and S.-C. Zhang. Topological insulators and superconductors. *Rev. Mod. Phys.* **83**, 1057 (2011)

[39] R. Yu et al. Quantized Anomalous Hall Effect in Magnetic Topological Insulators. *Science* **329**, 5987 : 61-64 (2010)

[40] X.-L. Qi, T. L. Hughes, and S.-C. Zhang. Topological field theory of time-reversal invariant insulators. *Phys. Rev. B* **78**, 195424 (2008)

[41] Y. Tokura, K. Yasuda, & A. Tsukazaki. Magnetic topological insulators. *Nature Reviews Physics* **1**, 126-143 (2019)

[42] J. Teng, N. Liu, & Y. Li. Mn-doped topological insulators: a review. *J. Semicond.* **40**, 081507 (2019)

[43] T. Hesjedal. Rare Earth Doping of Topological Insulators: A Brief Review of Thin Film and Heterostructure Systems. *Phys. Status Solidi A* **216**, 1800726 (2019)

[44] Yi Zhou, K. Kanoda, and T.-K. Ng. Quantum spin liquid states. *Rev. Mod. Phys.* **89**, 025003 (2017)

[45] L. Savary and L. Balents. Quantum spin liquids: a review. *Rep. Prog. Phys.* **80** 016502 (2016)

[46] A. Kitaev. Anyons in an exactly solved model and beyond. *Annals of Physics* **321**, 1 : 2-111 (2006)

[47] X. G. Wen. Effective Lagrangian for holes in the spin-liquid state. *Phys. Rev. B* **39**, 7223 (1989)

[48] X. G. Wen. Mean-field theory of spin-liquid states with finite energy gap and topological orders. *Phys. Rev. B* **44**, 2664 (1991)

[49] M. Perenzoni and D. J. Paul. *Physics and Applications of Terahertz Radiation*, Springer Series in Optical Sciences **173** (2004)

[50] S. L. Dexheimer. *Terahertz Spectroscopy: Principles and Applications*, CRC Press (2008)

[51] X. C. Zhang and J. Xu. *Introduction to THz Wave Photonics*, Springer (2010)

[52] P. Drude. Zur Elektronentheorie der Metalle. *Annalen der Physik* **306**(3): 566–613 (1900)

[53] L. Rosenfeld. *Theory of Electrons*. New York: Dover Publications, pp. 68 (1965)

[54] A. Bera et al. Review of recent progress on THz spectroscopy of quantum materials: superconductors, magnetic and topological materials. *The European Physical Journal Special Topics* **230**, pp. 4113–4139 (2021)

[55] E. Nichelatti. Complex refractive index of a slab from reflectance and transmittance: Analytical solution. *J. Opt. A Pure Appl. Opt.* **4**, 300–403 (2002)

[56] M. Dressel and G. Grüner. *Electrodynamics of solids*, Cambridge University Press (2002)

[57] B. S. Williams. Terahertz quantum-cascade lasers. *Nature Photonics* **1**, pp. 517–525 (2007)

[58] M. Hangyo, T. Nagashima and S. Nashima. Spectroscopy by pulsed terahertz radiation. *Measurement Science and Technology* **13**, 11 (2002)

[59] D. Dragoman & M. Dragoman. Terahertz fields and applications. *Progress in Quantum Electronics* **28**, 1, pp. 1-66 (2004)

[60] C.-K. Sun, F. Vallée, L. Acioli, E. P. Ippen, and J. G. Fujimoto. Femtosecond investigation of electron thermalization in gold. *Phys. Rev. B* **48**, 12365(R) (1993)

[61] D. N. Basov, R. D. Averitt, D. van der Marel, M. Dressel, and K. Haule. Electrodynamics of correlated electron materials. *Rev. Mod. Phys.* **83**, 471 (2011)

[62] E. Dagotto. Correlated electrons in high-temperature superconductors. *Rev. Mod. Phys.* **66**, 763 (1994)

[63] Y. He, Y. Chen, L. Zhang, S.-W. Wong and Z. Ning Chen. An overview of terahertz antennas. *China Communications* **17**, 7 (2020)

[64] N. M. Burford, M. O. El-Shenawee. Review of terahertz photoconductive antenna technology. *Optical Engineering* **56**(1), 010901 (2017)

[65] A. Schneider, M. Neis, M. Stillhart, B. Ruiz, R. U. A. Khan, and P. Günter. Generation of terahertz pulses through optical rectification in organic DAST crystals: theory and experiment. *Journal of the Optical Society of America B* **23**, 9, pp. 1822-1835 (2006)

[66] A. D´Arco et al. Broadband Anisotropic Optical Properties of the Terahertz Generator HMQ-TMS Organic Crystal. *Condens. Matter* **5**(3), 47 (2020)

[67] M. D. Thomson, V. Blank, and H. G. Roskos. Terahertz white-light pulses from an air plasma photo-induced by incommensurate two-color optical fields. *Optics Express* **18**, 22, pp. 23173-23182 (2010)

[68] J. Dai, J. Liu and X.-C. Zhang. Terahertz Wave Air Photonics: Terahertz Wave Generation and Detection With Laser-Induced Gas Plasma. *IEEE Journal of Selected Topics in Quantum Electronics* **17**, 1 (2011)

[69] R. Boyd. *Nonlinear Optics*. Elsevier Academic Press (2008)

[70] A. D'Arco et al. Broadband Anisotropic Optical Properties of the Terahertz Generator HMQ-TMS Organic Crystal. *Condensed Matter* **5** (3), 47 (2020)

[71] A. Schneider. Theory of terahertz pulse generation through optical rectification in a nonlinear optical material with a finite size. *Phys. Rev. A* **82**, 033825 (2010)

[72] Y. Shen et al. Nonlinear Cross-Phase Modulation with Intense Single-Cycle Terahertz Pulses. *Physical Review Letters* **99** : 043901 (2007)

[73] N. Nagaosa, J. Sinova, S. Onoda, A. H. MacDonald, and N. P. Ong. Anomalous Hall effect. *Rev. Mod. Phys.* **82**, 1539 (2010)

[74] C.-Z. Chang et al. Experimental Observation of the Quantum Anomalous Hall Effect in a Magnetic Topological Insulator. *Science* **340**, 6129, pp. 167-170 (2013)

[75] E. Liu et al. Giant anomalous Hall effect in a ferromagnetic kagome-lattice semimetal. *Nature Physics* **14**, pp. 1125–1131 (2018)

[76] R. S. K. Mong, A. M. Essin, and J. E. Moore. Antiferromagnetic topological insulators. *Phys. Rev. B* **81**, 245209 (2010)

[77] T. Morimoto and N. Nagaosa. Topological nature of nonlinear optical effects in solids. *Science Advances* **2**(5) : e1501524 (2016)

[78] T. Morimoto, S. Zhong, J. Orenstein, and J. E. Moore. Semiclassical theory of nonlinear magneto-optical responses with applications to topological Dirac/Weyl semimetals. *Physical Review B*, **94**(24) (2016)

[79] F. Giorgianni et al. Strong nonlinear terahertz response induced by Dirac surface states in Bi_2Se_3 topological insulator. *Nature Communications*, **7** : 11421 (2016)

[80] C.-K. Chan, N. H. Lindner, G. Refael, and P. A. Lee. Photocurrents in Weyl semimetals. *Physical Review B* **95**, 041104(R) (2017)

[81] F. de Juan, A. G. Grushin, T. Morimoto & J. E Moore. Quantized circular photogalvanic effect in Weyl semimetals. *Nature Communications* **8**, 15995 (2017)

[82] F. Ortmann, S. Roche, S. O. Valenzuela. *Topological Insulators: Fundamentals and Perspectives*. Wiley-VCH Verlag GmbH & Co. KGaA (2015)

[83] Y. Araki. Magnetic Textures and Dynamics in Magnetic Weyl Semimetals. *Ann. Phys.* **532**(2), 1900287 (2019)

[84] D. Destraz et al. Magnetism and anomalous transport in the Weyl semimetal PrAlGe: possible route to axial gauge fields. *npj Quantum Materials* **5**, 5 (2020)

[85] D. F. Liu et al. Magnetic Weyl semimetal phase in a Kagomé crystal, *Science* **365**, 1282–1285 (2019)

[86] S. Finizio et al. Magnetic configurations in nanostructured Co_2MnGa thin film elements. *New J. Phys.* **17**, 083030 (2015)

[87] Z. Zhu, T. Higo, S. Nakatsuji and Y. Otani. Magnetic and transport properties of amorphous, B2 and L21 Co_2MnGa thin films. *AIP Advances* **10**, 085020 (2020)

[88] J.-W. Rhim and Y. Baek Kim. Anisotropic density fluctuations, plasmons, and Friedel oscillations in nodal line semimetal. *New J. Phys.* **18**, 043010 (2016)

[89] G. Chang et al. Topological Hopf and Chain Link Semimetal States and Their Application to Co_2MnGa. *Phys. Rev. Lett.* **119**, 156401 (2017)

[90] I. Belopolski et al. Discovery of topological Weyl fermion lines and drumhead surface states in a room temperature magnet. *Science* **365**, 6459, 1278-1281 (2019)

[91] C. Fang, H. Weng, Xi Dai and Z. Fang. Topological nodal line semimetals. *Chinese Phys. B* **25**, 117106 (2016)

[92] T. Tai and C. Hua Lee. Anisotropic non-linear optical response of nodal loop materials. *Phys. Rev. B* **103**, 195125 (2021)

[93] S. Ahn, E.J. Mele, and H. Min. Electrodynamics on Fermi Cyclides in Nodal Line Semimetals. *Phys. Rev. Lett.* **119**, 147402 (2017)

[94] J. P. Carbotte. Optical response of a line node semimetal. *J. Phys.: Condens. Matter* **29**, 045301 (2017)

[95] Y. Kurtulus, R. Dronskowski, G. D. Samolyuk, and V. P. Antropov. Electronic structure and magnetic exchange coupling in ferromagnetic full Heusler alloys. *Phys. Rev. B* **71**, 014425 (2005)

[96] K. Manna et al. From Colossal to Zero: Controlling the Anomalous Hall Effect in Magnetic Heusler Compounds via Berry Curvature Design. *Phys. Rev. X* **8**, 041045 (2018)

[97] R. A. Faregh, A. Boochani, S. R. Masharian & F. H. Jafarpour. The surface effect on the thermodynamic stability, half-metallic and optical properties of Co_2MnGa(001) films: a DFT study. *International Nano Letters* **9**, 339–348 (2019)

[98] J. Y. Rhee, Y. V. Kudryavtsev, K. W. Kim and Y. P. Lee. Peculiar Optical Properties of Co_2MnGa Alloys. *ASEAN Journal on Science & Technology for Development* **24**, 1&2 (2007)

[99] P. Swekis et al. Magnetic and Electronic Properties of Weyl Semimetal Co_2MnGa Thin Films. *Nanomaterials* **11**(1), 251 (2021)

[100] C. H. Lee et al. Enhanced higher harmonic generation from nodal topology. *Phys. Rev. B* **102**, 035138 (2020)

[101] A. Markou et al. Thickness dependence of the anomalous Hall effect in thin films of the topological semimetal Co_2MnGa. *Phys. Rev. B* **100**, 054422 (2019)

[102] H. Reichlova et al. Large anomalous Nernst effect in thin films of the Weyl semimetal Co_2MnGa. *Appl. Phys. Lett.* **113**, 212405 (2018)

[103] A. Sakai et al. Giant anomalous Nernst effect and quantum-critical scaling in a ferromagnetic semimetal. *Nature Physics* **14**, 1119–1124 (2018)

[104] X. Han et al. Giant intrinsic anomalous terahertz Faraday rotation in the magnetic Weyl semimetal Co_2MnGa at room temperature. *Phys. Rev. B* **105**, 174406 (2022)

[105] C. Zhu et al. A robust and tuneable mid-infrared optical switch enabled by bulk Dirac fermions. *Nature Communications* **8**, 14111 (2017)

[106] W. Lu et al. Relaxation dynamics of photoexcited Dirac fermions in the three-dimensional Dirac semimetal Cd_3As_2. *Phys. Rev. B* **95**, 024303 (2017)

[107] W. Zhang et al. Ultrafast photocarrier dynamics in a 3D Dirac semimetal Cd_3As_2 film studied with terahertz spectroscopy. *Appl. Phys. Lett.* **114**, 221102 (2019)

[108] W. Lu, J. Ling, F. Xiu, and D. Sun. Terahertz probe of photoexcited carrier dynamics in the Dirac semimetal Cd_3As_2. *Phys. Rev. B* **98**, 104310 (2018)

[109] Z. Dai et al. High Mobility 3D Dirac Semimetal (Cd_3As_2) for Ultrafast Photoactive Terahertz Photonics. *Advanced Functionals Materials* **31**, 17, 2011011 (2021)

[110] K. J. Tielrooij et al. Photoexcitation cascade and multiple hot-carrier generation in graphene. *Nature Physics* **9**, 248–252 (2013)

[111] G. Jnawali, Yi Rao, H. Yan, and T. F. Heinz. Observation of a Transient Decrease in Terahertz Conductivity of Single-Layer Graphene Induced by Ultrafast Optical Excitation. *Nano Lett.* **13**, 2, 524–530 (2013)

[112] N. Sirica et al. Tracking Ultrafast Photocurrents in the Weyl Semimetal TaAs Using THz Emission Spectroscopy. *Phys. Rev. Lett.* **122**, 197401 (2019)

[113] Kai Sun et al. Circular Photogalvanic Effect in the Weyl Semimetal TaAs. *CHIN. PHYS. LETT.* **34**, 11: 117203 (2017)

[114] Y. Gao et al. Chiral terahertz wave emission from the Weyl semimetal TaAs. *Nature Communications* **11**, 720 (2020)

[115] M. Tong et al. Helicity-dependent THz emission induced by ultrafast spin photocurrent in nodal-line semimetal candidate Mg_3Bi_2. *Opto-Electron Adv* **3**, 200023 (2020)

[116] S. Y. Hamh et al. Anisotropic Terahertz Emission from Bi_2Se_3 Thin Films with Inclined Crystal Planes. *Nanoscale Research Letters* **10**, 489 (2015)

[117] Li-Guo Zhu, B. Kubera, K. F. Mak & J. Shan. Effect of Surface States on Terahertz Emission from the Bi_2Se_3 Surface. *Scientific Reports* **5**, 10308 (2015)

[118] A. B. Kuzmenko. Kramers–Kronig constrained variational analysis of optical spectra. *Review of Scientific Instruments* **76**, 083108 (2005)

[119] A. T. Zayak, P. Entel, K. M. Rabe, W. A. Adeagbo, and M. Acet. Anomalous vibrational effects in nonmagnetic and magnetic Heusler alloys. *Phys. Rev. B* **72**, 054113 (2005)

[120] Z. Zhang et al. Ultrafast electron-phonon coupling and photo-induced strain in the morphotropic phase boundary of $Bi_xDy_{1-x}FeO_3$ films. *Scientific Reports* **8**, 3258 (2018)

[121] P. A. George et al. Ultrafast Optical-Pump Terahertz-Probe Spectroscopy of the Carrier Relaxation and Recombination Dynamics in Epitaxial Graphene. *Nano Letters* **8**, 12, pp. 4248-4251 (2008)

[122] S. Kar, D. R. Mohapatra, E. Freysz and A. K. Sood. Tuning photoinduced terahertz conductivity in monolayer graphene: Optical-pump terahertz-probe spectroscopy. *Physical Review B* **90**, 165420 (2014)

[123] P. Suo et al. Observation of Negative Terahertz Photoconductivity in Large Area Type-II Dirac Semimetal $PtTe_2$. *Physical Review Letters* **126**, 227402 (2021)

[124] C. H. Lui et al. Trion-Induced Negative Photoconductivity in Monolayer MoS_2. *Physical Review Letters* **113**, 166801 (2014)

[125] E. Cinquanta et al. Ultrafast THz Probe of Photoinduced Polarons in Lead-Halide Perovskites. *Physical Review Letters* **122**, 166601 (2019)

[126] S. A. Bretschneider et al. Quantifying Polaron Formation and Charge Carrier Cooling in Lead-Iodide Perovskites. *Adv. Mater.* 30,29 (2008)

[127] K. H. Wu et al. Ultrafast optical probes of polaron dynamics in $La_{0.7}Ca_{0.3}MnO_3$ thin films. *Journal of Applied Physics* **105**, 043901 (2009)

[128] H. Fröhlich, H. Pelzer & S. Zienau. Properties of slow electrons in polar materials. *The London, Edinburgh, and Dublin Philosophical Magazine and Journal of Science* **41**, 314, pp. 221-242 (1950)

[129] H. Fröhlich. Electrons in lattice fields. *Advances in Physics* **3**, 11, pp. 325-361 (1954)

[130] J. T. Devreese and A. S. Alexandrov. Fröhlich polaron and bipolaron: recent developments. *Rep. Prog. Phys.* **72**, 066501 (2009)

[131] B. Guzelturk et al. Visualization of dynamic polaronic strain fields in hybrid lead halide perovskites. *Nature Materials* **20**, 618–623 (2021)

[132] J. Wang et al. Effect of epitaxial strain on small-polaron hopping conduction in $Pr_{0.7}(Ca_{0.6}Sr_{0.4})_{0.3}MnO_3$ thin films. *Applied Physics Letters* **106**, 102406 (2015)

[133] M. Zhukova et al. Experimental study of THz electro-optical sampling crystals ZnSe, ZnTe and GaP. *Journal of Physics: Conference Series* **917**, 6 (2017)

[134] J. E. Goff and W. L. Schaich. Theory of the photon-drag effect in simple metals. *Phys. Rev. B* **61**, 10471 (2000)

[135] V. A. Shalygin et al. Circular photon drag effect in bulk semiconductors. *J. Phys.: Conf. Ser.* **864**, 012072 (2017)

[136] G. M. Mikheev, A. S. Saushin, V. M. Styapshin & Yu. P. Svirko. Interplay of the photon drag and the surface photogalvanic effects in the metal-semiconductor nanocomposite. *Scientific Reports* **8**, 8644 (2018)

[137] J. Maysonnave et al. Terahertz Generation by Dynamical Photon Drag Effect in Graphene Excited by Femtosecond Optical Pulses. *Nano Lett.* **14**, 10, pp. 5797–5802 (2014)

[138] J. B. Héroux, Y. Ino, and M. Kuwata-Gonokam. Terahertz radiation emission from GaMnAs. *Appl. Phys. Lett.* **88**, 221110 (2006)

[139] L. Kronik & Y. Shapira. Surface photovoltage phenomena: theory, experiment, and applications. *Surface Science Reports* **37**, 1–5, pp. 1-206 (1999)

[140] V. Apostolopoulos and M. E. Barnes. THz emitters based on the photo-Dember effect. *Journal of Physics D: Applied Physics* **47**, 37 (2014)

[141] J. B. Khurgin. Optical rectification and terahertz emission in semiconductors excited above the band gap. *Journal of the Optical Society of America B* **11**, 12, pp. 2492-2501 (1994)

[142] J.-Q. Yan et al. Crystal growth and magnetic structure of $MnBi_2Te_4$. *Phys. Rev. Materials* **3**, 064202 (2019)

[143] L. Ding, C. Hu, F. Ye, E. Feng, Ni Ni, and H. Cao. Crystal and magnetic structures of magnetic topological insulators $MnBi_2Te_4$ and $MnBi_4Te_7$. *Phys. Rev. B* **101**, 020412(R) (2020)

[144] J. F. Dillon Jr., H. Kamimura, & J. P. Remeika. Magneto-optical properties of ferromagnetic chromium trihalides. *Journal of Physics and Chemistry of Solid* **27**, 9, 1531-1549 (1966)

[145] Yu Liu et al. Thickness-dependent magnetic order in CrI_3 single crystals. *Scientific Reports* **9**, 13599 (2019)

[146] L. Tomarchio et al. Low Energy Electrodynamics of CrI_3 Layered Ferromagnet. *Scientific Reports* **11**, 23405 (2021)

[147] C. Hu et al. A van der Waals antiferromagnetic topological insulator with weak interlayer magnetic coupling. *Nature Communications* **11**, 97 (2020)

[148] D. A. Estyunin et al. Signatures of temperature driven antiferromagnetic transition in the electronic structure of topological insulator $MnBi_2Te_4$. *APL Materials* **8**, 021105 (2020)

[149] H. Li et al. Antiferromagnetic topological insulator $MnBi_2Te_4$: synthesis and magnetic properties. *Phys. Chem. Chem. Phys.* **22**, 556-563 (2020)

[150] B. Li et al. Competing Magnetic Interactions in the Antiferromagnetic Topological Insulator $MnBi_2Te_4$. *Phys. Rev. Lett.* **124**, 167204 (2020)

[151] Y. Deng et al. Quantum anomalous Hall effect in intrinsic magnetic topological insulator $MnBi_2Te_4$. *Science* **367**, 6480, pp. 895-900 (2020)

[152] J. Li et al. Intrinsic magnetic topological insulators in van der Waals layered $MnBi_2Te_4$-family materials. *Science Advances* **5**, 6 (2019)

[153] Y.-J. Hao et al. Gapless Surface Dirac Cone in Antiferromagnetic Topological Insulator $MnBi_2Te_4$. *Phys. Rev. X* **9**, 041038 (2019)

[154] R. C. Vidal et al. Surface states and Rashba-type spin polarization in antiferromagnetic $MnBi_2Te_4(0001)$. *Phys. Rev. B* **100**, 121104(R) (2019)

[155] Y. Gong et al. Experimental Realization of an Intrinsic Magnetic Topological Insulator. *Chinese Physics Letters* **36**, 7 (2019)

[156] C. Liu et al. Robust axion insulator and Chern insulator phases in a two-dimensional antiferromagnetic topological insulator. *Nature Materials* **19**, 522–527 (2020)

[157] P. Di Pietro et al. Optical conductivity of bismuth-based topological insulators. *Physical Review B* **86**, 045439 (2012)

[158] P. Di Pietro et al. Observation of Dirac plasmons in a topological insulator. *Nature Nanotech.* **8**, 556 (2013)

[159] M. Autore et al. Topologically protected Dirac plasmons and their evolution across the quantum phase transition in a $(Bi1-xIn_x)_2Se_3$ topological insulator. *Nanoscale* **8**, 4667 (2016)

[160] M. Autore et al. Plasmon–Phonon Interactions in Topological Insulator Microrings. *Advanced Optical Mat.* **3**, 1257 (2015)

[161] F. Giorgianni et al. Strong nonlinear terahertz response induced by Dirac surface states in Bi2Se3 topological insulator. *Nature Commun.* **7**, 11421 (2016)

[162] A. M. Shikin et al. Nature of the Dirac gap modulation and surface magnetic interaction in axion antiferromagnetic topological insulator $MnBi_2Te_4$. *Scientific Reports* **10**, 13226 (2020)

[163] B. Chen et al. Intrinsic magnetic topological insulator phases in the Sb doped $MnBi_2Te_4$ bulks and thin flakes. *Nature Communications* **10**, 4469 (2019)

[164] M. Köpf, J. Ebad-Allah, S. H. Lee, Z. Q. Mao & C. A. Kuntscher. Influence of magnetic ordering on the optical response of the antiferromagnetic topological insulator $MnBi_2Te_4$. *Phys. Rev. B* **102**, 165139 (2020)

[165] M. Sang, J. Shin, K. Kim & K. J. Yu. Electronic and Thermal Properties of Graphene and Recent Advances in Graphene Based Electronics Applications. *Nanomaterials (Basel)* **9**(3): 374 (2019)

[166] K. F. Mak, et al. Measurement of the Optical Conductivity of Graphene. *Physical Review Letters* **101**, 196405 (2008)

[167] V. V. Chistyakov et al. Thickness dependence of conductivity in Bi_2Se_3 topological insulator. *J. Phys.: Conf. Ser.* **1389**, 012051 (2019)

[168] L. Wu et al. High-Resolution Faraday Rotation and Electron-Phonon Coupling in Surface States of the Bulk-Insulating Topological Insulator $Cu_{0.02}Bi_2Se_3$. *Phys. Rev. Lett.* **115**, 217602 (2015)

[169] C. X. Trang et al. Crossover from 2D Ferromagnetic Insulator to Wide Band Gap Quantum Anomalous Hall Insulator in Ultrathin $MnBi_2Te_4$. *ACS Nano* **15**, 8, 13444–13452 (2021)

[170] H.-R. Ji et al. Detection of Magnetic Gap in Topological Surface States of $MnBi_2Te_4$. *Chinese Physics Letters* **38**, 10 (2021)

[171] L. Xu et al. Persistent surface states with diminishing gap in $MnBi_2Te_4/Bi_2Te_3$ superlattice antiferromagnetic topological insulator. *Science Bulletin* **65**, 24 2086-2093 (2020)

[172] I. I. Klimovskikh et al. Tunable 3D/2D magnetism in the $(MnBi_2Te_4)(Bi_2Te_3)_m$ topological insulators family. *npj Quantum Materials* **5**, 54 (2020)

[173] L. J. Sandilands, Y. Tian, K. W. Plumb, Y.-J. Kim & K. S. Burch. Scattering Continuum and Possible Fractionalized Excitations in α-$RuCl_3$. *Phys. Rev. Lett.* **114**, 147201 (2015)

[174] S. Reschke et al. Sub-gap optical response in the Kitaev spin-liquid candidate α-$RuCl_3$. *J. Phys.: Condens. Matter* **30** 475604 (2018)

[175] A. Little et al. Antiferromagnetic Resonance and Terahertz Continuum in α-$RuCl_3$. *Phys. Rev. Lett.* **119**, 227201 (2017)

[176] Q. H. Wang, K. Kalantar-Zadeh, A. Kis, J. N. Coleman & M. S. Strano. Electronics and optoelectronics of two-dimensional transition metal dichalcogenides. *Nature Nanotechnology* **7**, pp. 699–712 (2012)

[177] S. Manzeli, D. Ovchinnikov, D. Pasquier, O. V. Yazyev & A. Kis. 2D transition metal dichalcogenides. *Nature Reviews Materials* **2**, 17033 (2017)

[178] J. Reedijk & K. Poeppelmeier. Comprehensive Inorganic Chemistry II: From Elements to Applications, Elsevier (2013)

[179] C. W. Liu, M. Östling & J. B. Hannon. New materials for post-Si computing. *MRS Bulletin* **39**, 658–662 (2014)

[180] M. C.Lemme, L.-J. Li, T. Palacios & F. Schwierz. Two-dimensional materials for electronic applications. *MRS Bulletin* **39**, 711–718 (2014)

[181] B. Radisavljevic, A. Radenovic, J. Brivio, V. Giacometti & A. Kis. Single-layer MoS_2 transistors. *Nature Nanotechnology* **6**, 147–150 (2011)

[182] K. F. Mak & J. Shan. Photonics and optoelectronics of 2D semiconductor transition metal dichalcogenides. *Nature Photonics* **10**, 216–226 (2016)

[183] C. Felser, G. H. Fecher & B. Balke. Spintronics: A Challenge for Materials Science and Solid-State Chemistry. *Angewandte Chemie* **46**, 5, 668-699 (2007)

[184] J. R. Schaibley et al. Valleytronics in 2D materials. *Nature Reviews Materials* **1**, 16055 (2016)

[185] H. Wang, V. Eyert & U. Schwingenschlögl. Electronic structure and magnetic ordering of the semiconducting chromium trihalides $CrCl_3$, $CrBr_3$, and CrI_3. *J. Phys.: Condens. Matter* **23**, 116003 (2011)

[186] B. Niu et al. Coexistence of Magnetic Orders in Two-Dimensional Magnet CrI_3. *Nano Lett.* **20**, 1, 553–558 (2020)

[187] I. Pollini. Electron correlations and hybridization in chromium compounds. *Solid State Communications* **106**, 8, 549-554 (1998)

[188] V. M. Bermudez & D. S. McClure. Spectroscopic studies of the two-dimensional magnetic insulators chromium trichloride and chromium tribromide—I. *Journal of Physics and Chemistry of Solids* **40**, 2, 129-147 (1979)

[189] W. Jin et al. Observation of the polaronic character of excitons in a two-dimensional semiconducting magnet CrI_3. *Nature Communications* **11**, 4780 (2020)

[190] J. Knolle, D. L. Kovrizhin, J. T. Chalker & R. Moessner. Dynamics of a Two-Dimensional Quantum Spin Liquid: Signatures of Emergent Majorana Fermions and Fluxes. *Phys. Rev. Lett.* **112**, 207203 (2014)

[191] P. S. Pershan. Magneto-Optical Effects. *Journal of Applied Physics* **38**, 1482 (1967)

[192] M. Freiser. A survey of magnetooptic effects. *IEEE Transactions on Magnetics* **4**, 2 (1968)

[193] T. Haider. A Review of Magneto-Optic Effects and Its Application. *International Journal of Electromagnetics and Applications* **7**, 1, 17-24 (2017)

[194] W. Zhao et al. Magnetic proximity and nonreciprocal current switching in a monolayer WTe_2 helical edge. *Nature Materials* **19**, 503–507 (2020)

[195] D. Zhong et al. Van der Waals engineering of ferromagnetic semiconductor heterostructures for spin and valleytronics. *Science Advances* **3**, 5 (2017)

[196] K. L. Seyler et al. Ligand-field helical luminescence in a 2D ferromagnetic insulator. *Nature Physics* **14**, 277–281 (2018)

[197] Z. Liu et al. Observation of nonreciprocal magnetophonon effect in nonencapsulated few-layered CrI_3. *Science Advances* **6**, 43, eabc7628 (2020)

[198] B. Huang et al. Layer-dependent ferromagnetism in a van der Waals crystal down to the monolayer limit. *Nature* **546**, 270–273 (2017)

[199] V. K. Gudelli & G.-Y. Guo. Magnetism and magneto-optical effects in bulk and few-layer CrI_3: a theoretical GGA + U study. *New Journal of Physics* **21**, 053012 (2019)

[200] M. A.McGuire, H. Dixit, V. R. Cooper & B. C. Sales. Coupling of Crystal Structure and Magnetism in the Layered, Ferromagnetic Insulator CrI_3. *Chem. Mater.* **27**, 2, 612–620 (2015)

[201] L. Webster, L. Liang & J.-A. Yan. Distinct spin–lattice and spin–phonon interactions in monolayer magnetic CrI_3. *Phys. Chem. Chem. Phys.* **20**, 23546-23555 (2018)

[202] Y. Zhang et al. Switchable magnetic bulk photovoltaic effect in the two-dimensional magnet CrI_3. *Nature Communications* **10**, 3783 (2019)

[203] C. Bacaksiz, D. Šabani, R. M. Menezes & M. V. Milošević. Distinctive magnetic properties of CrI_3 and $CrBr_3$ monolayers caused by spin-orbit coupling. *Phys. Rev. B* **103**, 125418 (2021)

[204] L. Chen et al. Magnetic anisotropy in ferromagnetic CrI_3. *Physical Review B* **101**, 134418 (2020)

[205] P. P. Stavropoulos, X. Liu & H.-Y. Kee. Magnetic anisotropy in spin-3/2 with heavy ligand in honeycomb Mott insulators: Application to CrI_3. *Physical Review Research* **3**, 013216 (2021)

[206] Z. Sun et al. Giant nonreciprocal second-harmonic generation from antiferromagnetic bilayer CrI_3. *Nature* **572**, 497–501 (2019)

[207] A. A. Pervishko et al. Localized surface electromagnetic waves in CrI_3-based magnetophotonic structures. *Optics Express* **28**, 20, 29155-29165 (2020)

[208] J. Nasu, J. Knolle, D. L. Kovrizhin, Y. Motome & R. Moessner. Fermionic response from fractionalization in an insulating two-dimensional magnet. *Nature Physics* **12**, 912–915 (2016)

[209] Z. Wang et al. Magnetic Excitations and Continuum of a Possibly Field-Induced Quantum Spin Liquid in α-$RuCl_3$. *Phys. Rev. Lett.* **119**, 227202 (2017)

[210] L. Chen et al. Topological Spin Excitations in Honeycomb Ferromagnet CrI_3. *Phys. Rev. X* **8**, 041028 (2018)

[211] A. T. Costa, D. L. R. Santos, N. M. R. Peres & J. Fernandez-Rossier. Topological magnons in CrI_3 monolayers: an itinerant fermion description. *2D Mater.* **7**, 045031 (2020)

[212] M. Freda et al. Transmittance Fourier Transform Infrared Spectra of Liquid Water in the Whole Mid-Infrared Region: Temperature Dependence and Structural Analysis. *Applied Spectroscopy* **59**, 9, 1155-1159 (2005)

[213] Y. Jung, Y. Zhou & J. J. Cha. Intercalation in two-dimensional transition metal chalcogenides. *Inorg. Chem. Front.* **3**, 452-463 (2016)

[214] N. Ghobadi. Band gap determination using absorption spectrum fitting procedure. *International Nano Letters* **3**, 2 (2013)

[215] A. Manoogian & J. C. Woolley. Temperature dependence of the energy gap in semiconductors. *Canadian Journal of Physics* **62**, 3 (1984)

[216] B. V. Van Zeghbroeck. Principles of semiconductor devices and heterojunctions. Upper Saddle River, Pearson Education (2010)

[217] J. Bhosale et al. Temperature dependence of band gaps in semiconductors: Electron-phonon interaction. *Phys. Rev. B* **86**, 195208 (2012)

[218] Y. Liu & C. Petrovic. Three-dimensional magnetic critical behavior in CrI_3. *Phys. Rev. B* **97**, 014420 (2018)

[219] S. Levcenco et al. Temperature dependence of the exciton gap in monocrystalline $CuGaS_2$. *Physica B: Condensed Matter* **405**, 17, 3547-3550 (2010)

[220] V. M. Bermudez. Unit-cell vibrational spectra of chromium trichoride and chromium tribromide. *Solid State Communications* **19**, 8, 693-697 (1976)

[221] A. McCreary et al. Distinct magneto-Raman signatures of spin-flip phase transitions in CrI_3. *Nature Communications* **11**, 3879 (2020)

[222] W. Jin et al. Raman fingerprint of two terahertz spin wave branches in a two-dimensional honeycomb Ising ferromagnet. *Nature Communications* **9**, 5122 (2018)

[223] W. Jin et al. Tunable layered-magnetism–assisted magneto-Raman effect in a two-dimensional magnet CrI_3. *PNAS* **117**(40), 24664-24669 (2020)

[224] J. Cenker et al. Direct observation of two-dimensional magnons in atomically thin CrI_3. *Nature Physics* **17**, 20–25 (2021)

[225] B. Huang et al. Tuning inelastic light scattering via symmetry control in the two-dimensional magnet CrI_3. *Nature Nanotechnology* **15**, 212–216 (2020)

[226] X. Guo et al. Structural Monoclinicity and Its Coupling to Layered Magnetism in Few-Layer CrI_3. *ACS Nano* **15**, 6, 10444–10450 (2021)

[227] D. T. Larson & E. Kaxiras. Raman spectrum of CrI_3: An ab initio study. *Phys. Rev. B* **98**, 085406 (2018)

[228] N. Ubrig et al. Low-temperature monoclinic layer stacking in atomically thin CrI_3 crystals. *2D Mater.* **7**, 015007 (2020)

[229] K. Wang et al. Magnetic order-dependent phonon properties in 2D magnet CrI_3. *Nanoscale* **24** (2021)

[230] S. Reschke et al. Electronic and phonon excitations in α-$RuCl_3$. *Phys. Rev. B* **96**, 165120 (2017)

[231] R. Stolen & K. Dransfeld. Far-Infrared Lattice Absorption in Alkali Halide Crystals. *Phys. Rev.* **139**, A1295 (1965)

[232] M. Sparks, D. F. King & D. L. Mills. Simple theory of microwave absorption in alkali halides. *Phys. Rev. B* **26**, 6987 (1982)

[233] A. Debernardi. Phonon linewidth in III-V semiconductors from density-functional perturbation theory. *Phys. Rev. B* **57**, 12847 (1998)

[234] N. Bonini, R. Rao, A. M. Rao, N. Marzari & J. Menéndez. Lattice anharmonicity in low-dimensional carbon systems. *phys. stat. sol.* (b) **245**, 10, 2149–2154 (2008)

[235] L. L. Boyer, J. A. Harrington, M. Hass, & H. B. Rosenstock. Multiphonon absorption in ionic crystals. *Physical Review B* **11**, 4 (1975)

[236] B. Bendow & H. G. Lipson. Multiphonon infrared absorption in highly transparent MgF_2. *Physical Review B* **20**, 4 (1979)

[237] A. K. Kundu, Y. Liu, C. Petrovic & T. Valla. Valence band electronic structure of the van der Waals ferromagnetic insulators: VI_3 and CrI_3. *Scientific Reports* **10**, 15602 (2020)

[238] G. Irmer, M. Wenzel & J. Monecke. The temperature dependence of the LO(T) and TO(T) phonons in GaAs and InP. *Physica status solidi (b)* **195**, 1, 85-95 (1996)

[239] R. H. Lyddane, R. G. Sachs & E. Teller. On the Polar Vibrations of Alkali Halides. *Phys. Rev.* **59**, 673 (1941)

[240] D. Sánchez-Portal & E. Hernández. Vibrational properties of single-wall nanotubes and monolayers of hexagonal BN. *Phys. Rev. B* **66**, 235415 (2002)

[241] C. Xu, J. Feng, H. Xiang & L. Bellaiche. Interplay between Kitaev interaction and single ion anisotropy in ferromagnetic CrI_3 and $CrGeTe_3$ monolayers. *npj Computational Materials* **4**, 57 (2018)

[242] T. Feng, X. Yang & X. Ruan. Phonon anharmonic frequency shift induced by four-phonon scattering calculated from first principles. *J. Appl. Phys.* **124**, 145101 (2018)

[243] V. K. Jindal & J. Kalus. Calculation of thermal expansion and phonon frequency shift in deuterated naphthalene. *Phys. stat. sol. (b)* **133**, 1, 89-99 (1986)

[244] S. Mann & V. K. Jindal. Blue and red shifted temperature dependence of implicit phonon shifts in graphene. *Mater. Res. Express* **4**, 075038 (2017)

[245] S. D. Pandey, J. Singh, K. Samanta, N. D. Sharma & A. K. Bandyopadhyay. Temperature Dependent Variations of Phonon Interactions in Nanocrystalline Cerium Oxide. *Journal of Nanomaterials* **2015**, 492967 (2015)

[246] J. G. Bednorz & K. A. Mueller. Possible high T_c superconductivity in the Ba-La-Cu-O system. *Z. Phys. B Condens. Matter* 64, pp. 189-193 (1986).

[247] H. Hosono and K. Kuroki. Iron-based superconductors: Current status of materials and pairing mechanism. *Physica C: Superconductivity and its Applications* **514**, 399 (2015)

[248] S. Iimura and H. Hosono. Heavily Hydride-ion-doped 1111-type Iron-based Superconductors: Synthesis, Physical Properties and Electronic Structure. *J. Phys. Soc. Jpn.* **89**, 051006 (2020)

[249] Y. Cao et al. Unconventional superconductivity in magic-angle graphene superlattices. *Nature* **556**, 43 (2018)

[250] A. H. MacDonald. Bilayer Graphene's Wicked, Twisted Road. *Physics* **12**, 12 (2019)

[251] J. Chaloupka & G. Khaliullin. Orbital order and possible superconductivity in $LaNiO_3/LaMO_3$ superlattices. *Phys. Rev. Lett.* **100**, 016404 (2008)

[252] J. Zhang et al. Large orbital polarization in a metallic square-planar nickelate. *Nature Phys.* **13**, pp. 864-869 (2017)

[253] Liang Si et al. Topotactic Hydrogen in Nickelate Superconductors and Akin Infinite-Layer Oxides ABO_2. *Phys. Rev. Lett.* **124**, 166402 (2020)

[254] D. Li et al. Superconductivity in an infinite-layer nickelate. *Nature* **572**, pp. 624-627 (2019)

[255] Ai Ikeda, Y. Krockenberger, H. Irie, M. Naito and H. Yamamoto. Direct observation of infinite NiO_2 planes in $LaNiO_2$ films. *Applied Physics Express* **9**, 6 (2016)

[256] M. A. Hayward, M. A. Green, M. J. Rosseinsky, and J. Sloan. Sodium Hydride as a Powerful Reducing Agent for Topotactic Oxide Deintercalation: Synthesis and Characterization of the Nickel(I) Oxide $LaNiO_2$. *J. Am. Chem. Soc.* **121**, 38, pp. 8843–8854 (1999)

[257] K. Lee et al. Aspects of the synthesis of thin film superconducting infinite-layer nickelates editors-pick. *APL Materials* **8**, 041107 (2020)

[258] V. I. Anisimov, D. Bukhvalov & T. M. Rice. Electronic structure of possible nickelate analogs to the cuprates. *Phys. Rev. B* **59**, pp. 7901-7906 (1999)

[259] M. A. Hayward & M. J. Rosseinsky. Synthesis of the infinite layer Ni(I) phase $NdNiO_{2+x}$ by low temperature reduction of $NdNiO_3$ with sodium hydride. *Solid State Sciences* **5**, pp. 839-850 (2003)

[260] S. Zeng et al. Phase diagram and superconducting dome of infinite-layer $Nd_{1-x}Sr_xNiO_2$ thin films. *Phys. Rev. Lett.* **125**, 147003 (2020)

[261] L.-H. Hu & C. Wu. Two-band model for magnetism and superconductivity in nickelates. *Phys. Rev. Research* **1**, 032046 (2019)

[262] Z. Liu, Z. Ren, W. Zhu, Z. Wang & J. Yang. Electronic and magnetic structure of infinite-layer $NdNiO_2$: trace of antiferromagnetic metal. *npj Quantum Mater.* **5**, pp. 1-8 (2020)

[263] M. Kitatani et al. Nickelate superconductors: a renaissance of the one-band Hubbard model. *npj Quantum Mater.* **5**, pp. 1-6 (2020)

[264] F. Lechermann. Late transition metal oxides with infinite-layer structure: nickelates versus cuprates. *Phys. Rev. B* **101**, 081110 (2020)

[265] P. Werner & S. Hoshino. Nickelate superconductors: multiorbital nature and spin freezing. *Phys. Rev. B* **101**, 041104 (2020)

[266] Y. Nomura et al. Formation of a two-dimensional single-component correlated electron system and band engineering in the nickelate superconductor $NdNiO_2$. *Phys. Rev. B* **100**, 205138 (2019)

[267] M.-Y. Choi, K.-W. Lee & W. E. Pickett. Role of $4f$ states in infinite-layer $NdNiO_2$. *Phys. Rev. B* **101**, 020503 (2020)

[268] C. Hanghui et al. Dynamical Mean Field Studies of Infinite Layer Nickelates: Physics Results and Methodological Implications. *Front. Phys.* **10** (2022)

[269] T. Zhou, Y. Gao & Z. Wang. Spin excitations in nickelate superconductors. *Sci. China Phys. Mech. Astron.* **63**, 287412 (2020)

[270] I. Giaever. Energy Gap in Superconductors measured by electron tunneling. *Phys. Rev. Lett.* **5**, pp. 147-148 (1960)

[271] M. Dressel, D. Wu, N. Barišić & B. Gorshunov. Looking at the superconducting gap of iron pnictides. *Journal of Physics and Chemistry of Solids* **72**, pp. 514-518 (2011)

[272] L. Degiorgi, G. Briceno, M. S. Fuhrer, A. Zettl & P. Wachter. Optical measurements of the superconducting gap in single-crystal K_3C_{60} and Rb_3C_{60}. *Nature* **369**, 541–543 (1994)

[273] R. W. Morse. *Progress in Cryogenics* (Heywood and Cy Ltd, London, 220, Vol. I, 1959)

[274] N. E. Phillips. Heat capacity of Aluminum between 0.1°K and 4.0°K. *Phys. Rev.* **114**, pp. 676-685 (1959)

[275] W. W. Warren, R. E. Walstedt, G. F. Brennert, G. P. Espinosa & J. P. Remeika. Evidence for two pairing energies from nuclear spin-lattice relaxation in superconducting $Ba_2YCu_3O_{7-\delta}$. *Phys. Rev. Lett.* **59**, pp. 1860-1863 (1987)

[276] L. E. Chow et al. Pairing symmetry in infinite-layer nickelate superconductor. *arXiv:2201.10038* (2022)

[277] S. P. Harvey et al. Evidence for nodal superconductivity in infinite-layer nickelates *arxiv:2201.12971* (2022)

[278] Q. Gu et al. Single particle tunneling spectrum of superconducting $Nd_{1-x}Sr_xNiO_2$ thin films. *Nat. Commun.* **11**, 6027 (2020)

[279] M. Dressel & N. Drichko. Optical properties of two-dimensional organic conductors: signatures of charge ordering and correlation effects. *Chem. Rev.* **104**, pp. 5689-5716 (2004)

[280] D. N. Basov & T. Timusk. Electrodynamics of high-T_c superconductors. *Rev. Mod. Phys.* **77**, pp. 721-779 (2005)

[281] M. Dressel, N. Drichko, B. Gorshunov & A. Pimenov. THz spectroscopy of superconductors. *IEEE Journal of Selected Topics in Quantum Electronics* **14**, pp. 399-406 (2008)

[282] A. Perucchi et al. Multiband conductivity and a multigap superconducting phase in films from optical measurements at terahertz frequencies. *Phys. Rev. B* **81**, 092509 (2010)

[283] M. Tinkham. *Introduction to Superconductivity* (Mc Graw-Hill, New York, 1996)

[284] T. Timusk & D. Tanner. *Physical Properties of High Temperature Superconductors I* (World Scientific, Singapore, 1989); T. Timusk & D. Tanner. *Physical Properties of High Temperature Superconductors III* (World Scientific, Singapore, 1992)

[285] P. Roy, M. Rouzières, Z. Qi & O. Chubar. The AILES Infrared Beamline on the third generation synchrotron radiation facility SOLEIL. *Infrared Physics & Technology* **49**, 139-146 (2006)

[286] W. Peng et al. Room-temperature soft mode and ferroelectric like polarization in $SrTiO_3$ ultrathin films: Infrared and *ab initio* study. *Sci Rep* **7**, 2160 (2017)

[287] J. Petzelt et al. Dielectric, infrared, and Raman response of undoped $SrTiO_3$ ceramics: Evidence of polar grain boundaries. *Phys. Rev. B* **64**, 184111 (2001)

[288] P. Dore, G. De Marzi & A. Paolone. Refractive indices of $SrTiO_3$ in the infrared region. *International Journal of Infrared and Millimeter Waves* **18**, 125–138 (1997)

[289] C. C. Homes, R. P. S. M. Lobo, P. Fournier, A. Zimmers & R. L. Greene. Optical determination of the superconducting energy gap in electron-doped $Pr_{1.85}Ce_{0.15}CuO_4$. *Phys. Rev. B* **74**, 214515 (2006)

[290] F. Carbone et al. In-plane optical spectral weight transfer in optimally doped $Bi_2Sr_2Ca_2Cu_3O_{10}$. *Phys. Rev. B* **74**, 024502 (2006)

[291] A. V. Puchkov et al. Evolution of the pseudogap state of high- T_c superconductors with doping. *Phys. Rev. Lett.* **77**, pp. 3212–3215 (1996)

[292] J. J. Tu, C. C. Homes, G. D. Gu, D. N. Basov & M. Strongin. Optical studies of charge dynamics in optimally doped $Bi_2Sr_2CaCu_2O_{8+\delta}$. *Phys. Rev. B* **66**, 144514 (2002)

[293] A. Lucarelli et al. Phase diagram of $La_{2-x}Sr_xCuO_4$ probed in the infrared: imprints of charge stripe excitations. *Phys. Rev. Lett.* **90**, 037002 (2003)

[294] S. Lupi et al. Evolution of a polaron band through the phase diagram of $Nd_{2-x}Ce_xCuO_{4-y}$. *Phys. Rev. Lett.* **83**, 4852–4855 (1999)

[295] L. Degiorgi. Electronic correlations in iron-pnictide superconductors and beyond: lessons learned from optics. *New Journal of Physics* **13**, 023011 (2011)

[296] A. Congeduti et al. Infrared study of charge delocalization induced by pressure in the $La_{0.75}Ca_{0.25}MnO_3$ Manganite. *Phys. Rev. B* **63**, 184410 (2001)

[297] I. Lo Vecchio et al. Optical properties of V_2O_3 in its whole phase diagram. *Phys. Rev. B* **91**, 155133 (2015)

[298] Y. Yu et al. High-temperature superconductivity in monolayer $Bi_2Sr_2CaCu_2O_{8+\delta}$. *Nature* **575**, 156–163 (2019)

[299] C. C. Homes et al. A universal scaling relation in high-temperature superconductors. *Nature* **430**, 539–541 (2004)

[300] C. C. Homes, S. V. Dordevic, T. Valla & M. Strongin. Scaling of the superfluid density in high-temperature superconductors. *Phys. Rev. B* **72**, 134517 (2005)

[301] J. L. Tallon, J. R. Cooper, S. H. Naqib & J. W. Loram. Scaling relation for the superfluid density of cuprate superconductors: Origins and limits. *Phys. Rev. B* **73**, 180504 (2006)

[302] D. C. Mattis & J. Bardeen. Theory of the anomalous skin effect in normal and superconducting metals. *Phys. Rev.* **111**, pp. 412-417 (1958)

[303] N. M. Rugheimer, A. Lehoczky & C. V. Briscoe. Microwave transmission- and reflection-coefficient ratios of thin superconducting films. *Phys. Rev.* **154**, 414 (1967)

[304] L. H. Palmer & M. Tinkham. Far-infrared absorption in thin superconducting Lead films. *Phys. Rev.* **165**, 588 (1968)

[305] G. Seibold, L. Benfatto & C. Castellani. Application of the Mattis-Bardeen theory in strongly disordered superconductors. *Phys. Rev. B* **96**, 144507 (2017)

[306] F. Gross, et al. Anomalous temperature dependence of the magnetic field penetration depth in superconducting uranium-beryllium (UBe_{13}). *Z. Phys. B* **64**, pp. 175–188 (1986)

[307] R. Prozorov & R. W. Giannetta. Magnetic penetration depth in unconventional superconductors. *Supercond. Sci. Technol.* **19**, pp. R41-R67 (2006)

[308] M. Dressel & G. Grüner. *Electrodynamics of Solids: Optical Properties of Electrons in Matter* (Cambridge University Press, Cambridge, 2002)

[309] Y. Seo, W. Choi, D. Ahmad, S. Kimura & Y. S. Kwon. Temperature dependence of the superconducting energy gaps in $Ca_{9.35}La_{0.65}(Pt_3As_8)(Fe_2As_2)_5$ single crystal. *Sci. Rep.* **8**, 8648 (2018)

[310] L. Fruchter et al. Penetration depth of electron-doped infinite-layer $Sr_{0.88}La_{0.12}CuO_{2+x}$ thin films. *Phys. Rev. B* **82**, 144529 (2010)

[311] F. Bernardini, V. Olevano & A. Cano. Magnetic penetration depth and T_c in superconducting nickelates. *Phys. Rev. Research* **2**, 013219 (2020)

[312] M. V. Berry. Quantal phase factors accompanying adiabatic changes. *Proceedings of the Royal Society A: Mathematical, Physical and Engineering Sciences* **392**(1802), pp. 45-57 (1984)

[313] D. Bures. An extension of Kakutani's theorem on infinite product measures to the tensor product of semifinite w^*-algebras. *Transactions of the American Mathematical Society* **135**, pp. 199-212 (1969)

[314] R. Resta. *Geometry and Topology in Electronic Structure Theory*: Notes subjected to ongoing editing (2018)

[315] David Tong. *The Quantum Hall Effect*. arXiv:1606.06687 (2016)

[316] S. Pancharatnam. Generalized theory of interference, and its applications. *Proceedings of the Indian Academy of Sciences - Section A* **44**(5), pp. 247-262 (1956)

[317] R. Resta. Manifestations of Berry's phase in molecules and condensed matter. *Journal of Physics: Condensed Matter*, **12**(9), pp. R107-R143 (2000)

[318] D. J. Thouless. *Topological Quantum Numbers in Nonrelativistic Physics*. WORLD SCIENTIFIC (1998)

[319] O. S. Heavens. *Thin film Physics* (Methuen and Co. LTDA, London, 1970)

[320] O. S. Heavens & S. F. Singer. Optical properties of thin solid films. *Physics Today* **9**, pp. 24-26 (1956)